Anthropogenic influence on new particle formation in the marine boundary layer atmosphere

Ville Berg Malmborg

LUND UNIVERSITY
Faculty of Science

August, 2014

Master's thesis

Department of Physics, Lund University

Supervisors:

Adam Kristensson

Pontus Roldin

Erik Swietlicki

Abstract

The most important parameter for estimates of the anthropogenic induced climate change is the radiative forcing. In a comparison of the earth's radiative budget in the year 2011 relative to 1750, the intergovernmental panel on climate change concludes that the largest uncertainty in the total radiative forcing derives from aerosol particles and their ability to modify cloud properties as cloud condensation nuclei (CCN). This uncertainty may be reduced from increased knowledge of the spatial and temporal distribution of aerosol particles with CCN properties.

In this project, aerosol particles formed in coastal and marine atmospheres through so called new particle formation (NPF) were analysed spatially and temporally and an assessment of the anthropogenic impact on the marine NPF was attempted.

A method known as the NanoMap method was applied to infer the frequency of NPF in marine environments in the North Sea, Baltic Sea and the Mediterranean Sea. The results of the NanoMap analysis clearly identifies NPF frequently occurring in all three marine environments. The results suggested furthermore an increased probability of NPF in areas with heavy shipping. If the particles formed by the NPF grow to sizes with diameters larger than 50 nm, these may participate in the formation of clouds as CCN.

To assess the anthropogenic impact on marine NPF, aerosol properties and NPF were simulated with the ADCHEM model. The input gas phase emissions to the model were emissions from anthropogenic, biogenic and natural sources. The simulations were carried out mainly over the the North Sea and the model was evaluated against the total particle volume measured in Høvsøre, Denmark. The model results were reasonably consistent with the observations.

From the ADCHEM modelling results, it was concluded that anthropogenic marine emissions do influence NPF. The modelled particle size distribution at Høvsøre showed evidence of an increase in the NPF most likely as a result of anthropogenic emissions of condensable gases. However, particulate matter from shipping emissions were in some cases found to suppress the NPF. It was therefore concluded that new marine emission control legislations of sulphur-containing compounds may result in a decrease of marine NPF. If particulate emissions were also to be reduced, the result may instead be an increase of marine NPF.

The ADCHEM model results were furthermore compared to the NanoMap analysis of the same period. The comparison showed that the modelled and the inferred NPF in the marine areas coincided to a large extent. The consistency between the modelled and the inferred NPF is an encouraging result and provides a first verification of the NanoMap analysis.

Acknowledgements

This project would not have been possible without the earlier works of my supervisors. I consequently wish to acknowledge their efforts in the field of aerosol science. I also wish to express my gratitude to my main supervisor Adam Kristensson who have inspired me from start to end. Adam has throughout the duration of the project helped me and aided me perfectly in all the new events and situations that may suddenly appear as relatively new to the scientific method. Most importantly, Adam has made sure I kept the work on the same track as initially planned. I would further like to thank Pontus Roldin for his generous aid with the ADCHEM model. Without the aid of Pontus, the simulations in this project would never have been possible. Pontus is easy to work with and very knowledgeable and I am very thankful he let me work with ADCHEM and him. My gratitude also to Emelie Hermansson who have answered my questions regarding ADCHEM without any further compensation. I would also like to thank Joakim Pagels for broadening both my knowledge and interest in the field of aerosol science and for letting me discuss my thesis with him. My family, who have been very supportive throughout this project, I owe you my gratitude and my love. Finally I would like to thank my supervisor professor Erik Swietlicki; first of all I wish to thank Erik Swietlicki for making me feel welcome at the division and for his help during the time of the project and his ability to pinpoint the weaknesses and strengths of the results and the following discussion of the thesis.

The following acknowledgement is also in order:
The authors gratefully acknowledge the NOAA Air Resources Laboratory (ARL) for the provision of the HYSPLIT transport and dispersion model and/or READY website (http://www.ready.noaa.gov) used in this publication.

Abbreviations, acronyms and important symbols

ADCHEM	Aerosol dynamics and gas phase chemistry model
AIS	Air Ion Spectrometer
B	Particle mobility
BVOC	Biogenic VOC
C_C	The slip correction factor
C_D	The drag force coefficient
CCN	Cloud condensation nuclei
CO_2	Carbon monoxide
CPC	Condensation Particle Counter
DJF	December-January-February
DMA	Differential Mobility Analyzer
DMPS	Differential Mobility Particle Sizer
DMS	Dimethyl sulphide
ECAs	Emission Control Areas
EMEP	European Monitoring and Evaluation Programme
EOG	End Of Growth (time)
F_D	The drag force
G	Gibbs free energy (IUPAC: Gibbs energy)
GDAS	Global Data Assimilation System
HO_2	Hydroperoxyl radical
H_2SO_4	Sulphuric acid
HYSPLIT	Hybrid Single-Particle Lagrangian Integrated Trajectory
IMO	International and Maritime Organization
IPCC	Intergovernmental Panel on Climate Change
JJA	June-July-August
λ	Mean free path
MAM	Mars-April-May
m.a.s.l.	Meters above sea level
MCM	Master Chemical Mechanism
µm	Micrometer (10^{-6} meters)
NCEP	The National Weather Service's Nation Centers for Environmental prediction
NH_3	Ammonia
nm	Nanometre (10^{-9} meters)
NMVOC	Non-Methane VOC

N_2O	Nitrous oxide
NO	Nitric oxide
NO_2	Nitrogen dioxide
NOAA	National Oceanic and Atmospheric Administration
NO_x	$NO + NO_2$
NPF	New particle formation
OH	Hydroxyl radical
PAR	Photosynthetic Active Radiation
PBLH	Planetary Boundary Layer Height
r_b	Quasi-laminar layer resistance
RMSE	Root Mean Squared Error
SMPS	Scanning Mobility Particle Sizer
SO_2	Sulphur dioxide
SON	September-October-November
τ	The relaxation time
UTC	Coordinated Universal Time
$\mathbf{v}_{\text{drift}}$	The drift velocity
VOC	Volatile Organic Compound
WHO	World Health Organisation
WNW	West-North-West
z_0	Roughness layer height

Table of Contents

1 Introduction

The climate of the earth is a complex system determined by the amount of incoming solar radiation and the absorption, reflectance and emission of energy in the atmosphere and at the surface (IPCC, 2007). On large time scales natural processes such as e.g. changes in solar radiation are repeatedly changing the climate. However, since the beginning of the industrial era, human made or anthropogenic changes to the environment have had a significant impact on some of the parameters controlling the climate. Combustion of fossil fuels has lead to large emissions of greenhouse gases and an almost 50 percent increase of the atmospheric carbon dioxide (CO_2) concentration since 1750 (IPCC, 2013).

Adding to the concentration of greenhouse gases increases the absorption of outgoing long wave radiation in the atmosphere and raises the temperature of the earth's surface. Several feedback mechanisms may follow a change in the climate forcing. One major feedback mechanism is the change in the amount of water vapour present in the air. The saturation water vapour pressure increases with temperature, hence adding greenhouse gases allows a higher water vapour concentration in the atmosphere (IPCC, 2013). The water vapour itself has several climate feedback mechanisms. It is a strong greenhouse gas which allows more heat to be trapped in the atmosphere. Due to the changes in both water vapour concentration and temperature, the relative humidity is also modified and as a result, the amount of clouds in the atmosphere is affected. Globally, about two thirds of the sky is covered by clouds and clouds present perhaps the most variable part of the climate system. Not only may changes in the cloud cover alter precipitation patterns but also, in addition, have both a warming and cooling effect on the climate. Clouds reflect incoming solar radiation which increases the albedo of the earth and cools the surface. At the same time, clouds increase the opacity of the atmosphere in the infrared region of radiation, preventing part of the long wave radiation to be lost to space (Taylor, 2005).

CO_2 emissions are far from the only anthropogenic emission affecting the climate. Another large source of anthropogenic induced climate change arise from emissions of aerosol particles. An aerosol is liquid or particular matter suspended in a gas. An example of an aerosol is thus the air the atmosphere consists of. Aerosol particles found in the atmosphere have a variety of natural sources including primary particles directly emitted from the oceans, deserts and volcanoes but large anthropogenic sources from e.g. combustion and road wear. Aerosols may also form in situ in the atmosphere by condensation of existing precursor gases forming so called secondary aerosols (Seinfeld and Pandis, 2006).

In this project, the main concern is the climate effects of aerosol particles and the way they alter the radiative properties of the atmosphere. Apart from climatic effects, aerosols may have large negative environmental effects, e.g. when aerosols form smog or cause acidic rain far from emission sources (Wallace and Hobbs, 2006). Moreover, The World Health organization (WHO) estimates that 0.8 million yearly deaths and a total of 7.9 million lost years of healthy life are caused by urban air pollution, where aerosol particles are the dominant contributor to the increased mortality rates (World Health Organisation, 2002).

Radiative forcing (Wm^{-2}) is a measure of the influence a factor has in changing the radiative balance of the earth-atmosphere system. A positive radiative forcing is generally associated with a heating of the surface while a negative radiative forcing cools the surface. Aerosol particles influence the radiative forcing directly by scattering and absorbing incoming solar radiation and outgoing longwave radiation. This effect is termed the direct effect (IPCC, 2007).

Aerosol particles act as cloud condensation nuclei (CCN) by forming surfaces on which water vapour may condense up on. These CCN are hence essential for the formation of clouds in the

earth's atmosphere and therefore, changes in the concentration of the CCN indirectly influence the climate by altering the albedo, amount and lifetime of clouds (IPCC, 2007). Often termed the first indirect effect, aerosol particles may alter the cloud albedo when an increase of CCN subsequently results in an increase of the number of water droplets in a cloud, thereby increasing the scattering and albedo of the cloud. Second indirect effects are changes in the liquid water content, cloud height and an increased life time of clouds due to an increased droplet concentration and less precipitation (Houghton et al., 2001. i.e. IPCC 2001). Anthropogenic emissions may alter the amount of CCN present in the atmosphere and may contribute to the climate change by altering the indirect effects as well as the direct effect.

Figure 1 shows the best estimates of the radiative forcings in 2011 relative to 1750. Both direct aerosol radiative forcings and cloud adjustments from aerosols are estimated to have a negative radiative forcing. The cloud adjustment is associated with a very large uncertainty in the magnitude of the radiative forcing. An important source for the large uncertainty is the incomplete aerosol distribution data used as input in global climate models (IPCC, 2007). Focusing on the indirect climate effects of aerosols, quantifying the distribution and production of CCN is therefore necessary in order to estimate the radiative properties of clouds. To improve climate predictions, the relative importance of different aerosol sources contributing to the CCN concentration needs to be studied (Merikanto et al., 2009).

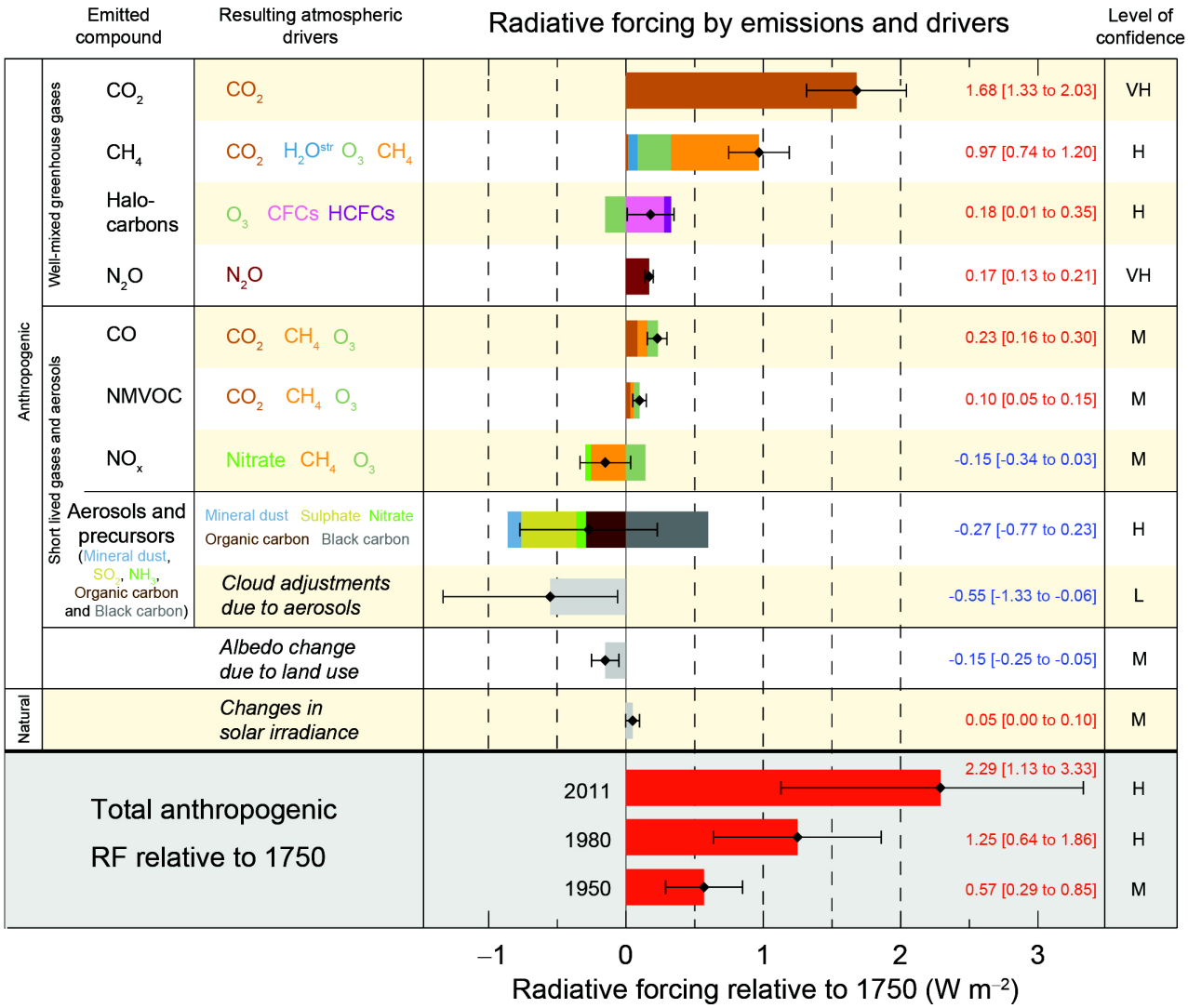

Figure 1: Radiative forcing estimates in 2011 relative to 1750 and aggregated uncertainties for the main drivers of climate change. The level of confidence in the right column signifies a low (L), medium (M), high (H) or very high (H) confidence in the results. Source: IPCC, 2013: Summary for Policymakers.

Secondary aerosols are formed in the atmosphere through nucleation of gaseous species, which is termed new particle formation (NPF), and through the condensation of vapours on existing particles forming e.g. secondary organic aerosols (SOA). The NPF contributes significantly to the total mass and number of aerosols present in the atmosphere (Spracklen et al., 2006; Zhang et al., 2012). NPF is often observed as typical events where a large increase of nanometre sized particles followed by growth of these particles to larger sizes can be observed (figure 2). Particle formation in the atmosphere exhibits two very clear stages. The particle formation is initiated by gas to particle formation and the nucleation of small stable clusters with sizes between 1-2 nm. The nucleation of the clusters is then followed by growth by the condensation of existing vapours. In the first stage of the NPF, sulphuric acid, water and ammonia (or amines) are believed to be the driving precursor gases. In the second stage, the growth of the newly formed particles, low volatile organic vapours are considered the main growth factor (Zhang et al., 2012; Kulmala et al., 2013).

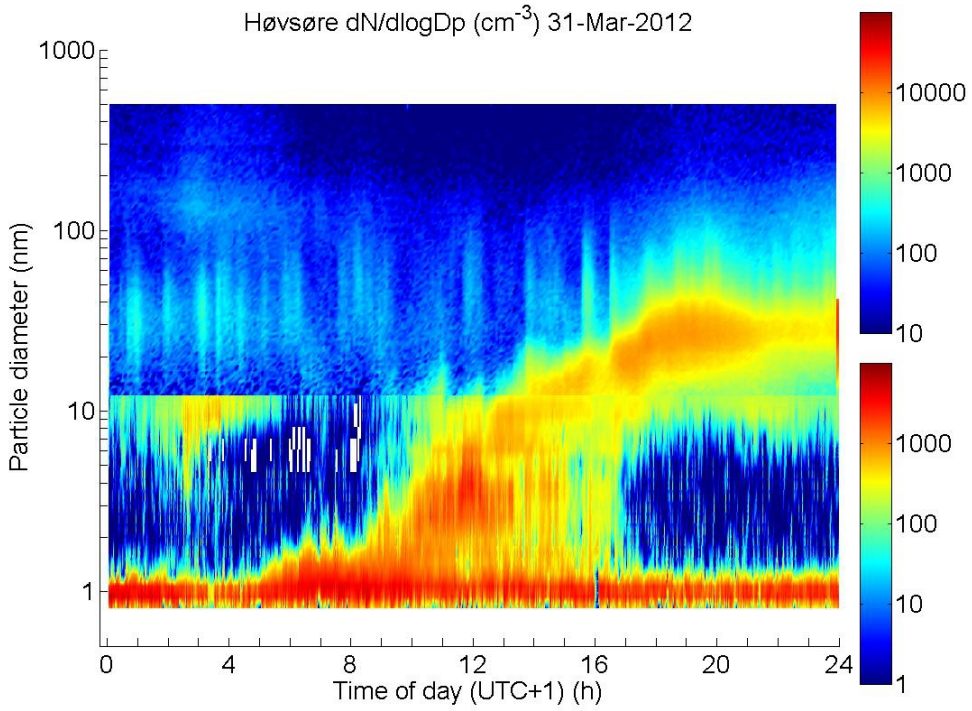

Figure 2: New particle formation and growth of new particles to larger sizes observed in Høvsøre, Denmark.

Modelling studies have shown that the NPF in the atmosphere may contribute to almost as much as 50% of the CCN present in low level clouds (Merikanto et al., 2009; Spracklen et al., 2008). There is furthermore strong evidence that the number of cloud droplets present in a cloud may increase significantly from NPF (Kerminen et al., 2005). Such findings show that secondary aerosol particles have a profound impact on the albedo and radiative properties of the earth's atmosphere. Furthermore, anthropogenic emissions of aerosol precursor gases, which leads to an increase in the amount of secondary aerosols, are likely to effect the anthropogenically induced climate change. Due to the increased albedo and resulting negative radiative forcing, these emissions may potentially result in an offset of some of the warming from greenhouse gas emissions as shown in figure 1.

NPF is frequently observed in different environments, from the polar regions, boreal forests, rural continental, urban and coastal areas (Kulmala et al., 2004). Marine NPF has been observed (e.g. Covert et al., 1992, Wiedensohler et al., 1996, Chang et al., 2011), however, modelling studies have shown that marine nucleation is much less likely to occur than in many terrestrial environments

(Pirjola et al., 2000). Nevertheless, O'Dowd et al. (1998) observed frequent NPF in the coastal marine environment. These measurements revealed NPF on small scales of 100's of meters which was later shown (O'Dowd et al., 2002) to be the cause of nucleation involving biogenic iodine oxides. Recent studies have shown that NPF is occurring in the marine boundary layer over the open ocean during periods of high biological activity (O'Dowd et al., 2010). Other studies show that biogenic marine isoprene emissions may strongly enhance the formation of secondary organic aerosols (Hu et al., 2013) and in the Southern Ocean, a correlation between algal blooms, the number of cloud droplets and a decrease in the droplet radius was found and attributed to marine isoprene emissions (Meskhidze et al., 2006).

Although marine NPF has been observed, the frequency of marine NPF and the anthropogenic impact on marine NPF remains unclear. In this project, measurement data from three coastal sites have been analysed together with meteorological backward trajectories using a method known as the NanoMap method. From the NanoMap analysis, it is possible to infer the frequency and probability of NPF also at large distances from the measurement sites. The analysis was used to infer NPF over sea areas in the North Sea, the Baltic Sea and the Mediterranean Sea. The results of the analysis may be further used to find correlations between NPF events and the spatial and temporal extent of NPF, meteorological conditions and biogenic and anthropogenic emission sources. The results of the NanoMap analysis have an unknown uncertainty and are not easily verified due to the limited number of measurement sites. During the project, a Lagrangian aerosol dynamics and gas phase chemistry model (ADCHEM) was used to model aerosol properties along meteorological airmass trajectories. In an effort to verify the NanoMap results, the modelled NPF could be compared to the inferred NPF of the NanoMap results. However, the main reason for applying the model was the ability to specifically simulate the influence that biological and anthropogenic emission sources have on NPF in these specific marine environments.

2 Hypothesis and aims

We hypothesise that new particle formation frequently occurs over coastal oceans and marine areas with large anthropogenic emissions.

From the hypothesis, the specific aims of this project have been formulated:

Task 1. To quantify the frequency of occurrence of new particle formation in coastal polluted marine areas.

Task 2. To estimate the influence of anthropogenic emissions of sulphur-containing compounds and volatile organic compounds on the NPF in the coastal polluted marine areas.

3 Atmospheric aerosol particles

This chapter briefly describes aerosol particle distributions, their sources and their chemical composition.

3.1 Aerosol size distributions

Aerosol particles are often characterised by their diameters and related to the number, surface, volume or mass distribution. Measurements of this kind are termed aerosol size measurements. Other measurements which do not give any information on the aerosol distribution may for example measure the total mass or volume. Since particles have distinct diameters or masses, aerosol size distributions are discrete. Aerosol measurements can generally not resolve all particle diameters but are limited to a discrete number of size bins in which all particles with diameters inside the size range of the bin are measured. Typically the number of size bins ranges from 10-100 with most of the bins at lower diameters which means that the size bins are often not equally spaced.

Presenting aerosol data may be done in several ways and the preferred way resembles a normal distribution. Assuming a measured aerosol number concentrations for a small number of size bins with known interval and mean diameter of the interval; figure 3 presents three different alternatives to present the data. The first alternative (figure 3a) displays the data as the number of particles in each size bin (ΔN). Since the intervals are not equally spaced, the number of particles may be interpreted as very large at large diameters compared to at small diameters, which is not the fact. A more illustrative way to present the data is to weight the concentration of particles by the size interval (ΔD), as shown in figure 3b. Similarly the number concentration may be weighted by the logarithm of the size interval ($\Delta \ln(D)$) as shown in figure 3c. The last alternative resembles a normal distribution, the aerosol distribution is said to be lognormally distributed and figure 3c is the common way to present aerosol size distributions.

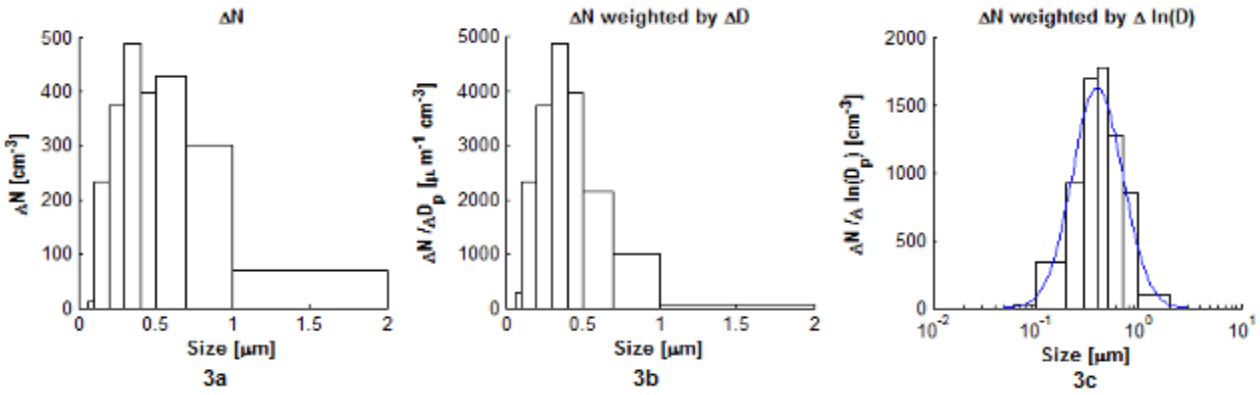

Figure 3: Illustration of different ways to present aerosol data. 3a: Total number concentration in each size interval. 3b: The number concentration weighted by the width of each size interval. 3c: The number concentration weighted by the difference in the logarithm of the size interval limits and fitted lognormal distribution. The x-axis is logarithmic in 3c.

To approximate the aerosol distribution with a lognormal distribution it is necessary to calculate the geometric mean diameter (or count median diameter) $\bar{D}_{\mathrm{pg}}$ and the geometric standard deviation σ_g. These are calculated in equation 3.1 and 3.2 and the fitting of the lognormal distribution in figure 3c is calculated using equation 3.3.

$$\bar{D}_{pg} = \exp\left[\frac{1}{N_t}\sum_{i=1}^{M}\left(N_i \ln\left(D_{pi}\right)\right)\right] \qquad \text{EQ 3.1}$$

$$\sigma_g = \exp\left[\frac{1}{N_t}\sum_{i=1}^{M} N_i\left(\ln(D_{pi}) - \ln(\bar{D}_{pg})\right)^2\right]^{1/2} \quad \text{EQ 3.2}$$

$$\frac{\Delta N}{\Delta \ln(D_p)} = \frac{N_t}{\sqrt{(2\pi)}\ln(\sigma_g)} \exp\left(-\frac{\left(\ln(D_p) - \ln(\bar{D}_{pg})\right)^2}{2\ln^2(\sigma_g)}\right) \quad \text{EQ 3.3}$$

Aerosol measurements are discrete measurements, however for large particle concentrations, it is acceptable to approximate the size distribution with a continuous distribution. Approximating aerosol measurements with a number of lognormal distributions significantly reduces the amount of data needed to describe a measurement.

An aerosol distribution can often be approximated by several lognormal distributions, so called modes. The modes consists of particles from different background sources and have very different atmospheric lifetimes. The number distribution is usually dominated by two modes at particle diameters less than 0.1 μm. The smallest particles below 10-20 nm represent the nucleation mode and a second mode is generally found in the size range 10-100 nm called the Aitken mode. The mass and volume distributions are normally dominated by two modes. An accumulation mode in the size range 0.1-2 μm and a coarse mode consisting of particles with diameters larger than 2 μm. The accumulation mode is frequently made up of two submodes, the condensation submode and the droplet submode. In general, particles with diameters larger than 2.5 μm are called coarse particles and with diameters less than 2.5 μm are called fine particles (Seinfeld and Pandis, 2006).

3.2 Aerosol sources

Aerosol particles have a large number of diverse sources and it is important to distinguish between the primary aerosols, which are emitted directly into the atmosphere, and the secondary aerosols, which are formed in the atmosphere from gas to particle conversion.

Primary aerosols may be mechanically generated, derive from combustion or from biological activity. Primary marine aerosols are mechanically generated by white capping of waves and by film or jet drops from gas bubbles bursting at the surface. Deserts and semiarid regions are the largest sources of particles on the surface of the earth where soil and dust is transported to the atmosphere by turbulent wind acting on the surface. Anthropogenic particle emissions are dominated by combustion of fossil fuels and biomass burning. Biogenic particles from plants and animals can be seeds, spores, pollen or bacteria, algae, fungi and viruses (Wallace and Hobbs, 2006; O'Dowd et al., 2007).

Secondary aerosols are particles which are formed in the atmosphere by condensation from the gas phase. A vapour may condense on existing particles, so called heterogeneous nucleation, or condense to form new particles, in a process called homogeneous nucleation. Heterogeneous nucleation is favourable if the existing particle distribution already has a large surface area. Nucleation of new particles generates the smallest particles observed but is often followed by a subsequent growth. This nucleation and growth is termed new particle formation and has been observed in many areas of the world. NPF is described in more detail in chapter 5.5.

3.3 Emissions, chemical composition and typical concentrations

Aerosols have varying sources and hence, the chemical composition may change between different environments. Table 1 summarizes the main aerosol types, sources and estimated fluxes to the atmosphere. The main contributor to the mass of marine aerosols is sodium chloride. Over the continents, windblown mineral dust from deserts and semiarid regions makes a large contribution to the total aerosol concentration. Other environments than marine have the aerosol mass dominated

by contributions of sulfates, ammonium, nitrates and organic carbon. Carbonaceous aerosols can be both organic matter and elemental carbon. The elemental carbon, also known as black carbon or soot, is emitted directly into the atmosphere while organic carbon can be emitted directly or form by condensation of organic vapours in the atmosphere (Seinfeld and Pandis, 2006)

Table 1: Aerosol emission sources. Adopted from IPCC, 2001.

Aerosol type	Emission sources	Global emissions (Tg year^{-1})
	Primary	
Organic carbon	Biomass burning	54
	Fossil fuel	28
	Biogenic	56
Black carbon	Biomass burning	6
	Fossil fuel	7
Industrial	Dust, etc.	100
Sea salt	Oceans	3300
Mineral	Soils	2150
	Secondary	
Sulfate	Anthropogenic	122
	Biogenic	57
	Volcanic	21
Nitrate	Anthropogenic	14
	Natural	4
VOC	Biogenic VOC	16

As a result of the different emission sources, particle concentrations differ considerably between geographical areas. Therefore, areas are often grouped into urban, rural continental, marine and polar areas. Aerosol concentrations are generally low in marine areas and high in urban areas. Typical concentrations can be addressed to the different environments and table 2 shows particle concentrations in geographical areas summarised from several studies.

In polar regions, the aerosol concentration is low and generally characterized by three modes at small particle diameters. The modes found are a nucleation mode at diameters less than 20 nm, an Aitken mode at approximately 50 nm and an accumulation mode close to 200 nm (Covert et al., 1996). In the Arctic, three periods of the year can be characterized. During spring is a period known as the haze period, characterised by a large accumulation mode. In the summer, high concentrations of locally formed nucleation mode particles and low concentrations of the accumulation mode are observed. The rest of the year is characterised by a low accumulation mode concentration and practically no particles in the fine and the nucleation mode (Tunved et al., 2013).

Mass concentrations of marine aerosols have been measured up to 1000 μg m^{-3} during strong wind conditions but number concentrations rarely exceed 600 cm^{-3}. The size distribution of marine particles can be described by three modes, an Aitken mode at 30 nm, an accumulation mode at 0.1 μm and a mode of particles larger than 0.5 μm (O'Dowd et al., 2007; Fitzgerald, 1991).

Rural continental aerosols have three typical modes. Two modes are generally observed below diameters of 0.1 μm and a coarse mode dominating the mass distribution. The particles originate

from natural sources and to a smaller extent from anthropogenic aerosols.

Urban aerosol sources include primary emissions from industries, traffic, natural background sources and secondary formation from precursor gases. Fine mode particles in urban air are primary particles from combustion sources and secondary aerosols. Coarse mode particles are typically mechanically generated from tire wear, soil dust, etc. Often, the urban number distribution is dominated by small particles up to 0.1 μm and the urban surface distribution dominated by particles with diameters between 0.1-0.5 μm (Seinfeld and Pandis, 2006).

Table 2: Typical number and mass concentrations for different geographical areas.

Geographical area	Average mean concentration [cm^{-3}]	PM10 [$\mu g\ m^{-3}$]	References
Urban	5000-20000 (Europe)	20-50 (Europe)	Aalto et al., 2005; Putaud et al., 2004
Near city	3000-10000 (Germany)	20-40 (Europe)	Wiedensohler, 2002; Putaud et al., 2004
Rural	1000-4000 (Germany)	1-20 (Europe)	
Remote marine	100-1000 (remote Atlantic, Pacific trade wind region)	1-50 (Pacific trade wind region)	Fitzgerald, 1991
Polar marine	5-250 (Arctic region)	0.1-1 (Arctic region)	Covert et al., 1996; Tunved et al. 2013

4 Aerosol measurement techniques

This chapter focuses on the measurement techniques used in this project. In order to better explain these methods, the motion of particles in a fluid is discussed in chapter 4.1. A description of the measurement techniques is found in chapter 4.2.

The measurement instruments used to quantify the aerosol size distributions in this project were three different Scanning Mobility Particle Sizers (SMPS) and two different Air Ion Spectrometers (AIS). The concept of the instruments are the same for all three measurement stations and the theoretical description of how the instruments work is therefore generalized.

Both the AIS and the SMPS instruments measure the electrical mobility diameter of a particle. An AIS measures only particles naturally carrying electrical charge (ions). An SMPS includes a charger, allowing also the detection of those particles not carrying electrical charge before entering the instrument.

For a detailed discussion of chapter 4.1 the reader is referred to Seinfeld and Pandis (2006), from which most of the equations and theory in this chapter derive from.

The measurement techniques used are thoroughly described in "Aerosol measurement: principles, techniques, and applications" by Kulkarni et al. (2011) which therefore has provided an excellent source of information for the following sections. If not explicitly stated otherwise, the reference for chapter 4.2 is Kulkarni et al. (2011) .

4.1 Particle motion in a fluid

On the smallest scale, molecules in a fluid move in straight lines until they collide with another molecule. The average distance travelled by a gas molecule between collisions is called its mean free path (λ). A large particle suspended in the gas will see gas molecules behaving as a continuous fluid. A small particle, with a diameter smaller than the mean free path of the gas, will on the other hand observe particles moving around it in all directions. The dimensionless relation between the radius of a particle (R_p) and the mean free path of the gas is called the Knudsen number (Kn, eq. 4.1).

$$\mathrm{Kn} = \frac{\lambda}{R_p} \qquad \text{EQ 4.1}$$

The mean free path can be calculated from the viscosity of the gas (μ), the pressure (p), the molecular weight of the gas molecules (M), the temperature (T) and the gas constant (R). For gas molecules in air, λ_{air} is usually calculated as only consisting of a single species and its mean free path is close to 65 nm in room temperature (eq. 4.2).

$$\lambda_{air} = \frac{2\mu}{p\left(8M/\pi RT\right)^{(1/2)}} \approx 65\ \mathrm{nm} \qquad \text{EQ 4.2}$$

Particles with diameters smaller than 0.1 μm behave more or less as free molecules and particles with Kn>>1 are said to be in the kinetic regime. For particles with diameters larger than 0.2 μm, Kn<<1 and the particles are said to be in the continuum regime. Particles with Kn~1 are said to be in the transition regime.

As a particle moves through a viscous fluid, a drag force (F_D) working in the opposite direction of the motion is exerted by the fluid. Stoke's law (eq. 4.3) solves the Navier-Stokes equations describing the particle motion in a viscous fluid for small Reynolds numbers, (Re, eq. 4.4) i.e. when the viscous forces dominate over the inertial forces on the moving particle. In equation 4.3 and 4.4,

ρ is the density of the fluid, v is the velocity of the particle with respect to the fluid and D_p the diameter of the particle.

$$F_D = 3\pi\mu D_p \nu \qquad \text{EQ 4.3}$$

$$\mathrm{Re} = \frac{\rho \nu D_p}{\mu} \qquad \text{EQ 4.4}$$

In the calculation of the drag force (F_D), Stoke's law assumes that the particle is a rigid sphere, a no slip condition at the particle surface and that the Reynolds number is very small. For aerosol particles, Re is sometimes not small enough for inertial forces to be neglected since molecules may slip on the surface of the particle and particles are not always perfectly spherical (Leith, 1987).

To correct for the approximation in Stoke's law that the Reynolds number is small, an empirically measured coefficient called the drag coefficient (C_D) can be introduced. The drag force on the particle can then be calculated as in equation 4.5; however it can be shown that the correction only becomes important for aerosol particles with diameters larger than 20 μm.

$$F_D = \frac{1}{8}\pi C_D \rho D_p^2 \nu^2 \qquad \text{EQ 4.5}$$

The no slip condition is a good approximation for particles in the continuum regime and hence in the limit as the Knudsen number approaches zero. For particles with diameters larger than 10 μm, the correction is only close to 2 percent. For small particles with Kn~1, the slip on the surface becomes appreciable and the drag force is reduced by almost a factor of 3 (Seinfeld and Pandis, 2006). The slip correction factor (C_c) can be calculated from the mean free path and the particle diameter (eq. 4.6) and included in the calculation of the drag force (eq. 4.7). The constants (α, β and γ) in equation 4.6 are experimentally determined e.g. from the famous Millikan's oil drop experiment (Allen et al. 1982).

$$C_c = 1 + \mathrm{Kn}\left[\alpha + \beta e^{\left(-\frac{\gamma}{Kn}\right)}\right] \qquad \text{EQ 4.6}$$

$$F_D = \frac{3\pi\mu D_p \nu}{C_c} \qquad \text{EQ 4.7}$$

If a particle is falling through a fluid due to a gravitational field, the forces acting on the particle are the gravitational force and the drag force of which the latter is a direct consequence of the particle moving through the fluid. After a specific time, the relaxation time (τ) of the particle, the particle must reach a steady state in which the particle is no longer accelerating. The relaxation time is generally very short for aerosol particles (Seinfeld and Pandis, 2006). The velocity reached after falling τ seconds is termed the terminal settling velocity (v_t) and for a particle with mass m_p the terminal settling velocity is given by equation 4.8. Equation 4.8 applies to particles with diameters less than 20 μm where C_D can be neglected.

$$\nu_t = \frac{m_p C_c g}{3\pi\mu D_p} = g\tau \quad \text{where, } \tau = \frac{m_p C_c}{3\pi\mu D_p} \qquad \text{EQ 4.8}$$

For any force acting on the particle it may be assumed that the accelerating force and the drag force becomes equal at a specific velocity. The drift velocity ($\boldsymbol{\nu}_{\mathrm{drift}}$) of a particle may thus be generalized to equation 4.9 where $\mathbf{F}_{ext}$ is an external force and B is the particle mobility defined by equation 4.10.

$$\boldsymbol{\nu}_{drift} = B\,\mathbf{F}_{\mathrm{ext}} \qquad \text{EQ 4.9}$$

$$B = \frac{\tau}{m_p} = \frac{C_c}{3\pi\mu D_p} \qquad \text{EQ 4.10}$$

The particle mobility may also be used to calculate the Brownian diffusivity (D) of the particles, a relation known as the Einstein relation (eq. 4.11).

$$D = BkT \qquad \text{EQ 4.11}$$

Finally, if a particle carries an electrical charge, q, and an electric field of strength $\mathbf{E}$ is acting on the particle, the particle will be put in motion and the electrical migration velocity $\mathbf{v}_e$ is obtained (eq. 4.12). B_e is the electrical mobility, defined in equation 4.13.

$$\boldsymbol{v}_e = \frac{qC_c}{3\pi\mu D_p}\mathbf{E} = B_e\mathbf{E} \qquad \text{EQ 4.12}$$

$$\text{Where, } B_e = \frac{qC_c}{3\pi\mu D_p} \qquad \text{EQ 4.13}$$

An instrument measuring the electrical mobility of particles, e.g. the differential mobility analyzer used in the Scanning Mobility Particle Sizer, classifies particle sizes according to their electrical mobility. The measured diameters are thus related to the electrical mobility and known as the electrical mobility equivalent diameter, defined as the diameter of a particle with unit density having the same electrical mobility as the measured particle.

4.2 The Scanning Mobility Particle Sizer

The SMPS normally consists of a drier, a bipolar charger, a differential mobility analyzer (DMA) and a particle counter such as the condensation particle counter (CPC). Figure 4 shows the set-up of the SMPS system used at the measurement station in Høvsøre.

In the Høvsøre set up, sampled air was first led through a drier to the bipolar charger. In the bipolar charger the aerosols attain a known charge distribution and with this charge distribution the particles enter the DMA. The DMA had a sheath flow of 5.0 L min^{-1} and an aerosol flow entering the DMA of 1.0 L min^{-1}. The negative voltage of the DMA was continuously decreased for 4 minutes, and during this time, particles were classified according to their electrical mobility (Kivekäs et al., 2014). The classified particles exit the DMA and enters the CPC which detects and counts the classified particles.

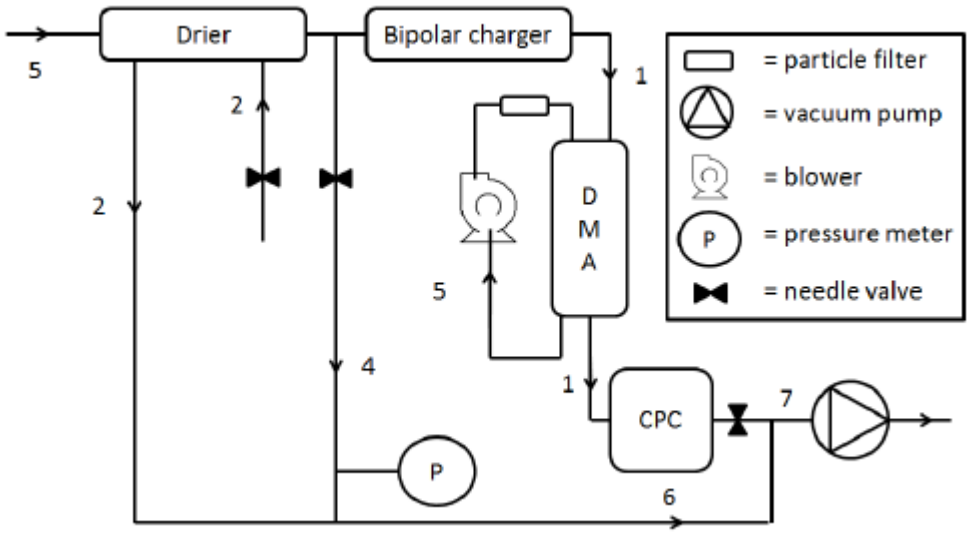

Figure 4: The SMPS system set-up in Høvsøre, Denmark. Source: Kivekäs et al., 2014. Courtesy of Niku Kivekäs.

4.2.1 Bipolar charger

In a mixture of positive and negative ions, the magnitude of the charge of a particle may increase or decrease by attachment of ions with identical or opposite charges. In such a mixture, particles are said to undergo bipolar diffusion charging. If the initial state of the ion mixture has a net charge equal to zero, the aerosol particles will eventually also reach a quasi-steady state in which the rate of attachment of positive ions equals the rate of attachment of negative ions.

The bipolar charger used in Høvsøre consists of a radioactive source (^{85}Kr) which β-decays into ^{85}Rb. The emitted electrons ionize the surrounding atmosphere, providing the mixture of positive and negative ions needed in order for a bipolar diffusion charging of the particles. The final charge distribution of the aerosol particles in the quasi-steady state closely resembles the Boltzmann distribution. However, due to differences in the molecular weights of the ions, these ions have different mobilities. This may cause the rate of which ions attach to the particles to vary. As a result, the charge distribution deviates from the Boltzmann distribution and a correction is necessary. The correction, named after its developer, is known as the Fuchs model.

4.2.2 Differential Mobility Analyzer

The DMA consists of an aerosol inlet, an inner and outer electrode, a sheath flow stripped of particles using a particle filter and an aerosol sample exit where classified particles may exit and continue towards the CPC (figure 5). The inner electrode, a circular rod mounted in the centre of the DMA is continuously ramped between low and high voltages (approximately 10 kV). Particles, of the opposite charge of the electrode, that enter the DMA sheath flow are advected towards the inner electrode.

If the electrical mobility is too high, the particle will deposit on the electrode, and if the mobility is

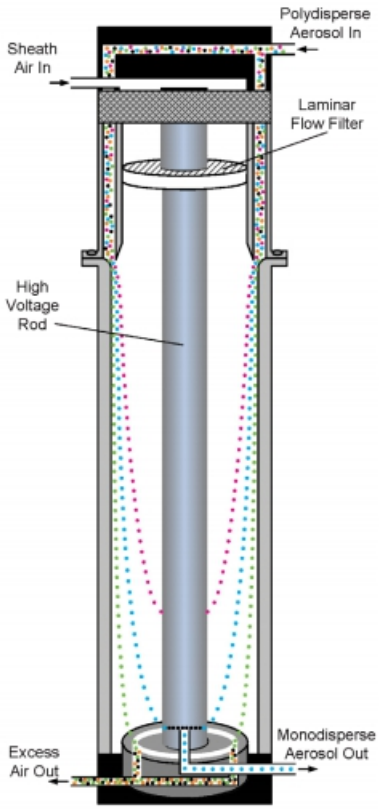

Figure 5: Overview of the DMA composition. The coloured trajectories illustrates particle trajectories in the DMA. With permission: TSI Inc., St. Paul, USA.

too low, it will exit with the sheath flow. However, particles with a narrowly defined mobility will exit the DMA in the aerosol sample exit. These particles are later counted by the CPC and a size distribution may be obtained from the knowledge of the mobility and the number of particles detected by the CPC.

As aerosols move with the sheath flow and are advected towards the inner electrode, radial diffusion of particles will allow particles with slightly lower or higher mobilities to exit with the aerosol exit flow. Therefore, in order for the DMA to correct for those particles sampled outside the specific mobility measured, the probability that particles with a specific mobility exits the DMA through the sampling exit needs to be calculated. This is calculated with a classifier transfer function which includes the effects of particle diffusion.

The DMA may ramp the electrode voltage continuously or discretely. When ramped discretely, the DMA ensures that the measured particles all have the same mobilities. Since the charge distribution of the particles are (close to) Boltzmann distributed, the number of particles counted by the CPC may directly be converted into a size distribution. Such a measurement technique is called a differential mobility particle sizer (DMPS). The disadvantage of the DMPS is mainly much longer scanning times. In the case of the SMPS, the electrode voltage of the DMA is ramped continuously. The voltage of the electrode is the factor determining the size bin the particle is classified in. During a continuous ramping, the time delay between the DMA and the detection of the particles in the CPC must be accounted for. Particles with different mobilities are also mixed during the passage to the CPC, which smears the resulting classification.

In the final analysis of deducing the size distribution, the collected data must be corrected for (1) the charge distribution, (2) the time delay between the DMA and CPC, (3) smearing effects and (4) diffusion of particles during the time of flight inside the DMA. These corrections are typically accounted for using fast data inversion algorithms in the software accompanying modern SMPS systems, requiring only user input of estimated residence times in the tubing, the DMA and CPC and the CPC counting efficiency.

4.2.3 Condensation Particle Counter

CPCs employs various optical techniques for the detection of aerosol particles. Accurate detection of nanometre sized particles using optical methods is difficult to achieve. To increase the surface area of the particles and hence the detection area, particles are grown to larger sizes by in situ condensation of a supersaturated vapour. In a continuous flow CPC such as the one employed in the SMPS system in Høvsøre (figure 6), the aerosol particles pass over an alcohol reservoir into a condenser. In the condenser, particles grow by condensation of the alcohol to detectable sizes larger than 12 μm. However, due to local differences of the vapour concentration, some particles are not grown, which lowers the counting efficiency of the CPC for particles with diameters less than 10 nm. The detection system is based on the scattered light from a single particle passing a beam of light. A laser and photo-detector are generally used to detect the particles. The counting efficiency is a function of particle size and is obtained by calibration of the CPC using monodisperse aerosol particles with known size.

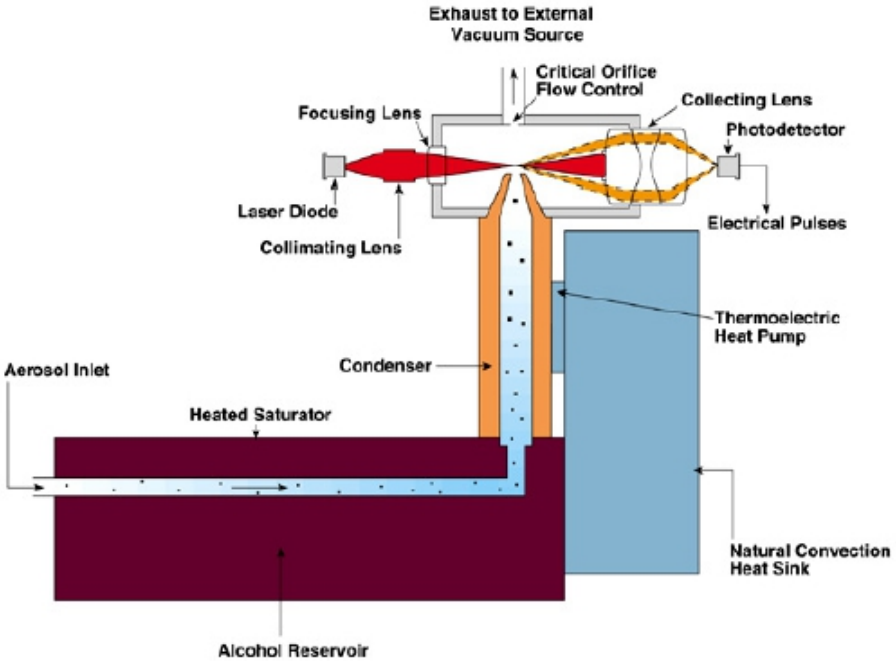

Figure 6: Schematic picture of the CPC (TSI, model 3010) used in Høvsøre. With permission: TSI Inc., St. Paul, USA.

4.3 The Air Ion Spectrometer

The AIS resembles the SMPS in many ways. However, the main difference is in the detection system. The AIS does not include a CPC to detect the particles; instead the outer electrode of the DMA contains a number of electrometers along the length of the electrode. Opposite to the SMPS, particles are advected away from the inner electrode and are deposited on the electrodes according to their electrical mobilities. The electrodes detects and counts the particles. The electrometers form the number of channels (size bins) in the size distribution of the instrument. AIS instruments are able to detect particles or clusters with sizes less than 1 nm in mobility diameter in the lowest channel and up to approximately 40 nm in the highest channel (Asmi et al., 2009).

5 Aerosol dynamics

Different aerosol dynamic processes are discussed in this chapter. The loss of aerosol particles from the atmosphere takes place via dry or wet deposition (chapter 5.1). The transformation of particles is determined by the coagulation of particles (chapter 5.2) and the condensation and evaporation of gas phase compounds on the existing particles (chapter 5.3). Some of these gases are discussed in chapter 5.4. The formation of new particles in the atmosphere through the process of NPF is finally addressed in chapter 5.5.

5.1 Particle deposition

The deposition of atmospheric particles may arise from gravitational settling of particles or Brownian transport to the surface. Such deposition is generally termed dry deposition. Particles may also be suspended in cloud droplets. When these cloud droplets fall out as rain drops, particles are efficiently transported to the surface in a process termed wet deposition.

Dry deposition accounts for approximately 10-20 % of the total removal of particles from the atmosphere. For particles to be dry deposited, they must first be transported to the surface. Near the surface, particles collide and stick to the leaves, grass, rocks etc. by impaction, due to their inertia, or by interception from the obstacles. For small particles with diameters less than 0.1 μm, Brownian motion is mainly responsible for this transport. For large particles with diameters above 1 μm, gravitational settling is causing the transport of the particles to the surface. In between these particle sizes, neither Brownian motion nor gravitational settling is very effective. Therefore, these particles are accumulated in the atmosphere until they are finally deposited through wet deposition. It is for this reason that the particles within this size range have been termed accumulation mode particles.

As a result of the particle deposition, the average lifetime of atmospheric particles is less than one day for particles with diameters less than 10 nm and for particles larger than 20 μm. However, for accumulation mode particles, the atmospheric lifetime may be several weeks (Wallace and Hobbs, 2006).

5.2 Coagulation

Coagulation in aerosol populations arises from two particles that collide and adhere. The collision of particles may arise from the motion caused by any force acting on the particles. For small particles in the atmosphere, the most important process determining the rate of collisions is the Brownian motion resulting in a random motion of the particles. Coagulation due to Brownian motion is often termed Brownian coagulation. Besides the rate of collisions, the collision efficiency is needed in order to calculate the coagulation rate (J_{12}) (Seinfeld and pandis, 2006). The collision efficiency (α) is the probability that two colliding particles will coagulate and form a new larger particle; this term however is often approximated as equal to one without any large errors (Roldin et al, 2011).

The coagulation rate is calculated by equation 5.1 where, K_{12} is the Brownian coagulation coefficient between two particles and N_1 and N_2 are the number concentrations of the two particles in a given volume of air. To evaluate equation 5.1, Fuchs form of the Brownian coagulation coefficient (eq. 5.2) may be applied. The coagulation coefficient includes the collision rate and describes the Brownian motion of particles in the kinetic regime as well as in the continuum regime of the particles.

$$J_{12} = K_{12} N_1 N_2 \qquad \text{EQ 5.1}$$

$$K_{12}=2\pi(D_1+D_2)(D_{p1}+D_{p2})[\frac{D_{p1}+D_{p2}}{D_{p1}+D_{p2}+2(g_1^2+g_2^2)^{1/2}}+\frac{8\alpha(D_1+D_2)}{(\bar{c}_1^{\,2}+\bar{c}_2^{\,2})^{1/2}(D_{p1}+D_{p2})}]^{-1} \quad \text{EQ 5.2}$$

In equation 5.2, D_1 and D_2 denotes the diffusion coefficients of the two particles, D_{p1} and D_{p2} their diameters, $\bar{c}_1$ and $\bar{c}_2$ are the mean velocities of the particles and g_1 and g_2 are functions of the particle diameters and their mean free path in the air (Seinfeld and Pandis, 2006).

Coagulation may change particles from spherical objects to aggregates of chain like structure (Seinfeld and Pandis, 2006). For the non-spherical particles, size classification using mobility classifiers is complicated as the drag on a non-spherical object may increase drastically. Coagulation also changes the size distribution of the aerosol and in turn the chemical composition of the particles may be altered.

5.3 Condensation

Condensation of vapours is the process of mass transfer from the gas phase to the particulate phase. When the opposite occurs this is termed evaporation. These are chemical equilibration processes where the energy (E) of the system is minimized at the same time as the disorder of the system (entropy, S) is maximized. The theory of condensation and evaporation may therefore be treated with the theory of classical thermodynamics.

5.3.1 Thermodynamics of chemical equilibrium

From the first and second law of thermodynamics, the infinitesimal change in energy (dE) may be formulated (eq. 5.3). In equation 5.3, T is the temperature, dS the change in entropy, p the pressure, dV the change in volume, μ_i is the chemical potential of the species i and dn_i is the change in the number of moles of the species i and r is the total number of species.

$$dE = TdS - pdV + \sum_{i=1}^{r} \mu_i dn_i \quad \text{EQ 5.3}$$

For a chemical specie existing in two phases, the partitioning between the phases may be derived by consideration of the total E, S, V and n. These are extensive functions and may therefore be written as the sum of the phases, denoted by an α (eq. 5.4).

$$E=\sum_{\alpha=1}^{\nu} E^{(\alpha)} \quad S=\sum_{\alpha=1}^{\nu} S^{(\alpha)} \quad V=\sum_{\alpha=1}^{\nu} V^{(\alpha)} \quad n_i=\sum_{\alpha=1}^{\nu} n_i^{(\alpha)} \quad \text{EQ 5.4}$$

The displacement from the equilibrium state of the two phase system may thus be calculated from equation 5.3 and 5.4 (eq. 5.5) where the condition for equilibrium states that any change away from equilibrium increases the energy of the system, $(\delta E)_{S,V,n_i} \geq 0$ where the subscript denotes that δE is a natural function of S, V and n_i.

$$\delta E=\sum_{\alpha=1}^{2} [T^{(\alpha)}\delta S^{(\alpha)} - p^{(\alpha)}\delta V^{(\alpha)} + \sum_{i=1}^{r} \mu_i^{(\alpha)} dn_i^{(\alpha)}] \quad \text{EQ 5.5}$$

Thus, at equilibrium, $T^1=T^2$, $p^1=p^2$, $\mu_i^1=\mu_i^2$ are satisfied. If the system is not fully at equilibrium, the system may still be in either thermal, mechanical or chemical equilibrium. It follows that T, p and μ_i are constant within each phase.

In the discussion of chemical equilibrium, the Gibbs free energy is a mathematical concept which simplifies the understanding. The Gibbs free energy (G) is the Legendre transform of E_{S,V,n_i} to a description of the energy of a system based on the variables T, p and n_i (eq. 5.6). The differential of G is shown in equation 5.7.

$$G = E - TS + pV \quad \text{EQ 5.6}$$

$$dG = -SdT + Vdp + \sum_{i=1}^{r} \mu_i \, dn_i \quad \text{EQ 5.7}$$

Using equation 5.6 and 5.7 and applying Euler's theorem for first order homogeneous functions, it may be shown that the Gibbs free energy is the sum of all $\mu_i n_i$ (eq. 5.8).

$$G = \left(TS - pV + \sum_{i=1}^{r} \mu_i n_i\right) - TS + pV = \sum_{i=1}^{r} \mu_i n_i \quad \text{EQ 5.8}$$

Equation 5.7 and 5.8 apply in general and considering a system with constant T and p, the equilibrium condition is $dG \leq 0$ towards equilibrium implying that the equilibrium of the system is found in the point where G is minimum (Chandler, 1987).

From the description so far, which is described in detail by e.g. Chandler (1987), the partitioning between phases may thus be understood as the system's tendency to decrease its Gibbs free energy. Applied to the atmosphere, Seinfeld and Pandis (2006) offer a detailed analysis of the processes determining the equilibrium concentrations and mass transfer between the phases.

In the atmosphere, aerosol particles may be both solid particles and liquid solutions. Due to the high concentration of water vapour present in the atmosphere, liquid solutions are often aqueous solutions including several chemical species (e.g. sulphate, ammonium, etc.). Cloud droplets are just one example of an aqueous solution found in the atmosphere.

In an ideal solution the chemical potential of a specie i may be determined from equation 5.9, where μ_i^* is the chemical potential the pure specie i, R is the gas constant and x_i the mole fraction of the substance i ($x_i = n_i / n_T$ where n_T is the total number of moles in the solution).

$$\mu_i = \mu_i^*(T, p) + RT \ln x_i \quad \text{EQ 5.9}$$

From equation 5.9 the relation between the vapour pressure of the gas i (p_i) and its mole fraction may be determined (eq. 5.10). In equation 5.11, μ_i^o is the standard chemical potential of the specie in the gas phase defined at a pressure of 1 atm, $K_i(T,p)$ is constant for constant temperature and pressure. If $x_i = 1$ and treating both the atmosphere and the solution as ideal, equation 5.10 may be simplified since K_i is equal to the vapour pressure of the pure component, p_i^o (eq. 5.11). This equation is known as Raoult's law. Raoult's law is also applicable to the solvent in a dilute solution. The solute is instead determined by Henry's law (eq. 5.12).

$$p_i = \exp\left(\frac{\mu_i^* - \mu_i^o}{RT}\right) x_i = K_i(T, p)\, x_i \quad \text{EQ 5.10}$$

$$p_i = p_i^o \, x_i \quad \text{EQ 5.11}$$

$$p_{\text{solute}} = H'_{\text{solute}} \, x_{\text{solute}} \quad \text{EQ 5.12}$$

For a non ideal solution, a correction is usually made by introducing an activity coefficient γ_i before the mole fraction x_i in equation 5.9.

The equations 5.9 – 5.12 offer tools with which the mole fraction of different species in the aqueous and liquid phase may be determined. Another effect largely determining the vapour pressure of molecular species is the curvature of the interface between the particle or liquid drop and the atmosphere. This effect, the Kelvin effect, considers the differences in the attractive forces between molecules on the surface of a particle with a flat or curved surface. Physically the effect of the curvature may be understood as arising from an increased distance between molecules on the surface. This decreases the attractive forces, allowing molecules to easier escape the particle to the gas phase. The vapour pressure over a curved surface is therefore always greater than over a flat

surface. The Kelvin equation describes the vapour pressure over a curved surface (eq. 5.13). In equation 5.13, p_A is the vapour pressure over the curved surface, p_A^o the vapour pressure over a flat surface, M is the molecular weight of the substance, ρ_l is the density of the specie in the liquid phase, R_p is the radius of the particle and σ the surface tension.

$$p_A = p_A^o \exp\left(\frac{2\sigma M}{RT\rho_l R_p}\right) \quad \text{EQ 5.13}$$

It is seen from the Kelvin equation that the vapour pressure increases with the molecular weight of the condensing molecule while decreases with an increased radius of the particle. Therefore, the Kelvin effect is also mainly important for small particles and for an aqueous solution it becomes appreciable for particle radii below 50 nm (Seinfeld and Pandis, 2006).

5.3.2 Growth of particles by condensation

Atmospheric particles are unlikely to be found in a stable equilibrium between the gas and particulate phase. Increased emissions and concentration of trace gases (described in chapter 5.4) with low volatility will result in mass transfer to the particulate phase (condensation) while the decrease in these emissions and subsequent lowered concentration in the gas phase will result in a mass transfer to the gas phase (evaporation). In such a system, the size of the particles is directly related to the rate of change of mass between the phases.

The change in mass over time of a particle with diameter D_p due to the condensation or evaporation of molecular species i is described by equation 5.14: D_i is the diffusion coefficient and M_i is the molecular weight of the of the molecular specie i, p_i is the vapour pressure far from the particle and $p_{eq,i}$ is the equilibrium vapour pressure and $f(\mathrm{Kn}, \alpha)$ is a correction factor due to non-continuum effects.

$$\frac{dm}{dt} = \frac{2\pi D_p D_i M_i}{RT} f(\mathrm{Kn}, \alpha)(p_i - p_{eq,i}) \quad \text{EQ 5.14}$$

From equation 5.14 the time evolution of a particle size distribution due to condensation and evaporation may be formulated (eq. 5.15). Equation 5.15 is known as the condensation equation, here formulated in terms of the particle diameter. In equation 5.15, $n_D(D_p,t)$ is the aerosol number distribution function over time and I_D (eq. 4.16) is the rate of diameter change with time due to the condensation and evaporation. The parameter I_D is closely related to equation 5.14. ρ_p in equation 5.16 is the density of the particle.

$$\frac{\partial n_D(D_p,t)}{\partial t} + \frac{\partial}{\partial D_p}[I_D(D_p,t) n_D(D_p,t)] = 0 \quad \text{EQ 5.15}$$

$$I_D(D_p,t) = \frac{dD_P}{dt} = \frac{4D_i M_i}{RT D_p \rho_p} f(\mathrm{Kn}, \alpha)(p_i - p_{eq,i}) \quad \text{EQ 5.16}$$

An important conclusion from the solution to the condensation equation is that the diameter of small particles will increase faster than the diameter of large particles. Therefore, in the absence of other perturbations to the aerosol size distribution (e.g. coagulation or NPF), the distribution becomes narrower over time (Seinfeld and Pandis, 2006).

5.4 Trace gases and aerosol chemical composition

The dry atmosphere contains mainly Nitrogen, Oxygen and a small concentration of the noble gas Argon. The concentration of water, being able to exist in all three phases, varies greatly in the atmosphere from less than 1‰ to about 5% in hot and humid air (Wallace and Hobbs, 2006).

Other gases in the atmosphere are referred to as trace gases. These gases contribute to less than 1% of the total mass of the atmosphere and includes green house gases e.g. carbon dioxide, methane, nitrogen dioxide etc. The trace gases can for simplicity be grouped according to their chemical compositions. Hydrogen compounds, e.g. the hydroxyl radical (OH) and hydroperoxyl (HO_2), are some of the most important oxidants in the atmosphere (Wallace and Hobbs, 2006). Table 1 displays typical groups of atmospheric species, typical chemical species and their typical sources.

Dimethyl sulphide (DMS) is an important specie and the dominant sulphur compound emitted from the oceans. Kettle et al. 1999 found globally, in agreement with earlier regional studies, strong indications that DMS concentrations in the ocean surface waters are correlated to the marine phytoplankton concentration. DMS is a short lived atmospheric specie and is quickly oxidized by the hydroxyl radical making DMS the dominant source of Sulphur dioxide (SO_2) in the marine atmosphere. Atmospheric nitrogen-containing compounds are mainly Nitrous oxide (N_2O), nitric oxide (NO) and nitrogen dioxide (NO_2) termed NO_x, nitric acid and ammonia (NH_3). Nitrogen compounds are essential for all living organisms and N_2O is a strong green house gas. Carbon-containing compounds include for example carbon monoxide (CO), CO_2, alkanes (e.g. CH_4), aromatics, aldehydes and ketones. Commonly all atmospheric organics except CO and CO_2 are grouped and termed Volatile organic compounds (VOCs). In the case of biologically emitted VOCs, these carbon compounds are referred to as biological VOCs (BVOCs) (Seinfeld and Pandis, 2006).

Table 3: Grouping of trace gases, examples of chemical species and sources. Adopted from Seinfeld and Pandis, 2006.

Group	Examples of chemical species	Sources
Sulphur compounds	SO_2, SO_4, H_2S, H_2SO_4, CH_3SCH_3 (DMS), OCS	**Natural** Oceans, volcanoes **Anthropogenic** Fossil fuel, biomass burning
Nitrogen compounds	N_2O, NO_2, NO, NH_3, HNO_3	**Natural** Soils, oceans **Anthropogenic** Agriculture, fossil fuel combustion, biomass burning
Carbon compounds	CO, CO_2, hydrocarbons, VOCs, BVOCs	**Natural** Vegetation, oceans, wetlands, termites etc. **Anthropogenic** Biomass burning, fossil fuel combustion, agriculture
Halogen compounds	Halocarbons, Chlorofluorocarbons, $CFCl_3$, CF_2Cl_2, CH_3Cl, CH_3Br	**Natural** Vegetation, oceans, wetlands, fungi **Anthropogenic** Industrial, coal combustion, incineration, agriculture

In the previous chapter (5.3) it was described how gases may partition between the phases by condensation and evaporation. Molecular species mentioned in this chapter with a low volatility may therefore condense on particles and contribute significantly to the mass of the particles.

As an example, sulphate aerosols consists of sulphuric acid particles which have been neutralized by ammonia and are to a large extent secondary aerosols produced in the atmosphere from nucleation of gaseous precursors. The sulphur-containing gaseous precursors are anthropogenic emissions of SO_2 from fossil fuel combustion, natural emissions from volcanic eruptions and biogenic DMS produced by marine phytoplankton. Sulphate is formed from gas phase reactions

where SO_2 is oxidized by OH, forming sulphuric acid (H_2SO_4) or by condensing on existing mineral or sea salt aerosols. H_2SO_4 is believed to participate in both homogeneous nucleation with H_2O and heterogeneous nucleation with NH_3 (O'Dowd, 2007). A different path for sulfate aerosol formation is through aqueous reactions in cloud droplets (IPCC, 2007).

5.5 New particle formation

New particle formation involves the nucleation of particles directly from condensation of chemical species in the gas phase and a rapid (nm h^{-1}) growth of the newly formed particles by condensation. The initial nucleation of particles and subsequent growth are most likely two separate processes with different chemical species responsible for the nucleation and the growth of the particles respectively (Kulmala et al., 2013). There is of yet no complete theoretical description accurately describing both the nucleation and growth of particles. Hence, empirical studies usually form the basis for the reported derivations of nucleation rates, growth rates and what chemical compounds are participating in the nucleation.

However, nucleation theory predicts the homogeneous formation of molecular clusters through the random collisions of molecules. These clusters may grow to critical sizes where the growth of the cluster becomes determined of one or a few vapour species. The critical size of the cluster may briefly be understood as the point where the growth to larger sizes permits the cluster to overcome a nucleation barrier, thought of as a local maximum in the Gibbs free energy of the cluster. After reaching the critical size, clusters may become stable and grow spontaneously by condensation of vapour species. If only one chemical specie is responsible for the growth of the stable clusters, the homogeneous nucleation is termed homomolecular while if several species participate in the growth is termed heteromolecular (Zhang et al., 2012). For nucleation in the atmosphere, empirical studies have indicated that the nucleation is always heteromolecular and that the critical size of the clusters is close to 1.5 nm (Zhang et al., 2012).

The rate at which stable clusters are formed at 1.5 nm in diameter is generally termed the nucleation rate ($J_{1.5}$) and is determined by the presence of chemical species with low vapour pressure. The important chemical species involved in atmospheric nucleation are most often sulphuric acid and different organics, e.g. amines (Kulmala et al., 2013).

Although the nucleation of atmospheric vapours is heteromolecular, the derivations of the nucleation rate from observations suggests that the nucleation rate may in many cases be well represented by H_2SO_4 as the only vapour specie involved in the nucleation. The parametrisation of the nucleation rate in equation 5.17 is proportional to the concentration of H_2SO_4 in the gas phase to the power of a constant α. It has been shown that α generally takes values between 1 and 2 (Kulmala et al., 2006). The constant K in equation 5.17 is the nucleation coefficient determined experimentally. The large variations in K (an order of magnitude) measured by Paasonen et al., 2010 (for α=1) is a strong indication that more species do participate in the nucleation. Parametrisations of the nucleation rate including different organics are available but with a low level of theoretical understanding, implying that uncertainties are large.

$$J_{1.5} = K[\mathrm{H_2SO_4}]^{\alpha} \qquad \text{EQ 5.17}$$

In order to estimate the growth of the nucleated particles and the effect on the aerosol size distribution, particle losses due to coagulation as well as the rate of condensing vapours on all particles present in the aerosol must be accounted for. Therefore, NPF is rarely observed if there is a large accumulation mode on which the stable clusters may coagulate, rather than grow to larger sizes by condensation. Similarly, NPF is decreased if the condensing vapour easily condenses on a large number of already existing particles. In derivations of $J_{1.5}$ from observations, these effects are accounted for.

The large uncertainties in the mechanism behind particle nucleation and the participating vapours creates challenges when modelling NPF with atmospheric aerosol models such as the ADCHEM model (chapter 6.6). Since such models are based on airmass trajectories, the geographical area over which the airmass travels during a simulation may be large. Thus, it is possible that the nucleation mechanism that best describes nucleation may changes during the time of a single simulation. This risk is perhaps most prominent if the concentration of gaseous species with low volatility also changes drastically along the trajectory.

6 Methodology

6.1 Scientific method and overview

To investigate the aims of this project, two different methods were applied and the project separated in two parts:

Task 1. In order to address the first aim, measurements of the particle number size distributions at several coastal sites were analysed and days with NPF were determined. The data were further analysed using a method known as the NanoMap method, in order to deduce the frequency and estimate the probability of NPF in the atmosphere over marine areas.

Task 2. To address the second aim, NPF was simulated with a chemical box model using meteorological data, regional anthropogenic emission sources and satellite data of algae bloom. The conditions were simulated to specifically address the anthropogenic influence on new particle formation in marine areas.

6.1.1 Task 1 - Frequency of marine NPF

In the first method, aerosol data gathered from three coastal measurement sites during time periods ranging from three months to several years were analysed. The data were used to infer the NPF frequency and probability over marine areas using the NanoMap analysis method. The NanoMap analysis is further described in chapter 6.4 and includes also a discussion of the parameters largely influencing the NanoMap results (chapter 6.5).

The NanoMap analysis requires input of when NPF events were observed at the measurement site. Therefore, the measurement data were classified into event days and non-event days for the full time period of the measurements. The procedure of the classification method is described in chapter 6.3. The NanoMap analysis also requires airmass backward trajectories to be calculated in advance. The method with which the trajectories were calculated is described in chapter 6.2.

In order to compare the NanoMap analysis and the observed NPF at the measurement sites, statistics of aerosol number size distributions and event statistics were also analysed for each measurement station. These statistics are also important for a comparison to other measurement sites and simplifies the interpretation of the NanoMap results. The stations at which data were collected are described in chapter 7 and the event statistics are included in the results (chapter 8.1).

6.1.2 Task 2 - Anthropogenic impact on NPF in marine areas

In the second method, the aerosol dynamics and gas phase chemistry model ADCHEM was used to simulate NPF. The ADCHEM model was used to simulate NPF and aerosol dynamics during 14 airmass trajectories all passing over the measurement station in Høvsøre, Denmark, with three hour intervals. These trajectories were used to construct a particle number size distribution at Høvsøre, used for comparison and estimation of both model accuracy and the sources influencing the NPF.

In order to answer the second aim, two different emission scenarios together with the 14 trajectories were simulated. In the first scenario, all emissions available were included. In the second scenario, anthropogenic marine emissions were not included. These scenarios were compared in order to qualitatively assess the anthropogenic influence on coastal NPF. Furthermore, the geographical location of all NPF modelled by ADCHEM in the two scenarios were compared in order to estimate also the anthropogenic impact on NPF in the marine atmosphere.

The ADCHEM model is briefly described in chapter 6.6 together with a description of the marine isoprene emission model developed in this project.

6.2 Airmass trajectories

An airmass trajectory may be described as the paths an air parcel take, or in more detail, the time integrated advection following an air parcel or a particle. Backward trajectories follow the air parcel or particle backwards in time from the initial starting position while a forward trajectory calculates the path travelled after the initial starting position.

Both the NanoMap analysis and the ADCHEM model requires airmass backward trajectories to model the NPF events. These backward trajectories were calculated using meteorological input from the National Weather Service's National Centers for Environmental Prediction (NCEP) called GDAS (Global Data Assimilation System) and the HYSPLIT model (Hybrid Single-Particle Lagrangian Integrated Trajectory) provided by the NOAA (National Oceanic and Atmospheric Administration).

In this project the trajectories were calculated using the HYSPLIT model. The model requires input of a three-dimensional wind velocity field, $\mathbf{V}=(U,V,W)$ where U,V are the horizontal wind speeds and W the vertical wind speed. The advection of an air parcel is calculated from the average of the velocity vectors for both the initial position $P(t)$ and the first guess position $P'(t+\Delta t)$. The first guess position is the calculated position using only the velocity of the initial position. The calculation of the final position of the next time step is shown in equation 6.1 (Draxler and Hess, 1998).

$$P(t+\Delta t)=P(t)+0.5[\mathbf{V}(P,t)+\mathbf{V}(P,t+\Delta t)]\Delta t \qquad \text{EQ 6.1}$$

The trajectories may have large errors which increases with the distance upwind or downwind of the initial starting position. The errors associated with an airmass trajectory results in an error of the air parcel position of approximately 20% of the distance travelled (Stohl, 1998). The influence of trajectory uncertainty on the NanoMap results is addressed further in chapter 6.5.4.

6.3 Task 1 - Classification method

To separate NPF days from non-event days, no simple reliable automatic routine is available. The classification of NPF events was therefore done manually.

Dal Maso et. al (2005) have worked out a classification scheme for regional particle formation events measured by an SMPS or DMPS. Furthermore, Vana et. al (2008) extended the classification for use with AIS data and local formation events. An overview of the classification is given in table 4.

When only SMPS data were available, the classification of Dal Maso et. al (2005) has been used. For time series including AIS measurements, both classification methods have been used. AIS data alone is not considered suitable for event classification due to technical limitations of the instrument.

The criteria which has to be met in order for a day to be qualified as a NPF event is shortly summarized by Dal Maso et. al (2005) as:

1. A distinct new mode of particles must appear in the size distribution.
2. The mode must start in the nucleation mode size range (<25 nm).
3. The mode must prevail over a time span of hours.
4. The new mode must show signs of growth.

In order to minimize subjective opinions, a panel of two or more persons should perform the classification. Any day when the panel initially disagree should be revised and if the disagreement concerns event/non-event, the day should be classified as undefined. The undefined class is included to eliminate false positives, i.e. non-event days classified as event days. Although

undefined days therefore likely also contains some false negatives, i.e. event days classified as non-event, it is very unlikely that non-events have been misclassified as event days (Kristensson et al 2008). Bad or missing data which significantly affect the classification of an event/non-event, result in the day being classified as "bad data". In such a case, the day is not considered in further analysis.

Vana et al (2008) classifies events into five classes and one non event class. The classes have been given characteristic names for their appearances: class I, banana-type; class II, hump type; class III, apple-type; class IV, mixed-type and class V, rain-events.

In this study, days were classified according to both methods. However to be compatible with NanoMap, all days were finally classified into the following four events: (1) non-event, (2) undefined, (3) class II and (4) class I (see mid section table 4).

Table 4. Classification of events, procedure by Dal Maso et al. (2005) (left) and Vana et al. (2008) (right). The middle section shows the classification adopted from the two procedures. Class II-IV of the classification by Vana et al. (2008) may be grouped either as undefined, class II or class I.

Dal Maso et. al (2005)	**Event classification**	**Vana et. al (2008)**
No sign of NPF.	**Non-event**	No sign of NPF. **Class V, rain-induced events**
Undefined: If the panel could not agree on event/non-event, the day will be classified as undefined.	**Undefined** e.g. nucleation mode without growth.	**Class II, hump-type events:** distinct new mode appear in the size range of intermediate air ions, nucleation starts from the cluster ion region. **Class III, apple-type events:** distinct new mode appear in the size range of intermediate air ions with a clear gap between the cluster and intermediate ion modes.
Class II: Days when the derivation of the formation and growth rates was not possible or the results were questionable.	**Class II** e.g. days with strong fluctuations in the growing mode.	**Class IV, mixed-type events:** formation of intermediate air ions clearly observed but not possible to classify as a banana, hump or apple event.
Class Ia & Class Ib: Days when the growth rate and formation rate could be determined with good confidence level.	**Class I** e.g. days with clear growth and characteristic banana shape.	**Class I:** Days with a distinct new mode of particles in the intermediate air ion size range (1.6-7nm). Formation of particles and subsequent continuous growth to larger sizes for several hours.

In the case for which both AIS and SMPS data were available, class I events also included hump, apple and mixed events that show continuous growth to larger particles for several hours. The particle formation events in this study are furthermore assumed to occur over geographically large areas of in general several 100 kilometres. Days classified as "rain events" measured by the AIS instrument hence do not qualify as event days but may be of interest for statistical purposes.

6.4 Task 1 - NanoMap method

The NanoMap analysis aims at increasing the geographical understanding of aerosol number and size distributions and is available as an open source Matlab program developed at Lund University. Based on meteorological backward trajectories and single point measurements of particle number size distributions, NanoMap enables the determination of where new particle formation takes place at the point of formation of 1.5 nm in particle diameter and at distances up to at least 500 km from the measurement site. Increasing the understanding of the spatial distribution of NPF will allow better parametrisation in climate models and permit more detailed studies of the relative impact from anthropogenic emissions on secondary aerosol formation.

The NanoMap method relies on the simultaneous event assumption which implies that the measured NPF is a regional event with the start of the nucleation time and end of nucleation time constant over the full area covered by the regional NPF event.

To calculate the extent of a regional NPF event, the NanoMap method utilizes airmass backward trajectories together with particle number size measurements. The general procedure and resulting geographical plots produced by NanoMap are described in this chapter. A sensitivity analysis intended to highlight uncertainties and improve the results produced by NanoMap is given in chapter 6.5.

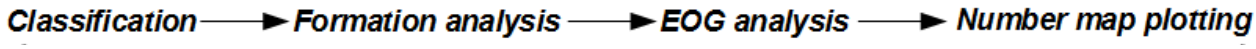

Figure 7: The NanoMap procedure.

The NanoMap procedure is divided into four separate parts: (1) event classification, (2) formation time analysis, (3) end of growth (EOG) analysis, (4) Number map plotting. These parts are depicted by the flowchart in figure 7. Besides the Number map plotting, a method for calculating the probability of NPF in a grid cell has been developed during this project. The event probability calculation is described in further detail in chapter 6.4.5.

6.4.1 Classification

The first part, the classification of measurement data, is previously described in chapter 6.3. In this study, only class I events showing distinct new particle formation were used in the NanoMap analysis since the resulting degree of accuracy using class II events in the NanoMap analysis may be questionable.

6.4.2 Formation time analysis

The formation time analysis is done manually and consists of choosing the start time of the NPF (formation start time) and the ending time of the NPF formation (formation end time). The process is exemplified in figure 8. Since NPF occurs at an approximate particle diameter of 1.5 nm, the formation start time of the NPF event is chosen as the time when the particle concentration in the lowest size bin first starts to increase above the normal background concentration. In an identical approach to the formation start time, the formation end time is taken to be the time when the particle formation ends and the concentration of the lowest size bin returns to the background concentration.

All instruments measuring particle number size distributions may not able to measure particles as small as 1.5 nm in diameter for which the stable clusters are formed. If the instrument recording the NPF has a smallest size bin larger than the diameter at which the stable clusters form, the formation time also has to be extrapolated backwards in time. In order to do the extrapolation the growth rate

of the particles from 1.5 nm to the smallest size bin of the instrument must be estimated.

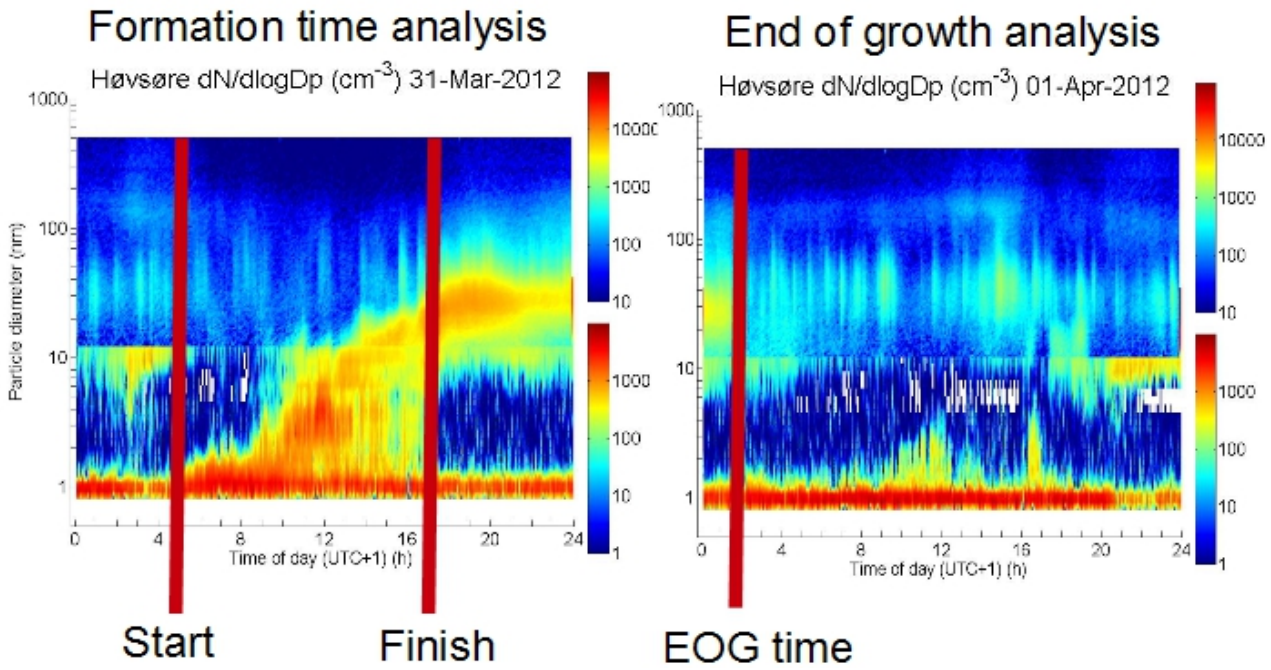

Figure 8: Data showing a class I event in Høvsøre, Denmark between the 31st of March 2012 and 1st of April 2012. The formation start and end times and EOG time are represented by the red lines.

In this project the only measurement station that had a smallest size bin larger than 1.5 nm was Preila. Thus it was estimated from the results of Kulmala et al. (2004) that the growth rate from 1.5 nm to 8 nm was 2 nm h^{-1}. The formation time was then assumed to have occurred approximately three hours earlier.

6.4.3 End of growth analysis

In the third part, the end of growth time of the measured nanoparticles is chosen. The EOG time is the time for which the growing mode can no longer be followed in the measured spectrum. Often, the EOG time is clearly visible due to a change of air mass or when the growing mode of particles once again reaches background concentrations (figure 8). However sometimes, the EOG time can be obscured by bursts of primary particles from e.g. local pollution which can make the determination of the EOG time difficult. The end of growth time greatly influences the NanoMap results as it sets the limit of how far away from the measurement station a NPF event may be inferred. This is in most cases however only the maximum extent of the NanoMap results; in reality the NPF is likely larger. The sources influencing the EOG time are discussed in more detail in the NanoMap sensitivity analysis (chapter 6.5.2).

6.4.4 Number map plotting

The fourth part in the NanoMap method is the determination of the geographical position of the new particle formation using meteorological backward trajectories. At a specific time between the formation ending time and the EOG time, the grown particles as observed at the measurement site can be followed backwards with the trajectories to their place of formation at 1.5 nm diameter, during the time when they were formed between the formation start and ending time.

Since the resolution of the backwards trajectories is normally one hour, the geographical position of the formation can be determined for each hour between the formation end time and the EOG time. The geographical position of the formation deduced from the EOG time determines the horizontal

extent of the formation.

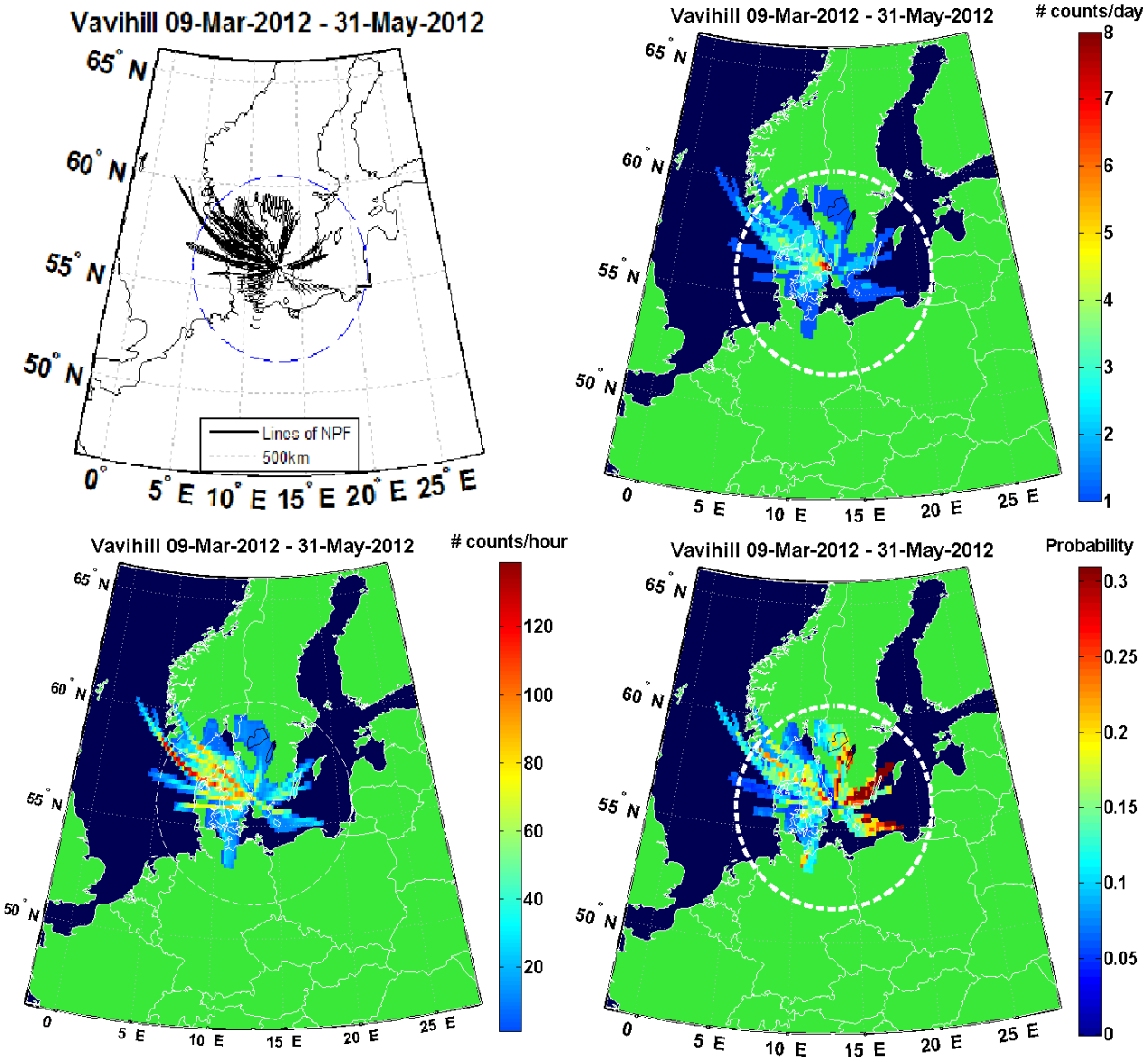

Figure 9: Illustration of the NanoMap results plotted in four different ways. Measurement data and results from Vavihill field station (56°0'36"N, 13°5'24"E) using HYSPLIT backward trajectories and DMPS size measurements with a time resolution of 10 minutes and size resolution of 3-900 nm (Kristensson et al., 2008). ***Top left:*** *Line plot.* ***Top right:*** *grid plot displaying the number of events per day in each grid cell.* ***Bottom left:*** *grid plot displaying the number of events per hour in each grid cell.* ***Bottom right:*** *Probability of NPF event in each grid cell.*

The resulting plot is the final NanoMap result which may be displayed in several different manners of which four are described here and exemplified in figure 9. For relatively short time series, the results may be displayed as lines giving a clear overview of the NPF event (figure 9, top left). For longer time series the Number map plot may be presented in a gridded format with a user defined resolution. The NanoMap results in this project are presented in the gridded format with a resolution of 0.2 degrees. In the grid format, a trajectory passing over a grid cell will result in a "grid count". These grid counts may be used to present either the number of days with an event (figure 9, top right), the number of counts per hour (figure 9, bottom left) or the probability of NPF events to occur in a grid cell (figure 9, bottom right). For instructions on how the probability of NPF is calculated, please see section 6.4.5.

The meteorological backward trajectories in this work have been calculated using the HYSPLIT model and meteorological data input from GDAS (1° resolution). Trajectories from HYSPLIT and GDAS have been used in earlier NanoMap studies with good results (Kristensson et al., 2014). The temporal resolution of the trajectories is one hour which allows the NanoMap results to be plotted with an hourly resolution. Since generally there is either one NPF event or none recorded per day, the number of counts in each grid cell is also set to either one per day or none, although the total number of counts in that grid cell from all trajectories during the same day may be higher. The same applies to hourly resolved grid plots. This procedure ensures that the latitude and longitude data may be interpolated to any extent without over counting the number of events in a grid cell. In the final gridded NanoMap results, the latitude and longitude data of the inferred NPF events are interpolated in order to fill also all grid cells that are intermediate two grid cells where NPF was inferred.

6.4.5 Event probability calculation

To obtain the probability plot it is necessary to estimate the number of trajectories that passes the same grid cell without any NPF. This is done through an analysis of the complete number of trajectories passing the grid cell during the measurement period. However, this number of trajectories may be reduced. The NanoMap method also provides information regarding what time during the day NPF may be observed at the station. Therefore, by analysing the formation start time and end time, it is often clear that NPF only occurs during certain hours of the day, often corresponding to the daylight hours. Hence, instead of all trajectories, only those within the observed formation period at the station are chosen. The grid produced shows thus the distribution of all trajectories within the formation time and per day. In this procedure, the maximum grid count per day is one.

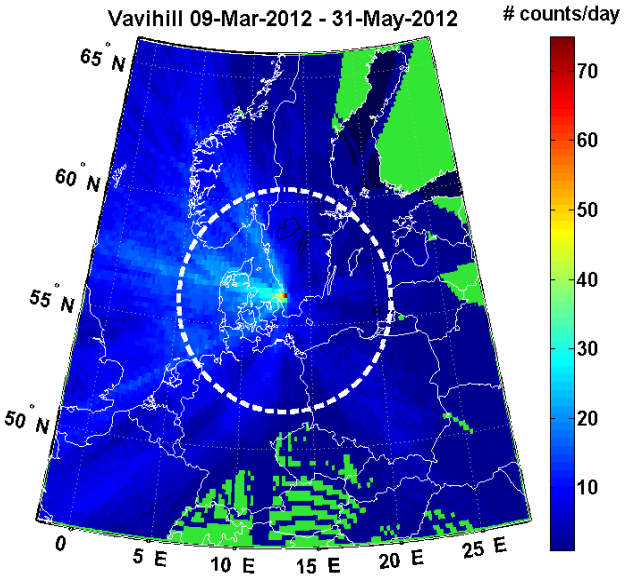

Figure 10: All trajectories within the formation start time and end time, both during and without NPF, starting from Vavihill and 72 hours backwards.

Figure 10 displays a trajectory analysis, where the colorbar represents the number of grid counts from all trajectories between 6 am and 8 pm and per day. To calculate the daily chance of NPF in the grid cells, the grid representing the number of NPF events per day is divided by the grid of all trajectories within the formation time and per day. This is illustrated by equation 6.2 where $Z_{probability}$ is the new probability grid, Z_{event} is the event per day grid, $Z_{FST\text{-}FET}$ is the grid representing one day

from all trajectories within the formation start time (FST) and formation end time (FET) and N_{days} is the number of days analysed. The numerator in equation 6.2 is illustrated in figure 9, top right, while the denominator is the result shown in figure 10.

$$Z_{\text{probability}} = \frac{\sum^{N_{\text{event days}}} Z_{\text{event}}}{\sum^{N_{\text{days}}} [Z_{\text{FST-FET}}]} \qquad \text{EQ 6.2}$$

The final result of the probability calculation can be seen in Figure 9, bottom right in the previous section.

6.5 NanoMap sensitivity analysis

As discussed in Kristensson et. al (2014) there are at least seven factors that influence the precision of the NanoMap results. Five of these are discussed in this chapter. These are:

1. The event classification.
2. The EOG time.
3. The simultaneous event assumption.
4. Trajectory calculations.
5. The grid resolution.

6.5.1 Event classification

The classification of event procedure developed by Dal Maso et al. (2005) and Vana et al. (2008) both include subjective choices in the process. This subjectiveness can result in a misclassification of the class I events used in the NanoMap plots. If for example some class II events, which can have a higher uncertainty in both growth rate, formation time and EOG time, are systematically misclassified as class I events the resulting NanoMap plot will be smeared out. A too cautious classification with possible type I events downgraded to type II events may instead lead to missing data and yield areas of very low or no NPF, whilst a more aggressive classification could show considerable NPF in those areas.

6.5.2 The EOG time

The EOG time can not always be chosen with a satisfactory accuracy. Since the EOG time sets the number of trajectories which are to be plotted for an event as well as the observable horizontal extent of an event, the EOG time is an essential parameter for the Nanomap results. The difficulty of choosing the EOG time arises from different sources and may cause the EOG time to be both underestimated and overestimated. Meteorological conditions causing strong turbulence, convection or sudden shifts in wind direction may abruptly change the airmass origin. After such an airmass change, it might be difficult to identify the continuation of the event. Conversely, primary particle emissions may in some cases conceal the true EOG time by the addition of a similar number of particles at a similar size as the recently formed particles during a NPF event. When the EOG time is underestimated, information regarding the geographical extent of the event is lost. On the other hand, an overestimation of the EOG time imposes an error and leads to higher grid counts or probability than with a more correct EOG time.

6.5.3 The simultaneous event assumption

The simultaneous event assumption employed in the NanoMap analysis implies that the start and end time of the formation event are the same over the entire area upwind of the station. Local fluctuations in the formation time of the regional NPF event is therefore not accounted for. Since regional differences in meteorological conditions and concentrations of nucleating vapours may be considerable, this assumption can give significant uncertainties to the results of where NPF take

place. To consider all these conditions would demand the modelling of all parameters that influence the nucleation. Such large scale modelling is extremely time consuming and with several uncertainties. Therefore, it is not motivated to take this potentially large error into account in the analysis made in this project.

6.5.4 Airmass backward trajectories and grid resolution

Airmass trajectories are essential in the derivation of the NanoMap results. The uncertainty of the trajectory position results in an uncertainty of the position of the inferred geographical location of the NPF. Furthermore, the trajectories yield NPF along a line, neglecting horizontal diffusion along the trajectory. Horizontal diffusion along a trajectory should result in wider areas where NPF takes place. This area would also increase further upwind of the station.

Since the uncertainty thereby grows with the distance from the station, backward trajectories should not be followed too far. Airmass trajectories have been shown to have errors in the position corresponding to approximately 20% of the distance travelled from the initial starting position (Stohl, 1998). It is therefore justified to question the use of trajectories which do not include diffusive processes. It is possible to calculate backward trajectories including diffusion, for example with the FLEXPART model (e.g. Stohl et al., 2005). The aim is also to be able to utilise the trajectories including diffusion in the Nanomap model. However, implementing the FLEXPART model trajectories in the NanoMap model requires much work and is therefore a future project. With an approximate trajectory uncertainty of 20% and a trajectory at 500 km distance from the initial position corresponds to approximately 100 km uncertainty in the position. In most cases in this project, except where the trajectory follows close to the coast line, this uncertainty is well within the precision needed to determine if the NPF occurs over land or over marine areas.

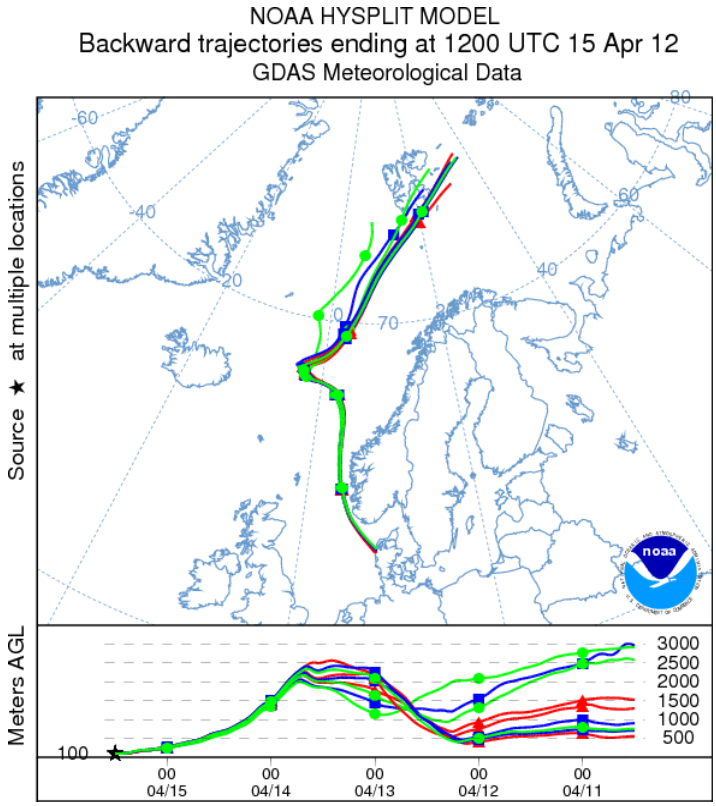

Figure 11: HYSPLIT multiple trajectory plot. The initial coordinates are varied by approximately 0.1 degrees starting from 100 m.a.s.l. Source: Draxler et al., 2013.

Diffusion is one parameter which influences the accuracy of the trajectory. Considering also the

uncertainties in the meteorological input data, the uncertainty of the trajectories in specific trajectory runs may be evaluated by calculating several trajectories with slight variations in their initial positions. This procedure allows the estimation of how far away from the station a trajectory position is accurately predicted. When the trajectories diverge, the accuracy of the initial trajectory is lowered. In figure 11, several trajectories are calculated with less than 0.1° spacing. These trajectories diverge significantly after approximately 36 hours. There are most likely cases for which the trajectories will diverge much faster but there will also be trajectories which do not diverge even after several days. In NanoMap, the time a trajectory is followed is usually ranging from hours to one or two days. The trajectory uncertainty is thus a strong reason to treat NanoMap results which are far away from the measurement site with caution.

The resolution of the grid cells used for the plotting of the NanoMap results largely determines how many grid counts can be expected from two or more overlapping trajectories. A coarse resolution gives a blurred picture with little information of local differences of the number of NPF events. However, a fine resolution may result in too few events overlapping each other and a large underestimation of the event probability. The issue of too fine a resolution arises from the trajectories consisting of longitudinal and latitudinal output data along the line which the airmass follows. Thus, in the current set-up, the trajectory is one dimensional. This implies that the largest two dimensional airmass trajectory is given by the user defined resolution. In this way and without a significant interpolation between grid cells, a very fine grid resolution will result in a geographical map with almost no overlapping of grid counts. It is currently possible to interpolate the trajectory to a satisfactory degree down to approximately 0.1° resolution, but lower resolutions should not be aimed at without rewriting the interpolation routine. The resolution dependence is illustrated in figure 12 displaying NanoMap results for a very coarse and very fine resolution. The resolution in this project (see results, chapter 8.1.2) was set to 0.2°, which often allows local differences to be clearly observed. The loss in data using too fine a resolution could be decreased if dispersion along the trajectory was included.

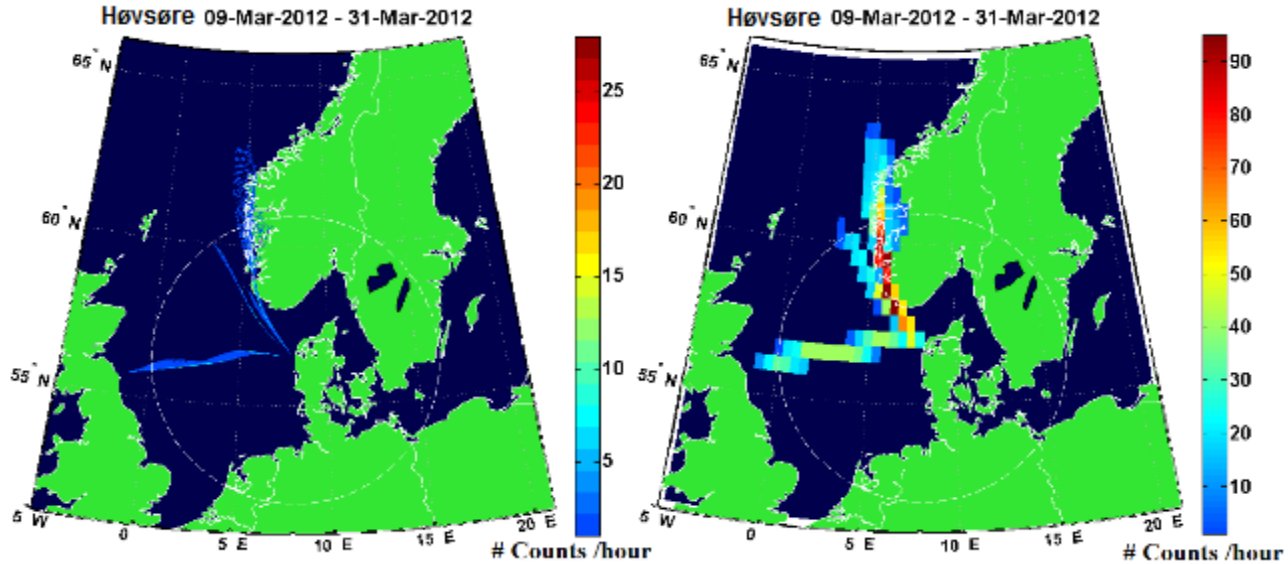

Figure 12: Image displaying the influence of the user defined resolution to the final NanoMap results. Left: very fine resolution. Right: coarse resolution.

6.6 Task 2 - Modelling new particle formation at Høvsøre

Modelling atmospheric properties generally requires a large amount of parameter considerations. To model primary aerosol particles, NPF and secondary organic aerosol formation in order to reproduce the observed particle size distribution at Høvsøre for several consecutive days, requires a mechanistic description of the problem. For this purpose the ADCHEM model was chosen. Using ADCHEM, aerosol properties were simulated along 14 trajectories. These trajectories started 96 hours upwind and ended 48 hours downwind of Høvsøre. The trajectories arrived at Høvsøre with 3 hours interval which allowed the modelling of aerosol properties with a 3 hour resolution. By combing all trajectories, the modelled particle number size distribution at Høvsøre could be obtained. The trajectories are included in appendix A.

In the current project, input data to the model were anthropogenic gas phase emissions and biogenic DMS emissions from the European Monitoring and Evaluation Programme (EMEP), Isoprene emissions from the ocean calculated using satellite chlorophyll-a data, terrestrial biogenic VOC emissions and meteorological conditions from the NCEP.

In order to evaluate the second specific aim (chapter 2), the impact of marine anthropogenic emissions on NPF, the model was run for two different emission scenarios. In the first scenario, the model included all input emissions, both anthropogenic, biogenic and natural. In the second scenario, the model was run excluding all anthropogenic emissions over marine areas. The size distribution of the two simulations was compared with the aim to qualitatively assess the anthropogenic impact on NPF.

The ADCHEM model is amply described in Roldin et al. (2011). However, since the initial ADCHEM version, there have been several adjustments which are described further in Roldin (2013). The next sections aim at giving an overview of the processes simulated by ADCHEM and to describe the steps from model input to model output.

6.6.1 Model description

The ADCHEM model is a process based model which allows the simulation of chemical and physical aerosol properties relevant for climate and health (Roldin, 2013). The original version of the ADCHEM model was set-up as a 2 dimensional model. In the version used for this project, the model was set-up as a 1 dimensional, Lagrangian box model where particles are emitted, formed, transformed and deposited as the volume of air moves along an airmass trajectory. Figure 13 illustrates the model structure and the input to the ADCHEM model. The aerosol processes simulated in the ADCHEM model include primary particle emissions, homogeneous nucleation, condensation, evaporation, coagulation and dry and wet deposition.

In the model, the particle number size distribution is discretized into a finite number of size bins. In each size bin, all particles are assumed to have the same structure and chemical composition. The model uses a full moving structure of the size bins, which allows new size bins to be added as the simulation time increases (Roldin et al., 2011).

Cluster activation theory (Kulmala et al., 2006) was used to represent the homogeneous nucleation, involving sulphuric acid and with stable clusters forming at 1.5 nm ($J_{1.5}$). Due to the large uncertainties and differences between empirically derived values of the nucleation coefficient, this parameter was set conservatively to $5\text{x}10^{-8}$ s^{-1}, which is in the lower range of the values reported in the literature (see e.g. Riipinen et al. (2007) and Paasonen et al. (2010)). The calculation of the number of particles formed by homogeneous nucleation is shown in equation 6.3.

$$J_{1.5} = 5\text{x}10^{-8}[H_2SO_4] \quad s^{-1} \qquad \text{EQ 6.3}$$

Gas phase chemical reactions were simulated with the Master Chemical Mechanism v3.2 (MCM). The MCM is a near explicit description of the chemical mechanisms involved in the degradation of a large number of VOCs. The included species are primarily based on the UK National Atmospheric Emission inventory (Passant, 2002) and includes several anthropogenic VOCs, isoprene and three monoterpenes α-pinene, β-pinene and limonene. The model is based on 17000 elementary reactions and 6700 primary, secondary and radical species. The MCM simulates the concentration of all gas phase species included in the model upon photolysis and oxidation and determines the gas phase concentrations for important species such as sulphuric acid.

The VOCs undergo degradation resulting in a large number of products. For simplicity only those products with a significant mass fraction were further implemented in the ADCHEM model. These products had a total mass fraction of approximately 95 percent. The chemical products with low volatility are most likely the species involved in the growth of the nucleated particles. (The chemical mechanistic information was taken from the Master Chemical Mechanism, MCM v3.2 (Jenkin et al., 1997, Saunders et al 2003, Jenkin et al., 2012), via website: http://mcm.leeds.ac.uk/MCM).

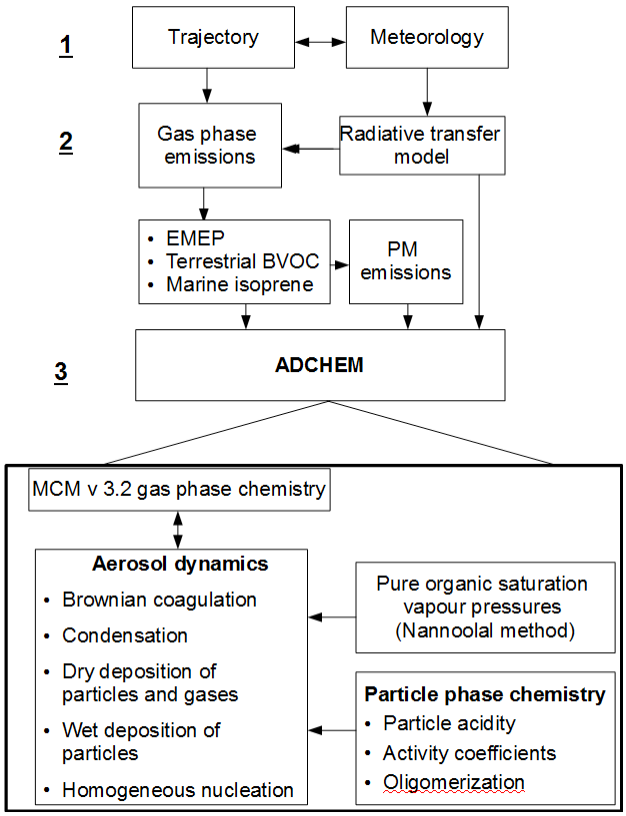

Figure 13: Conceptual model showing the ADCHEM structure.

The partitioning of chemical species between the gas and the particular phase is governed by the saturation vapour pressures of the chemical species and the chemical composition of the pre-existing aerosol particles. The condensation and evaporation model included in the ADCHEM model considers sulphuric acid, ammonia, nitric acid, hydrochloric acid and the oxidation products from the degradation of the VOCs estimated by the MCM. In the model, the gases condense onto a surface layer on the pre-existing aerosol particle. For each included chemical specie is calculated a particle molar growth rate from the consideration of the saturation gas phase concentration of each specie at the particle surface. The saturation vapour pressures of the VOC oxidation products were calculated with the Nannoolal method (Nannoolal et al., 2008) while the corresponding equilibrium

vapour pressures were calculated according to Raoult's law (Roldin, 2013).

Coagulation is a process mainly governed by Brownian diffusion. The coagulation between the modelled particle size bins is calculated from the coagulation sink ($Coag_{\text{sink}}$) and the coagulation source ($Coag_{\text{source}}$). The coagulation source and sink are combined into equation 6.4 which shows the calculation of the new particle concentration (c_i) in the size bin i after coagulation.

$$c_i = c_i + \sum_{j}^{N} [\, y_{1,i,j} \cdot Coag_{\text{source},i,j} + y_{2,i-1,j} \cdot Coag_{\text{source},i-1,j} - Coag_{\text{sink},i,j}] \cdot \Delta t \qquad \text{EQ 6.4}$$

In equation 6.4, $y_{1,i,j}$ and $y_{2,i-1,j}$ is the fraction of the single particle volume of the smaller and larger formed particles respectively, Δt is the model time step. In order to be modelled realistically, coagulation requires not only a model for Brownian coagulation of particles but also the background sources of primary particles to be modelled correctly.

A complete description of the representation of condensation-evaporation and coagulation in the ADCHEM model is beyond the scope of this project and therefore only briefly discussed. The reader is referred to the published works by Roldin (2013) and Roldin et al. (2011) for a complete description. The reader is also reminded of the theory in chapter 5.2 and 5.3.

Dry deposition processes were included in each model time step. The dry deposition is based on a resistance model including two resistances. The transport of particles from the volume of air to the ground is determined by the surface layer resistance (r_a), the quasi-laminar layer resistance (r_b) and the settling velocity (v_s) which becomes important for large particles. The dry deposition loss rate (v_d) is given by equation 6.5 and is a function of wind speed, height over ground of the particle and the stability of the atmosphere. The quasi-laminar layer resistance is calculated differently over land and ocean as a result of the differences between the two surfaces (Roldin et al., 2011).

$$v_d = \frac{1}{r_a + r_b + r_a r_b v_s} + v_s \qquad \text{EQ 6.5}$$

Wet deposition was calculated as a function of rainfall intensity (mm h^{-1}) and acting on the full volume of air, regardless of the height of the cloud base (see laakso et al., 2003).

In the current simulations the height of the box model was set to a fixed value. The height was calculated from the meteorological parameter of the planetary boundary layer height (PBLH) and chosen as the 84th percentile of all values of the PBLH between 72 hours upwind and 0 hours upwind of Høvsøre. The height of the box model was generally between 500-1500 meters above sea level (m.a.s.l.).

6.6.2 Model input

The data input to the ADCHEM model is calculated in several steps. Meteorological data (GDAS 1º resolution) together with the HYSPLIT model was used to calculate the trajectory. Using a Fortran script, meteorology (e.g. wind velocity, surface pressure etc.) was added to the trajectory from the meteorological data. Once the trajectory and meteorology were calculated, the emission data, photosynthetic active radiation (PAR) and the spectral actinic flux are calculated in the model.

Spectral actinic flux is the measure of the radiative flux from all directions in a volume of air and is calculated along the trajectory using the radiative transfer model. A second output parameter from the radiative transfer model is PAR, which is later used in the calculation of terrestrial BVOC emissions.

Gas phase emissions used as input to the ADCHEM model were marine and terrestrial anthropogenic emissions of SO_2, NO_x, CO and non-methane VOCs (NMVOCs). Anthropogenic emissions were calculated using EMEP data and Biogenic emissions using a terrestrial BVOC

model and a marine isoprene emission model. The SO_2 emissions calculated from the EMEP data also include marine SO_2 derived from biogenic emissions of DMS. The land based BVOC emissions were based on land cover data including a vegetation speciation. In the model, the plants or trees (e.g. birch, pine etc.) are addressed with emission potentials for the different molecular species according to data from Smiatek and Steinbrecher (2006). The BVOC emissions were then calculated according to Guenther et al. (1991, 1993, 1997) as a function of PAR and temperature. The Marine isoprene model was developed for this project and is discussed further in chapter 6.6.3.

The speciation of all the NMVOCs used in the model is shown in appendix B. The NMVOC emissions from the EMEP data were speciated according to Simpson et al. (2012) with the exception of marine ship NMVOC emissions for which the work by Passant (2002) was employed.

Shipping emissions were assumed to have no special time variability. All other emissions calculated from the EMEP data except marine biogenic SO_2 were adjusted for country specific monthly, weekly and daily variations. Marine biogenic SO_2 which is the oxidation product of DMS emissions was adjusted for seasonal variations according to Tarrasón et al. (1995).

Primary particle emissions included in the simulations were marine sea spray and combustion generated particles from shipping (marine) and road traffic (terrestrial). The sea spray emissions were assumed to have a bimodal size distribution with modes at 0.1 µm and 2.5 µm, calculated from the parametrisation by Mårtensson et al. (2003). The parametrisation of the sea spray emissions is temperature, salinity and wind speed dependent. The wind speed dependence derives from its relationship to the white cap area fraction. Temperature has only a small influence on the resulting size distribution while variations in the salinity from 9.2‰ and 33.0‰ have a negligible effect on particles with diameters less than 70 nm, but significantly less large particles are formed from water with low salinity. The parametrisation for a salinity of 33‰ was used throughout the modelling and parametrisation of the temperature dependence was implemented for temperatures of 0ºC, 5ºC or 10ºC.

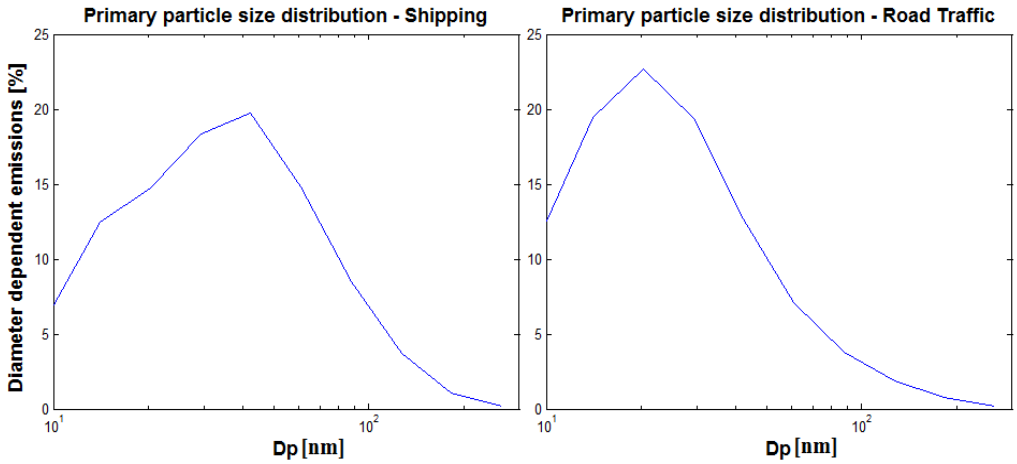

Figure 14: Modelled size distributions of primary particles emitted from shipping and road traffic.

The primary particle distribution from shipping was assumed to have a trimodal shape and was calculated from the combined particle size distributions of the results found by Jonsson et al. (2011) and Petzold et al. (2008). The number of particles emitted was scaled against NO_x emissions from the results by Petzold et al. (2008). Similarly, road traffic primary particle emissions and size distribution were calculated using the results of Kristensson et al. (2004). Figure 14 displays the particle size distributions from shipping emissions and road traffic emissions employed in the ADCHEM model.

6.6.3 Marine emissions of isoprene

A major BVOC emitted from the oceans is isoprene. In order to estimate the marine biogenic emissions of isoprene, a simple gas exchange model of isoprene sea-air fluxes was developed. The model is based on the chlorophyll-a concentration in the ocean surface water, wind velocity and the concentration of isoprene in the air.

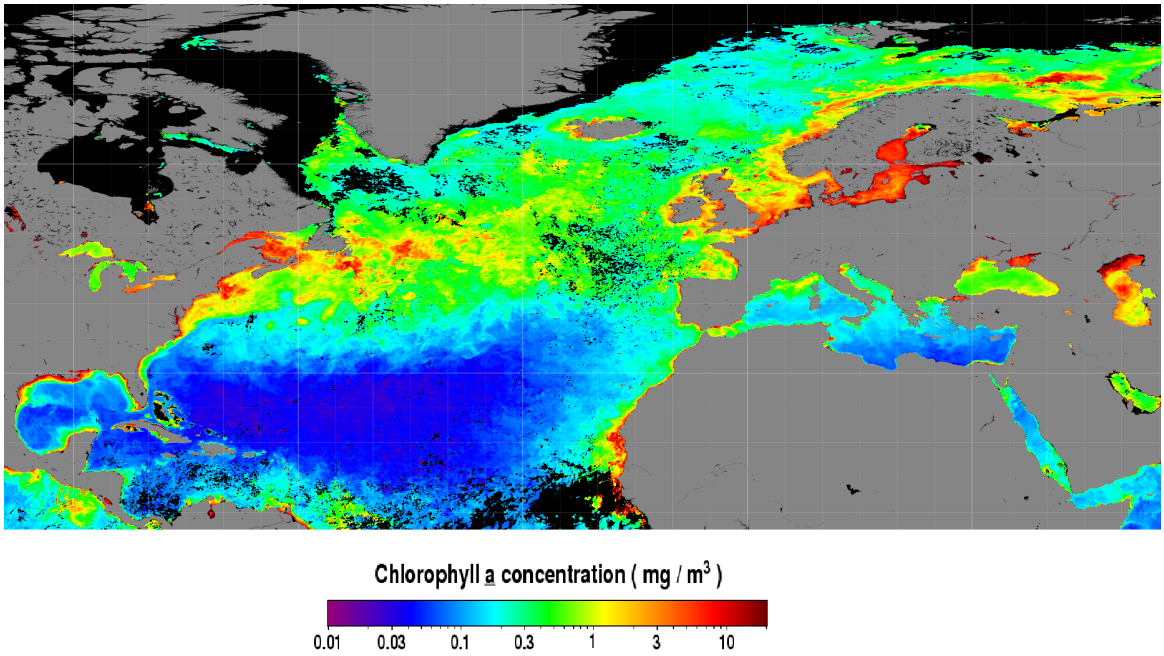

Figure 15: Monthly composite chlorophyll-a concentrations for April 2012 and for the area of interest. Source: Feldman, G. C., C. R. McClain, Ocean Color Web, MODIS-Aqua, Reprocessing 2005, NASA Goddard Space Flight Center. Eds. Kuring, N., Bailey, S. W. Access date: 2014-07-20. http://oceancolor.gsfc.nasa.gov

The model input chlorophyll-a concentrations were obtained from the Ocean Color web (NASA, MODIS-Aqua) where gridded near surface chlorophyll-a data with a resolution of 9x9 km have been derived from the MODIS-Aqua satellite instruments. Monthly composite data were used in order to minimize the number of missing grid cells. The chlorophyll-a concentration for April, 2012 is shown in figure 15 which shows significantly higher concentrations in the North Sea compared to the North East Atlantic Ocean.

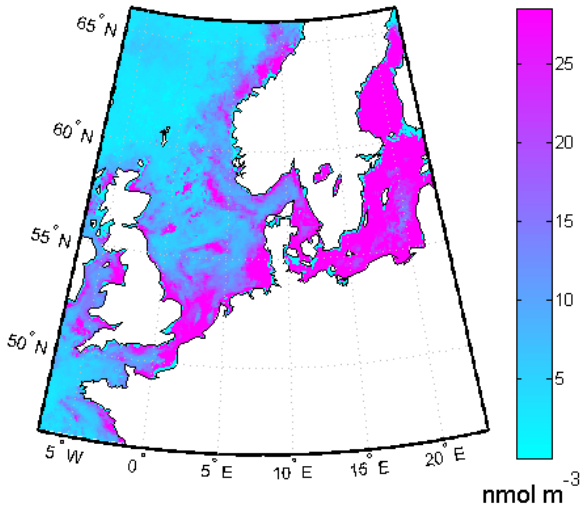

Figure 16: Derived isoprene concentrations in the North Sea and Baltic Sea during April 2012.

In the model, isoprene concentrations in the surface water are calculated using the linear relationship between the chlorophyll-a and the isoprene concentrations found by Broadgate et al. (1997), equation 6.6. A more realistic isoprene model would include PAR and sea temperatures. However, for the qualitative evaluation of the relative importance between particle precursor gases, the simpler approach was deemed sufficient. A zoom in on the North Sea displaying the derived isoprene concentrations is shown in figure 16.

$$[C_{\text{Isoprene}}]=6.43[C_{\text{Chl-a}}]+1.2 \qquad \text{EQ 6.6}$$

The isoprene flux model assumes a steady state condition where the production equals all losses. For simplicity it has been assumed that a no-slip condition on the surface leads to an existing layer of air closest to the ground with zero wind velocity. This layer, the roughness layer (z_o), is assumed at all times to be in equilibrium with the isoprene concentration of the water according to Henry's law. Above the roughness layer is due to frictional forces a quasi-laminar layer. As the name implies, the flow of the sub layer is laminar and hence, no vertical or lateral mixing occurs. The flux across the thin layer is thus purely based on molecular diffusion and the concentration gradient across the quasi laminar layer, equation 6.7 (Seinfeld and pandis, 2006). The flux of isoprene ($F_{isoprene}$) across the quasi-laminar sub layer is determined by the quasi-laminar layer resistance (r_b), equation 6.8 (Simpson et al., 2012). In equation 6.7 and 6.8 respectively, u_* is the wind shear, C_{air} and $C_{roughness\ layer}$ are the isoprene concentrations in the air and the roughness layer respectively, k is the von Karman constant and $D_{isoprene}$ is the molecular diffusivity of isoprene in air.

$$F_{Isoprene}=r_b u_*([C_{air}]-[C_{roughness\,layer}]) \quad [\text{mol m}^{-2}\text{s}^{-1}] \qquad \text{EQ 6.7}$$

$$r_b=\frac{1}{ku_*}\ln\left(\frac{z_o}{D_{isoprene}}ku_*\right) \quad [\text{m}^{-1}\text{s}] \qquad \text{EQ 6.8}$$

The model depends on the wind speed, which appears in the calculation of the wind shear, the roughness layer calculation and the wind drag coefficient, described by equation 6.9, equation 6.10 (Seinfeld and pandis, 2006) and equation 6.11 (Yelland and Taylor, 1996) respectively. In equation 6.9-6.11, z_{10m} equals 10 meters above the ocean surface, u_{10m} is the wind speed at 10 meters above the ocean surface, τ is the wind stress, ρ_{air} the density of air and C_D is the wind drag coefficient .

$$z_0=z_{10m}\exp\left(-u_{10m}\frac{k}{u_*}\right) \quad [\text{m}] \qquad \text{EQ 6.9}$$

$$u_*=\left(\frac{\tau}{\rho_{air}}\right)^{-(1/2)}=\left(C_D u_{10m}^2\right)^{-(1/2)} \quad [\text{m s}^{-1}] \qquad \text{EQ 6.10}$$

$$C_D=10^{-3}\left(0.29+\frac{3.1}{u_{10m}}+\frac{7.7}{u_{10m}^2}\right) \quad 3\text{ms}^{-1}<u_{10m}<6\text{ms}^{-1}$$

$$C_D=10^{-3}\left(0.60+0.070\,u_{10m}\right) \quad 6\text{ms}^{-1}<u_{10m}<23\text{ms}^{-1} \qquad \text{EQ 6.11}$$

Isoprene fluxes and concentrations are displayed in figure 17 for the ADCHEM model simulation arriving at Høvsøre at noon the 15th April, 2012. The isoprene flux ranges between 0.2 nmol m^{-2} day^{-1} and 180 nmol m^{-2} day^{-1}. Measured fluxes in the North Sea suggest a mean annual flux of $1.7x10^7$ molecules cm^{-2} s^{-1} equivalent to 24.4 nmol m^{-2} day^{-1} (Broadgate et al., 1997). The maximum and minimum fluxes reported were 67 nmol m^{-2} day^{-1} and 1.4 nmol m^{-2} day^{-1} respectively. The modelled fluxes are therefore moderately higher than expected from these observations in the North Sea. However, Matsunaga et al. (2002) measured isoprene fluxes in the western North Pacific as high as 300 nmol m^{-2} day^{-1} and also presents observations from the Florida straits with fluxes above 100 nmol m^{-2} day^{-1}. These observations put the modelled fluxes of isoprene well within observed values, albeit the observations took place far from the current region in which the conditions were simulated. Matsunaga et al. (2002) also presents observations of the measured concentration of

isoprene in the air. The observed median concentration in the western North Pacific during a day in May was 43 pptv. In the current simulation, the isoprene concentration in the air is below 50 pptv while the airmass remains over the ocean. The rapid increase in isoprene concentration after Høvsøre (>96 h) is due to large terrestrial emissions.

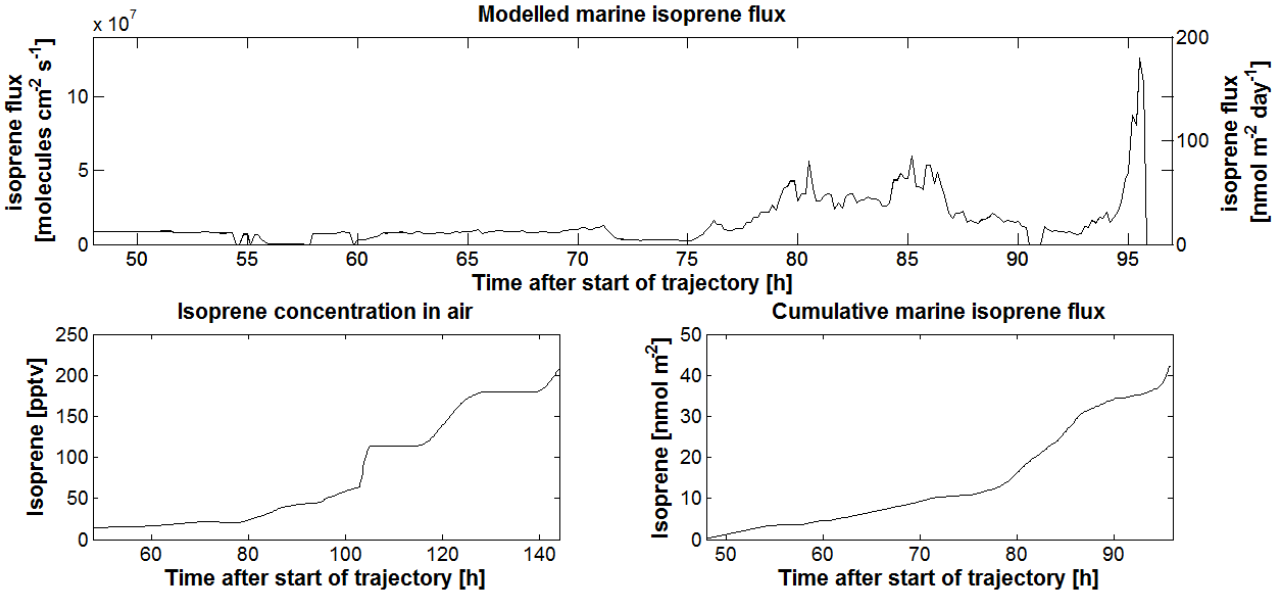

Figure 17: Modelled marine isoprene flux, total isoprene concentration in the air of the box model and the cumulated marine isoprene flux. The trajectory arrives at Høvsøre after 96 hours at noon the 15th April, 2012.

7 Station description

The aerosol data in this project were gathered at three different coastal measurement sites, Finokalia in Greece, Høvsøre in Denmark and Preila in Lithuania (figure 18). The instrumentation, time period, number of analysed days and the location of the measurement sites are listed in table 5.

By sorting the measured aerosol number size distributions according to their concentration in each size bin, site specific characteristic aerosol number size distributions were calculated for all sites using the available data. Also, wind statistics and a backward trajectory analysis for each measurement site are included below. The wind direction was calculated using the backward trajectories by calculating the bearing between the location of the station and the location of the air parcel one hour upwind of the station.

Table 5: Measurement station description. Data period, number of days analysed, coordinate and instrumentation.

Station	Country	Data period	# Days	Coordinates	Instrument	Reference
Finokalia	Greece	From: 2008-04-04 Until: 2009-06-15	306	35º20' N 25º40' E	AIS (0.8-42 nm) SMPS (8-895 nm)	Asmi et al., 2011
Høvsøre	Denmark	From: 2012-03-09 Until: 2009-05-31	85	56º27' N 8º09' E	AIS (0.8-42 nm) SMPS (12-496 nm)	Kivekäs et al., 2014
Preila	Lithuania	From: 2009-04-01 Until: 2013-05-30	735	55º55' N 21º00' E	SMPS (8-840 nm)	Asmi et al., 2011

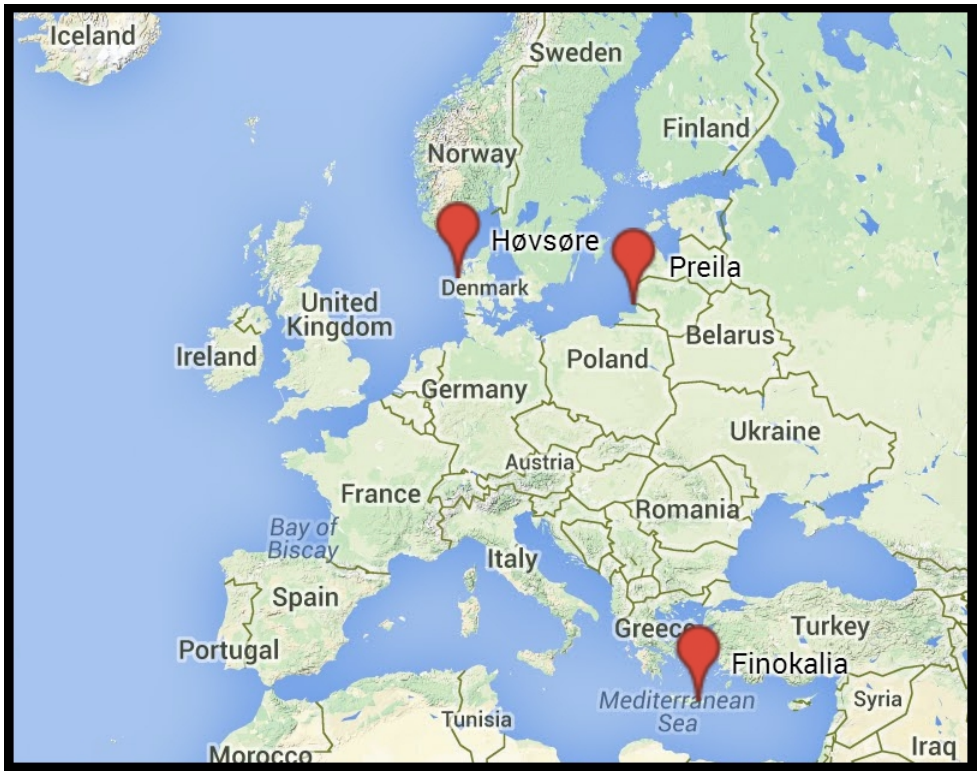

Figure 18: Location of the background measurement stations.

7.1 Finokalia

Finokalia measurement station is a background measurement station situated on the north east coast of the Greek island of Crete (35º20' N 25º40' E). The station is remotely located on the top of a hill (250 m.a.s.l) near the sea. Aerosols at the Finokalia station generally contain aged particles from

various sources and regions including Greece, Turkey and northern Africa (Pikridas et al., 2012). A trajectory analysis of all trajectories arriving at the Finokalia station between 5th June 2008 and 15th June 2009, shown in figure 21, confirms these aerosol source regions. The size distribution at Finokalia over the full period, corresponding to approximately one year of data, shows two distinct modes for the median and 15th percentile distributions (figure 19). The modes correspond to an Aitken mode at 60 nm and an accumulation mode at 100-150 nm. Seasonal variations in the size distributions are small with the exception of summer (JJA) where only one strong mode is visible with a mean mobility diameter of approximately 100 nm. During winter (DJF) there is also a significant decrease of particles over all sizes.

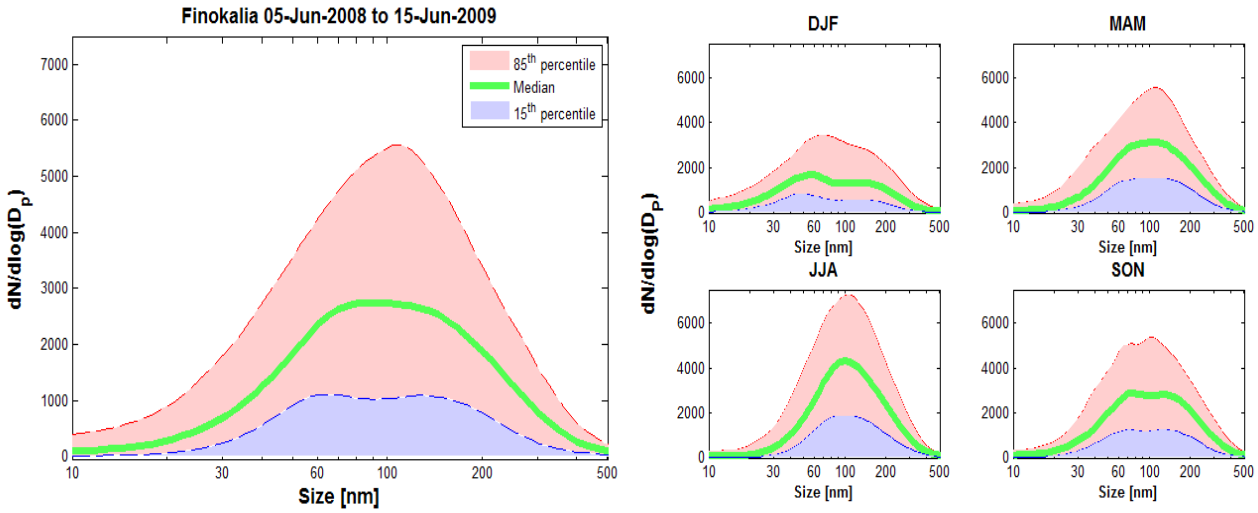

Figure 19: Finokalia size distributions. Left figure displays 15th, median and 85th percentile distributions of the period over a full day. Right figures shows seasonal variations in size distribution, i.e. winter (DJF), spring (MAM), summer (JJA) and autumn (SON).

The predominant wind direction at Finokalia station is west to north west (figure 20, left). Comparing the wind direction and the wind speed of the full period to periods with NPF (figure 20, right) does not reveal any significant relationship between wind conditions and the number of NPF events but rather resembles the overall wind direction at Finokalia.

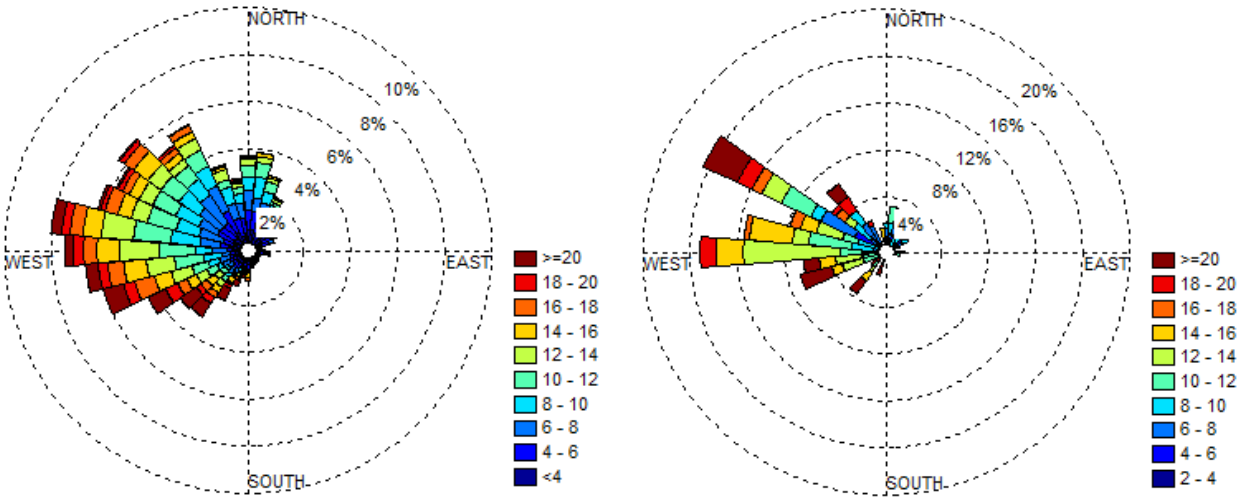

Figure 20:Finokalia wind statistics, colours show wind speed (m/s) and circles percent of days. Left figure displays wind speed and wind direction at the station for all trajectories during the period. Right figure shows wind statistics for periods with NPF at the station.

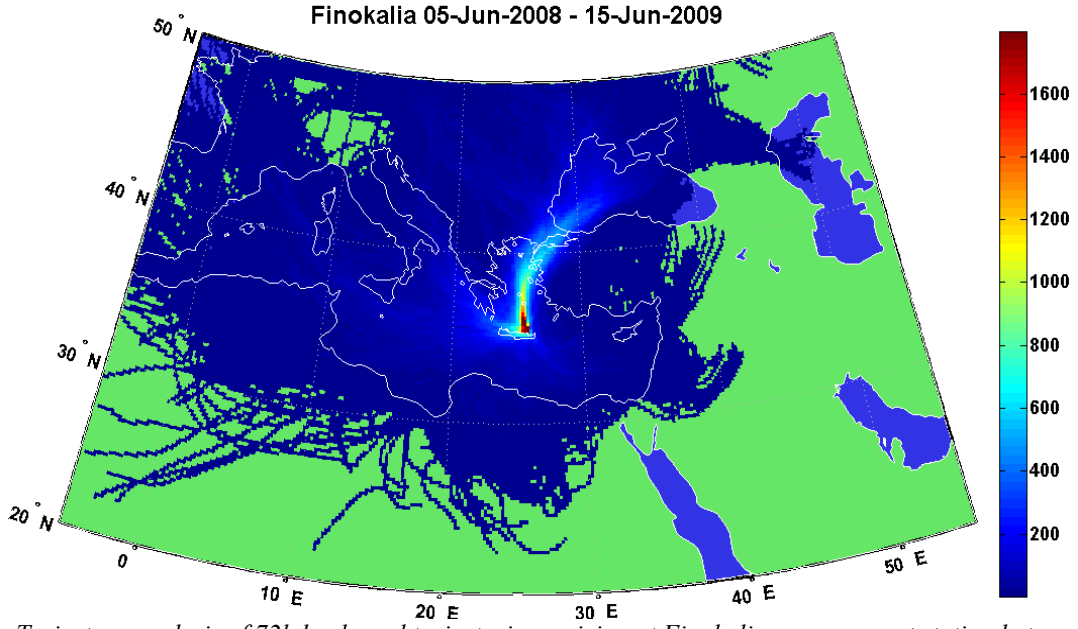

Figure 21: Trajectory analysis of 72h backward trajectories arriving at Finokalia measurement station between 5th June 2008 and 15th June 2009, 1h interval. The scale of the colorbar shows the number of trajectories which have passed through a grid cell.

7.2 Høvsøre

Høvsøre background measurement station (56º27' N 8º09' E) is located on the north west coast of the Danish mainland, Jutland. It is situated 1.8 km from the coast line and approximately 50 km from major shipping lanes in the North Sea. A site and instrument description has previously been presented in Kivekäs et al. (2014.) The data from Høvsøre were gathered with an Air Ion Spectrometer (AIS) and an SMPS. The SMPS had a lower cut off size of 12 nm. With a lower cut off size of 12nm it might become difficult to determine whether the NPF is occurring at the station or upwind only. The AIS allows the detection of particle diameters down to approximately 1 nm, hence combining the SMPS with an AIS, nucleation events occurring at the station may easily be discerned from those events occurring slightly upwind of Høvsøre but not at the station. The size distribution at Høvsøre has a dominant Aitken mode and a weak accumulation mode. The short period over which the data was collected does not allow a seasonal analysis of the number size distribution. However, hourly variations during the day were analysed. From figure 22 however, it

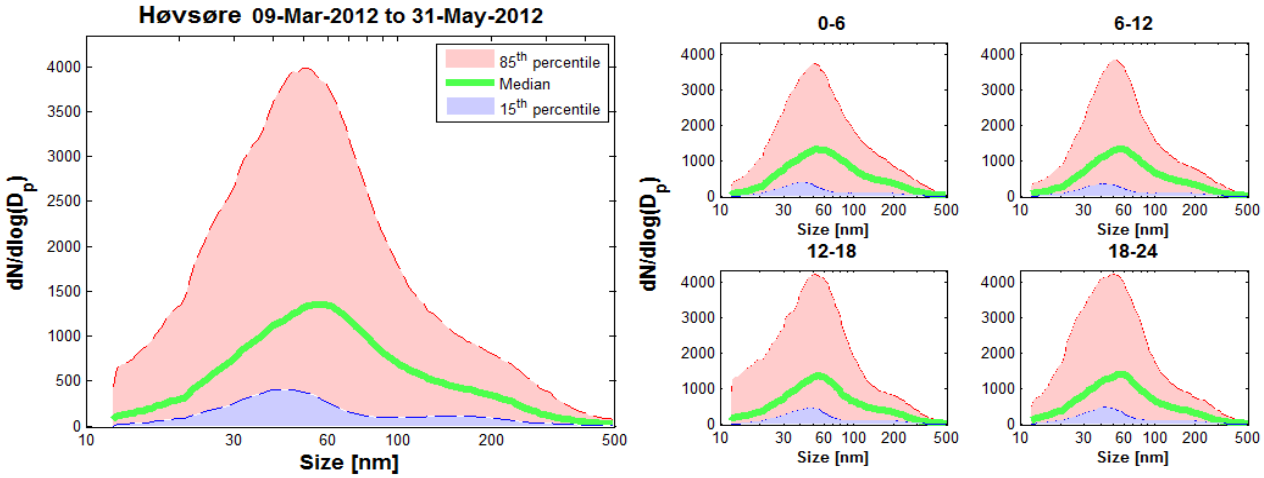

Figure 22: Høvsøre size distributions from SMPS data. Left figure displays 15th, median and 85th percentile distributions of the period over a full day. Right figures shows variations in size distribution during the day, i.e. at 00-06 hours (night), 06-12 hours (morning), 12-18 hours (afternoon), 18-24 hours (evening).

is clear that hourly variations have little or no impact on the particle size distribution at Høvsøre.

The trajectory analysis in figure 24 shows that a majority of all air masses arriving at Høvsøre originates from the North Atlantic. Closer to Høvsøre there is a clear distinction between trajectories with a north westerly path and a south westerly path. In general, North westerly paths correspond to an Arctic airmass origin while the south westerly paths to more sub tropic regions of the North Atlantic. The Arctic air masses are very clean with few pollution sources.

The calculated wind data for Høvsøre (figure 23) shows indeed, similar to the trajectory analysis, that the north westerly winds are most common. Due to the short time period of the data it is not possible to make concluding remarks by comparing the wind statistics during event and non event. However, it is worth noticing the relatively low frequency of nucleation during south westerly winds.

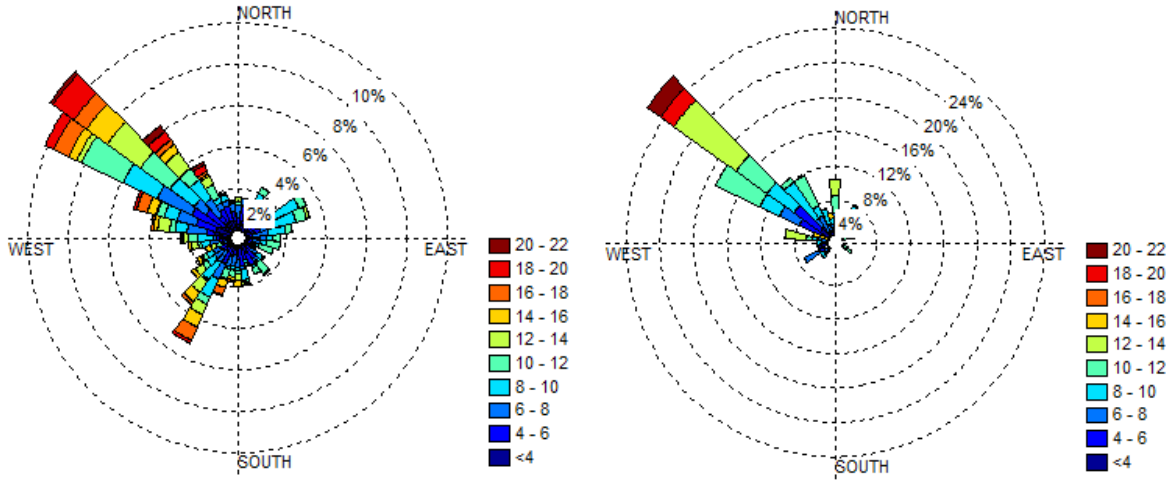

Figure 23: Høvsøre wind statistics, colours show wind speed (m/s) and circles percent of days. Left figure displays wind speed and wind direction at the station for all trajectories during the period. Right figure shows wind statistics for periods with NPF at the station.

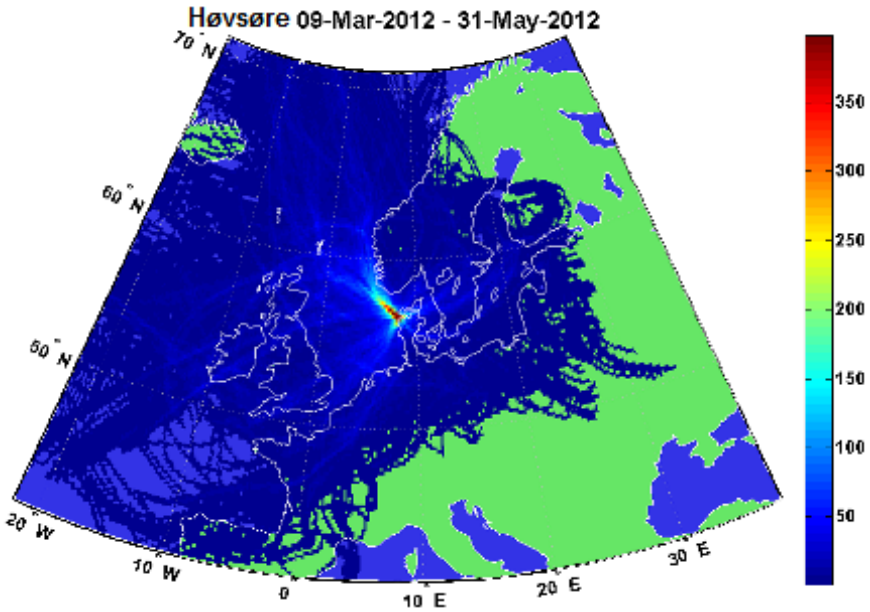

Figure 24:Trajectory analysis of 72h backward trajectories arriving at Høvsøre measurement station between 10th Mars 2012 and 31th May 2012, 1 hour interval. The scale on the colorbar shows the number of trajectories which has passed through a grid cell.

7.3 Preila

Preila field station is a background measurement station located in Lithuania on the Curonian Spit, just in front of the Baltic Sea. The particle size distribution was measured with an SMPS with a lower cut off size of 8 nm. The size distribution at Preila (figure 25) measured in mobility diameter has a clear Aitken mode at 60 nm and an accumulation mode at 150 nm. The seasonal trends in the particle size distribution are relatively small. However during the summer months (JJA), the upper concentration of particles with diameters below 15 nm is very large. This is probably due the low availability of data coupled with an event frequency of approximately 30% (see figure 29) for these months. The dominant wind direction at Preila is south west to north west indicating that predominantly, the wind arrives from the Baltic Sea (figure 26).

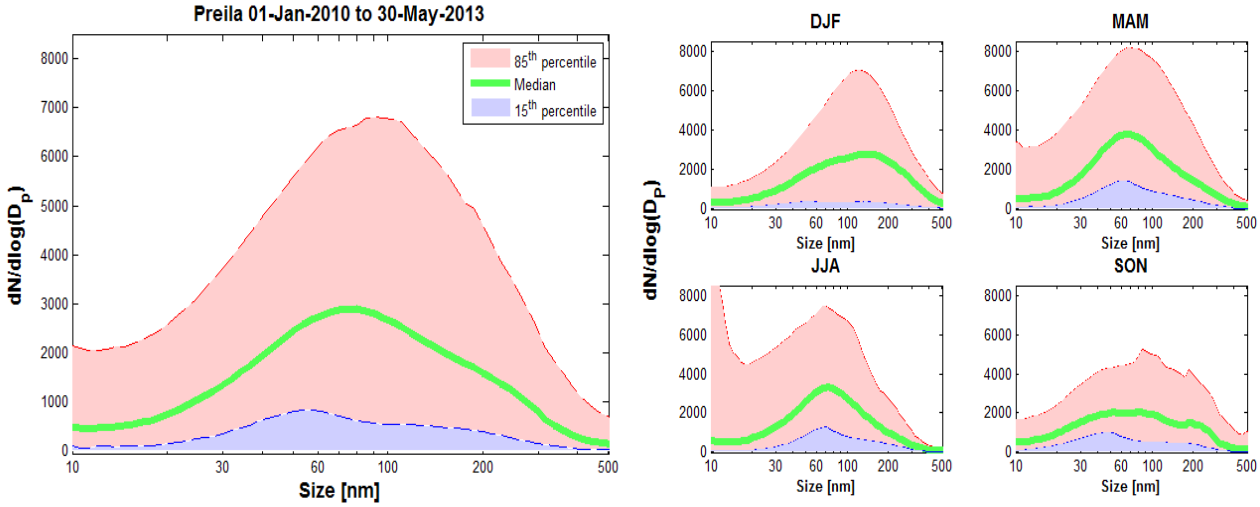

Figure 25: Preila size distributions. Left figure displays 15th, median and 85th percentile distributions of the period over a full day. Right figures shows seasonal variations in size distribution, i.e. winter, spring, summer and autumn.

The trajectory analysis (figure 27) of 72h backward trajectories for the full measurement period shows, compared to both Høvsøre and Finokalia, air mass sources much more homogeneously spread out over Europe. However, the fraction of trajectories which has passed the Baltic Sea before reaching Preila is significantly larger than any other geographical location. This suggests that when the wind is westerly at the Preila station, the air also traverse a large part of the southern Baltic Sea.

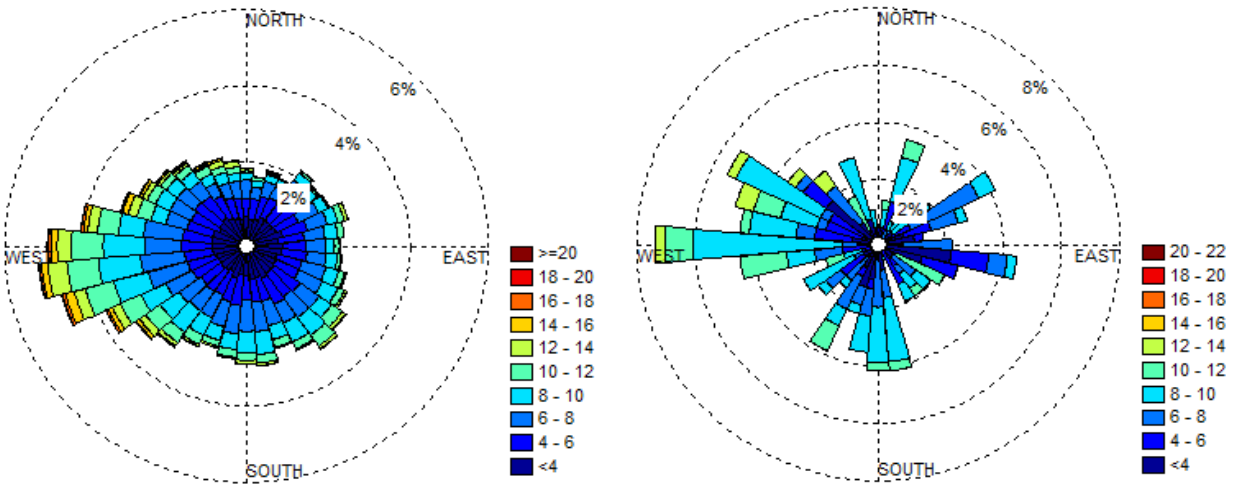

Figure 26: Preila wind statistics, colours show wind speed (m/s) and circles percent of days. Left figure displays wind speed and wind direction at the station for all trajectories during the period. Right figure shows wind statistics for periods with NPF at the station.

This most likely influence air mass properties and ship particle emissions may be large contributors to the Preila background particle concentration.

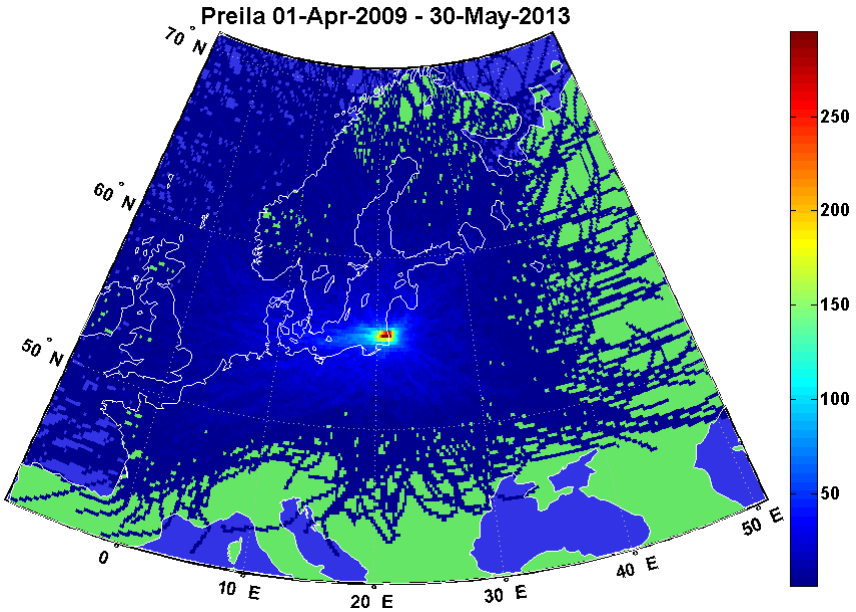

Figure 27: Trajectory analysis of 72h backward trajectories arriving at Preila background station between 1th April 2009 and 30th May 2013, 1 hour interval. The scale on the colorbar shows the number of trajectories which has passed through a grid cell.

8 Results

8.1 Results - Task 1

Chapter 8.1 includes the results of the NanoMap analysis. The event statistics (chapter 8.1.1) includes a discussion. The NanoMap results of chapter 8.1.2 which were aimed to address the first aim of this project are discussed in chapter 9.1.

8.1.1 Event statistics – results and discussion

The NPF event statistics for the three measurement stations is an important tool for a comparison of NPF between different measurement stations. The event statistics contains a frequency analysis, a formation time analysis and an analysis of the time between the formation start time and the EOG time. The frequency analysis is given both for the total period and month specific. For later use with NanoMap, the formation time analysis is very informative and is used when calculating the probability maps.

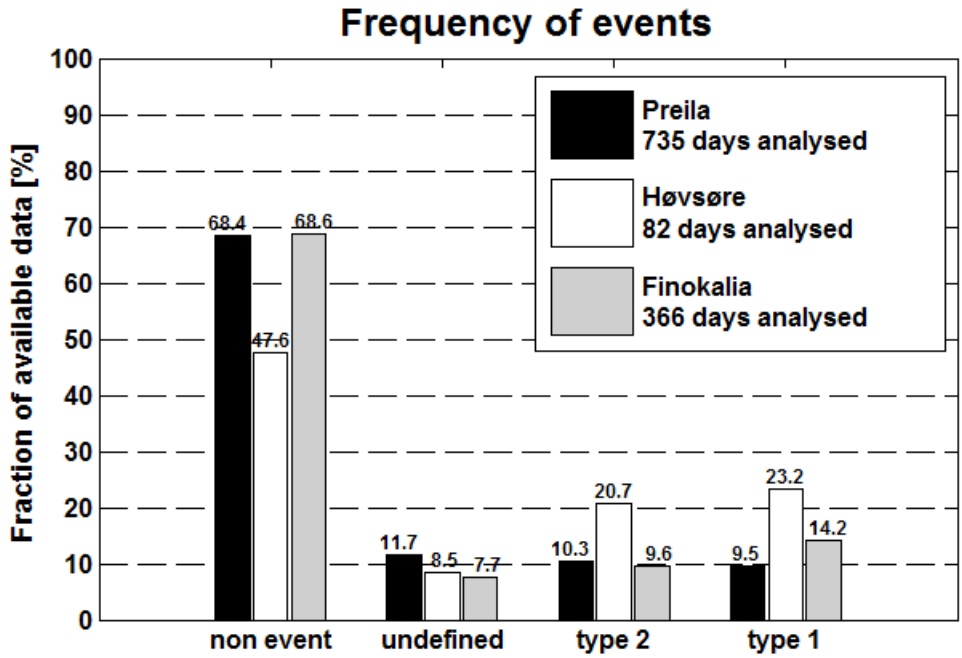

Figure 28: Overview of the event frequency for the three measurement stations.

With the exception of Preila, the NPF frequency at the measurement sites (figure 28) are within the range (21% - 57%) reported by Manninen et al. (2010) where statistics of NPF were evaluated for 12 European measurement stations.

The frequency of events (including both class I and II) for Preila and Finokalia are 19.8% and 23.8% respectively. These findings are thus in the lower end compared to several other sites. A possible explanation may be their coastal locations which in the absence of large biogenic emissions of precursor gases from forest emissions are likely to exhibit less NPF. If instead the monthly number and frequency of events are analysed (figure 29), it is clear that NPF varies significantly during the year. The event frequency in Preila peaks in the spring and in September while it exhibits a minimum from June to August and almost no events during the winter months. In Finokalia the event frequency is similar to that of Preila in early spring but higher during late autumn and December. The results suggest that the presence of solar radiation and therefore larger biogenic emissions may be an important factor determining the number of NPF events. Due to its more

southern location, this may explain the higher frequency of NPF events during the winter months in Finokalia.

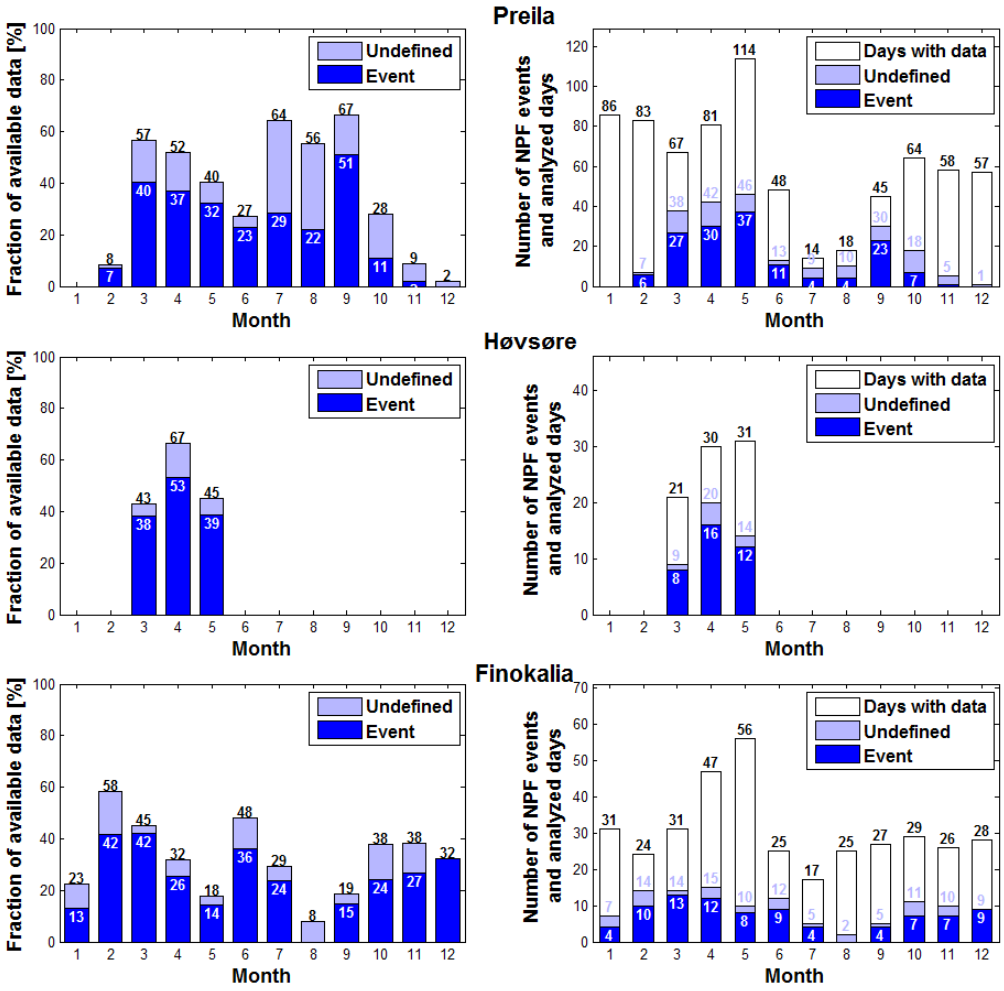

Figure 29: Monthly event statistics. Left figures display the fraction of event days and event plus undefined days with respect to the number of days with available data. Right figures display the total number of event days, undefined days and the total number of days with data. Event days include both class I and class II events.

Only three month of data from Høvsøre were available. During this period a total number of 36 days were classified as a class I event day (23.2 %). In relation to both Preila and Finokalia this is an exceptionally large number of NPF events. However in comparison to the fraction of events observed at a non-coastal measurement station, e.g. Vavihill (Sweden) during Mars to April which has an event frequency between 50% and 65% (Kristensson et al., 2008), the frequency of events in Høvsøre is still lower. For a comparison to Høvsøre, the number of NPF events in Vavihill were in this project calculated for the same measurement period as the Høvsøre data. The event frequency in Vavihill for this period ranged between 48% in March and 64% in May.

The formation time analysis of the observed NPF at the station is one of the steps in the NanoMap analysis. Figure 30 shows a summary of the start time and end time of all NPF events for all three stations. In the NanoMap method, the formation analysis is initially a necessity to evaluate how many hours of the trajectories should be plotted during an event. There exists at least one more strong reason to perform an accurate formation time analysis. Given enough data and a long enough time series, the formation time analysis provides a direct answer to during what time of the day NPF events may occur. This information, while trivial, may be used in order to greatly enhance the probability calculations of the NanoMap results. This is done by excluding all trajectories arriving at the station during hours which are outside the formation time. This will also provide climate

modelers with more accurate results, with regard to both time and probability of NPF. Important information regarding the mechanisms behind the nucleation may also be derived from the analysis of the formation time.

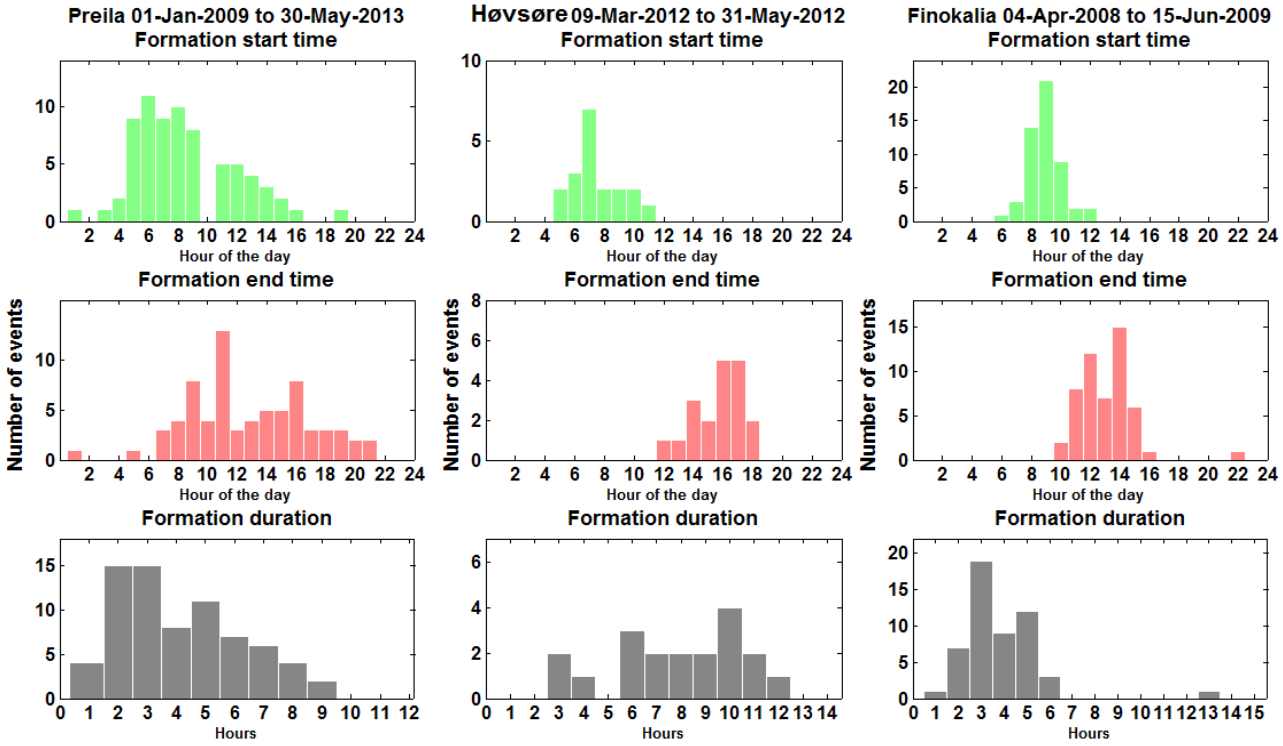

Figure 30: Analysis of the start and end time of the observed NPF at the three stations. The y-axis shows number of events and are the same for all figures. All times shown are in local time. Top: Start of formation. Middle: End of formation. Bottom: Duration of formation.

The formation starting time is in all cases before noon local time in both Finokalia and Høvsøre and is often observed already in the early morning hours for Preila. In Preila, the start of formation is not necessarily after sunrise but still, the majority of the observed events start after the onset of solar radiation. Similarly, the formation end time occurs in most cases in the afternoon but not after sunset. In Preila, formation starting times are found also in the afternoon and evening, but the majority of all events start already in the early morning. This information together with the apparent absence of night-time formation is a strong indicator that atmospheric photochemistry is indeed a necessity in order to observe NPF. The duration of the formation time is similar for all three stations and in general ranges from a couple of hours to half a day.

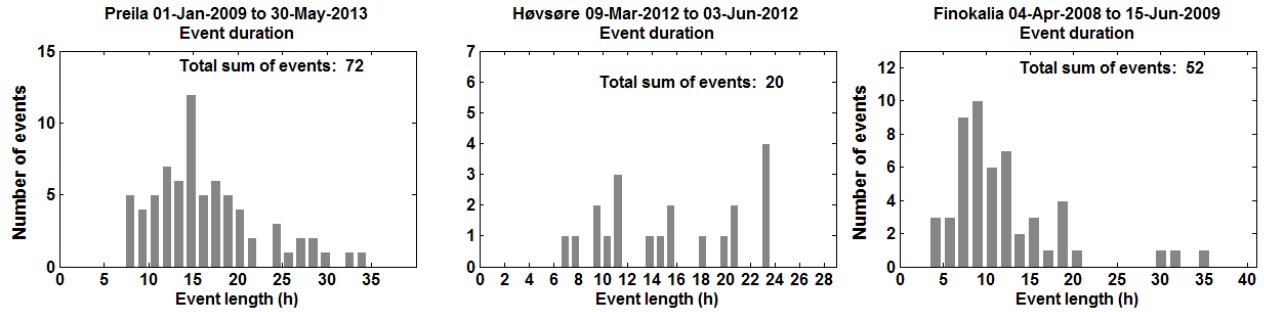

Figure 31: Time between the start time and EOG time. The figure shows the total event length measured from the start time of formation until the observed end of growth.

Another parameter which has been discussed (chapter 6.5.2) to vary for several reasons and to greatly influence the NanoMap results is the time between the formation start time and the EOG

time. The time between the start time and EOG time (figure 31) is often less than 20 hours. Therefore, if the mean wind speed is between 5-10 ms^{-1}, it may be reasoned that the maximum extent of the inferred NPF in the NanoMap analysis rarely exceeds 500 km. This implies that the inferred NPF is often within a distance from the station where the trajectory uncertainty does not contribute considerably to the total uncertainty of the NanoMap results, as discussed in chapter 6.5.4.

8.1.2 NanoMap - results

For each of the three measurement sites, the NanoMap results presented are the Number maps of the total number of inferred events and the event probability. In all results, the resolution used in the calculations were 0.2º. The results show that the areas with the highest number of events are not in all cases the areas with highest event probability.

Finokalia

The inferred NPF from the NanoMap analysis of the Finokalia data, shown in figure 32, demonstrates frequent NPF over the Aegean Sea due north of Finokalia station. Secondly, west and south of Finokalia are larger areas exhibiting a high frequency of NPF events. These areas have an inferred number of events between 6-10 for the duration of the measurement period. Other areas show fewer events. In sharp contrast to the total number of events, the probability of events west of Finokalia is less than one percent. The Aegean Sea and the sea area south of Finokalia have event probabilities close to 15%. The highest probability is found over eastern Turkey, however this area is much further away than 500 km from the Finokalia station which represents the area of highest accuracy. Most sea areas where one or more events were inferred (figure 32), have event probabilities between 3% to 10% which is comparably small to the class I frequency at Finokalia station of 14.2%. Although the inferred event probability is small over sea areas, in total there are fewer inferred events over land areas and subsequently the calculated event probability is even less over land areas than over sea areas.

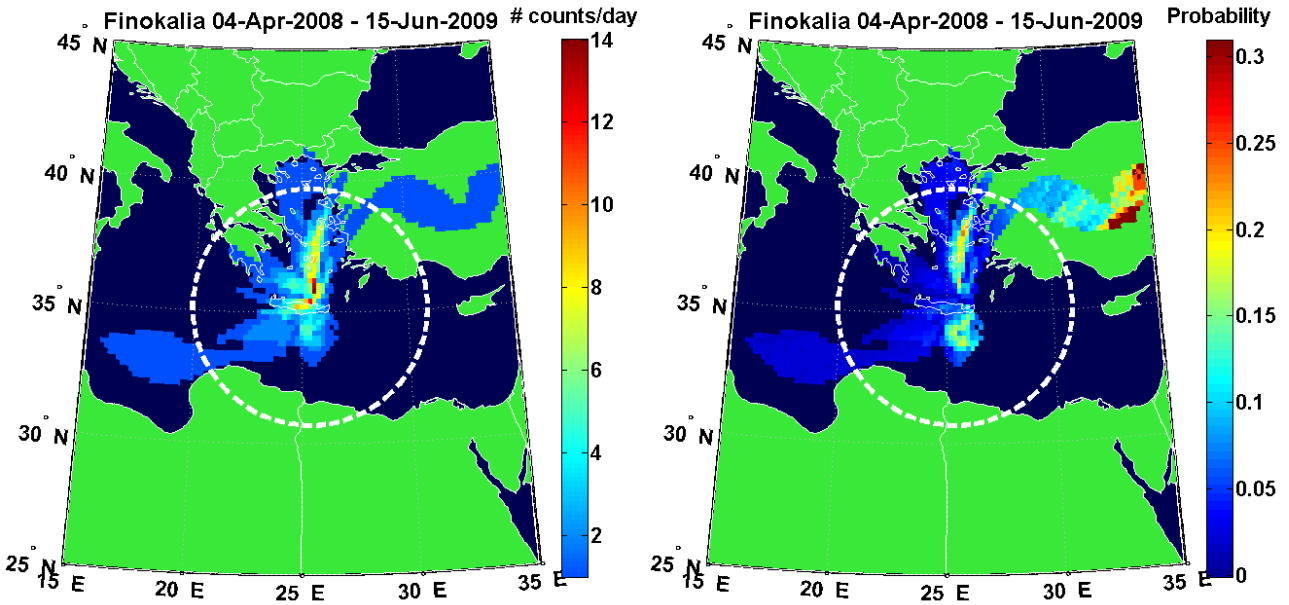

Figure 32: NanoMap results for data from Finokalia displaying regional NPF for measurement conducted between 4th April 2008 and 15h of June 2009 and a total of 366 analysed days. Left figure: total number of inferred event days in each grid cell. Right figure: probability of NPF in each grid cell and per day. The white circle represents a distance of 500 km from Finokalia.

Høvsøre

The NanoMap analysis from Høvsøre data shown in figure 33 shows the occurrence of a large number of NPF events during a relatively short time period over the North Sea. The maximum total number of events are inferred north-west of Høvsøre, in figure 33 (left), and corresponds to eight days with NPF. The area of the most frequently inferred NPF is over the North Sea, but also to a smaller extent covers the south-west coast of Norway. Areas with less counts per day are found both to the west, south and to the north-east of Høvsøre.

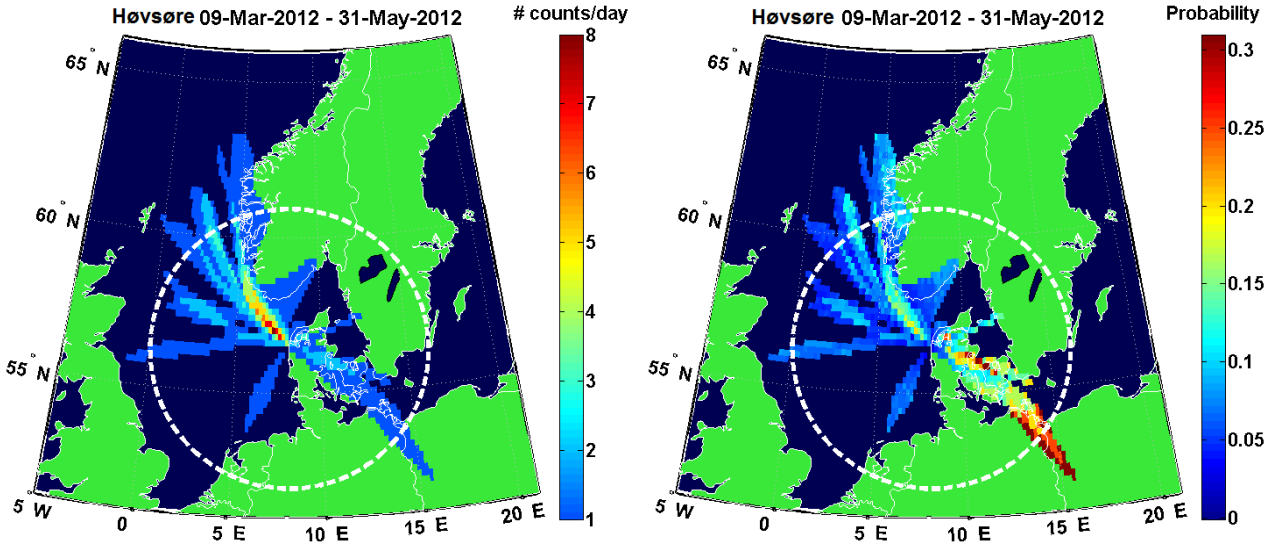

Figure 33: NanoMap results for data from Høvsøre displaying regional NPF for measurement conducted between 9th March 2012 and 31h of May 2012 and a total of 82 analysed days. Left figure: total number of inferred event days in each grid cell. Right figure: probability of NPF in each grid cell and per day. The white circle represents a distance of 500 km from Høvsøre.

The event probability is high over the North Sea and the west coast of Norway with a daily probability of NPF ranging from 5% to 20%. This is lower compared to the class I event frequency at Høvsøre station (23.2%). South-east of Høvsøre is an area indicating very high event probability of 15% to 30%. This area stretches from Jutland in Denmark to Northern Germany and Poland and indicates a higher chance of NPF over land than ocean. It should be noted that relatively few trajectories were passing over these grid cells during the measurement period (figure 24).

Preila

At the Preila measurement station, 72 days were classified as class I events from a total of 735 analysed days. The NanoMap results are shown in figure 34.

Most of the events plotted in the NanoMap analysis occur within 500 km from Preila, which is represented by the white circle in figure 34. The maximum number of events recorded in a single grid cell is 11 event days. This maximum is found together with the majority of the events west of Preila station over the Baltic Sea. Near the station there are several event days in all directions; however the number of events is significantly higher for the grid cells south of Preila than for grid cells north of Preila. At distances further away than 500 km there are more events west than east of Preila. It is worth noticing the almost complete absence of events in the East and North Gotland Basin of the Baltic Sea. The probability of an event ranges from less than one to several percent. The highest probabilities are found west-north-west (WNW), to the south and due east of Preila. These highest probabilities have an event probability around 5%.

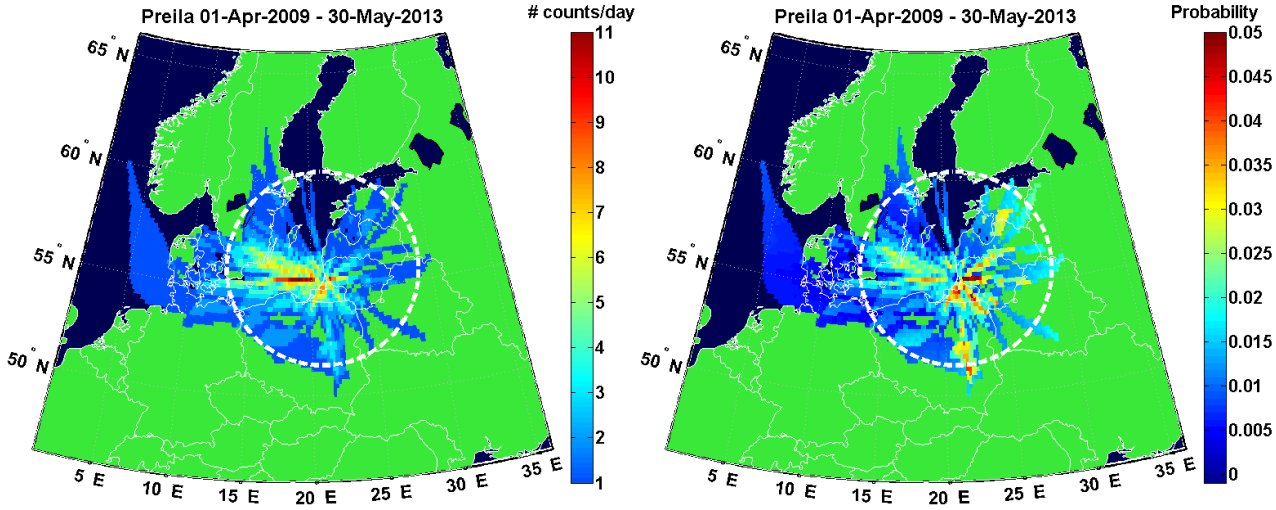

Figure 34: NanoMap results for data from Preila displaying regional NPF for measurement conducted between 1th April 2009 and 30th of May 2013 and a total of 735 analysed days. Left figure: total number of inferred event days in each grid cell. Right figure: probability of NPF in each grid cell and per day. The white circle represents a distance of 500 km from Preila.

8.2 Results – Task 2

In chapter 8.2, the results of the ADCHEM simulations are presented. These results include:

1. A comparison of the modelled data to the observed data from Høvsøre (chapter 8.2.1) including a discussion of the model accuracy.
2. The particle number size distribution at Høvsøre derived from the two model scenarios (chapter 8.2.2).
3. The geographical position of the modelled NPF, 0–24 hours upwind of Høvsøre (chapter 8.2.3).

Chapter 8.2.2 and 8.2.3 presents the simulation results aimed to assess the second aim of this project. The discussion of these results are given in chapter 9.2. The full simulations are available in appendix C. All times are in UTC time if not stated otherwise.

8.2.1 Model evaluation – results and discussion

A direct quantitative comparison of the modelled and the observed particle size distributions is not possible without first recalculating the size distributions to be based on the same geometric mean diameters and bin widths. This was deemed too time consuming and only compared qualitatively. Instead, the quantitative evaluation was based on the total particle number and the total particle volume of the modelled and measured data.

An overview of the observed particle size distribution at Høvsøre for the period between the 15th April 00:00 to the 16th April 24:00 (UTC+1) is shown in figure 38, bottom (chapter 8.2.2). It is possible to visually compare the measured particle number size distribution with the modelled size distribution in figure 38 (top and middle) without any further adjustments.

The measured size distributions display two clear NPF events on the 15th and 16th of April. The two events are similar, with a formation start time at approximately 9 am and formation end time in the early evening. The growth of the new particle modes is visible for the full measurement period starting from the formation start time. The new modes grow within hours to particle sizes between 10-20 nm in diameter. Visible background sources are ship plumes, characterised by sharp peaks between 30-100 nm, and a low concentration of marine background particles. The first hours of the measurement period are characterised by a comparatively strong Aitken mode.

The modelled particle size distribution is illustrated by the top and middle graphs in figure 38. Both scenarios show NPF with a formation start time around noon and formation end time between 6-9 pm. There is a low concentration of marine particles in both model scenarios while, naturally, scenario 1 is the only simulation able to capture ship emissions. To some extent, the modelled scenario 1 is able to simulate the strong Aitken mode evident in the observed size distribution (figure 38, bottom) between 00-04 am. the 15th April. Since the mode is not evident in scenario 2, the source is anthropogenic ship emissions of particulate matter.

The quantitative evaluation of the model to the observations is based on the total number concentration and the total particle volume. The modelled and the observed total particle number and total particle volume were plotted and a scatter plot of the modelled and observed total particle volume is included in the discussion below.

The total number concentration at Høvsøre is shown in figure 35. The modelled scenarios differ considerably from the observed and a strong model to observation correlation is not apparent.

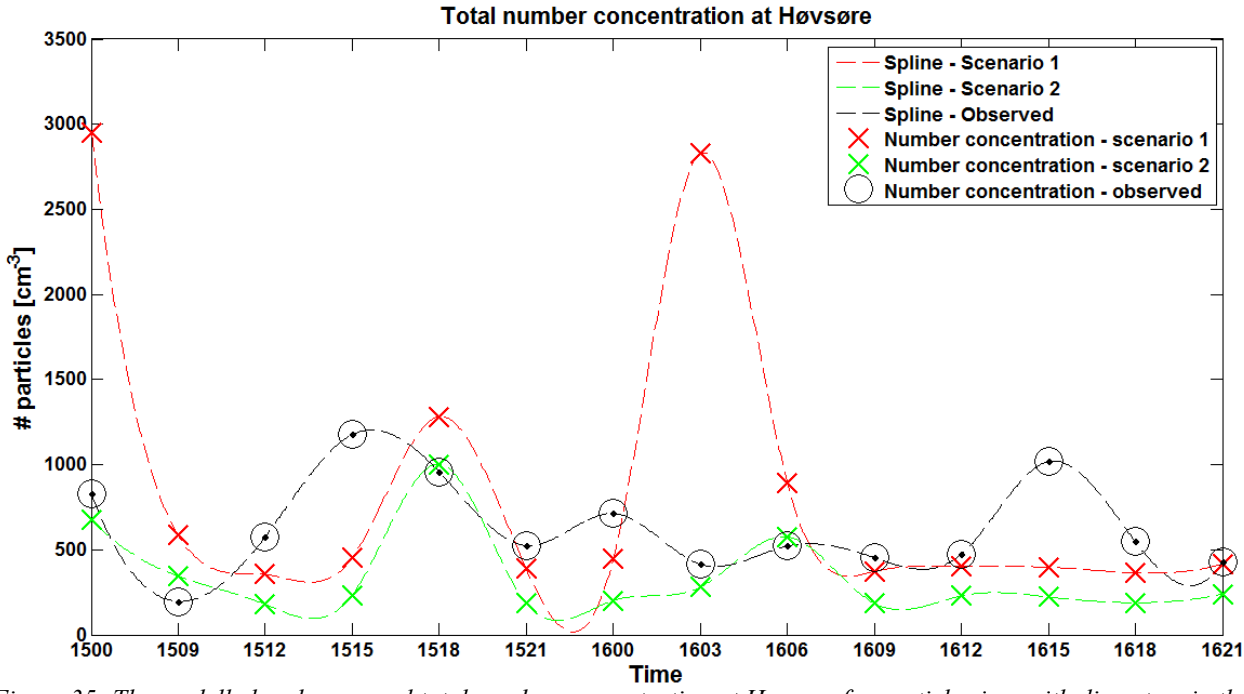

Figure 35: The modelled and measured total number concentration at Høvsøre for particle sizes with diameters in the size range 12–500 nm. Time in days and hours of the format "ddHH".

However, the total particle number is a difficult parameter to model during NPF, since the nucleation parameters are highly uncertain. The cut-off size of the SMPS instrument at Høvsøre also limits the comparison to particle diameters larger than 12 nm, at particle diameters above most of the observed and modelled particles deriving from NPF.

The total particle volume assumes that particles are spherical. The modelled and the measured total particle volumes are shown in figure 36. Figure 37 shows the model versus observation scatter plot for the total particle volume. In figure 37, values outside the area enclosed by the two dashed lines indicate modelled values more than a factor of 2 above or below the observed value. The R^2 values and the root mean squared error (RMSE) are also included in figure 37. An R^2 value of 1 would indicate perfect model versus observation agreement while a low value indicates no agreement. The smaller the value of the RMSE, the better the model agreement. The R^2 value for model scenario 1 is 0.78, indicating a correlation between the modelled and the observed values of the total particle volume. The R^2 value of model scenario 2 is only 0.01 indicating a poor correlation. The model scenario 1 shows an acceptable agreement to the measured values. Model scenario 2 does not fit the measured values as well. The much higher correlation between scenario 1 and the observed than scenario 2 and the observed shows that the model scenario 1 better represents the observed conditions at Høvsøre. This may be interpreted as the marine anthropogenic particle sources contributing significantly to the aerosol distribution at Høvsøre.

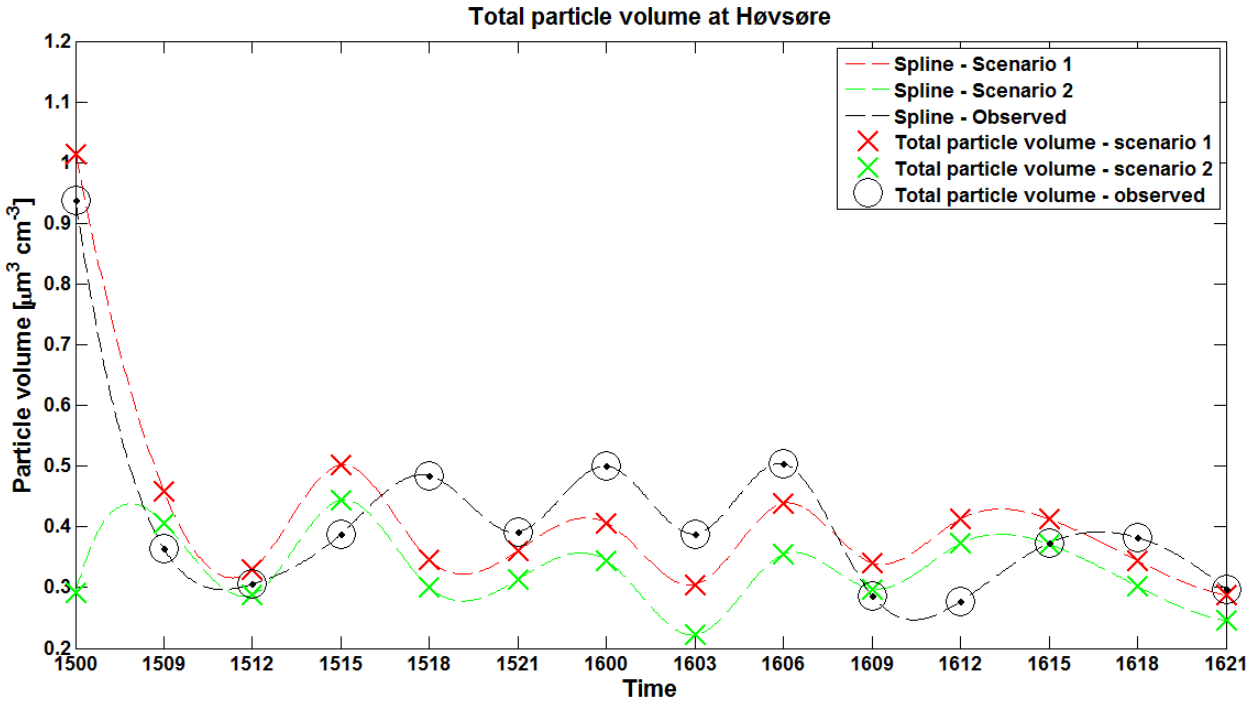

Figure 36: The modelled and measured total particle volume at Høvsøre for particle sizes with diameters in the size range 12–500 nm. Time in days and hours of the format "ddHH".

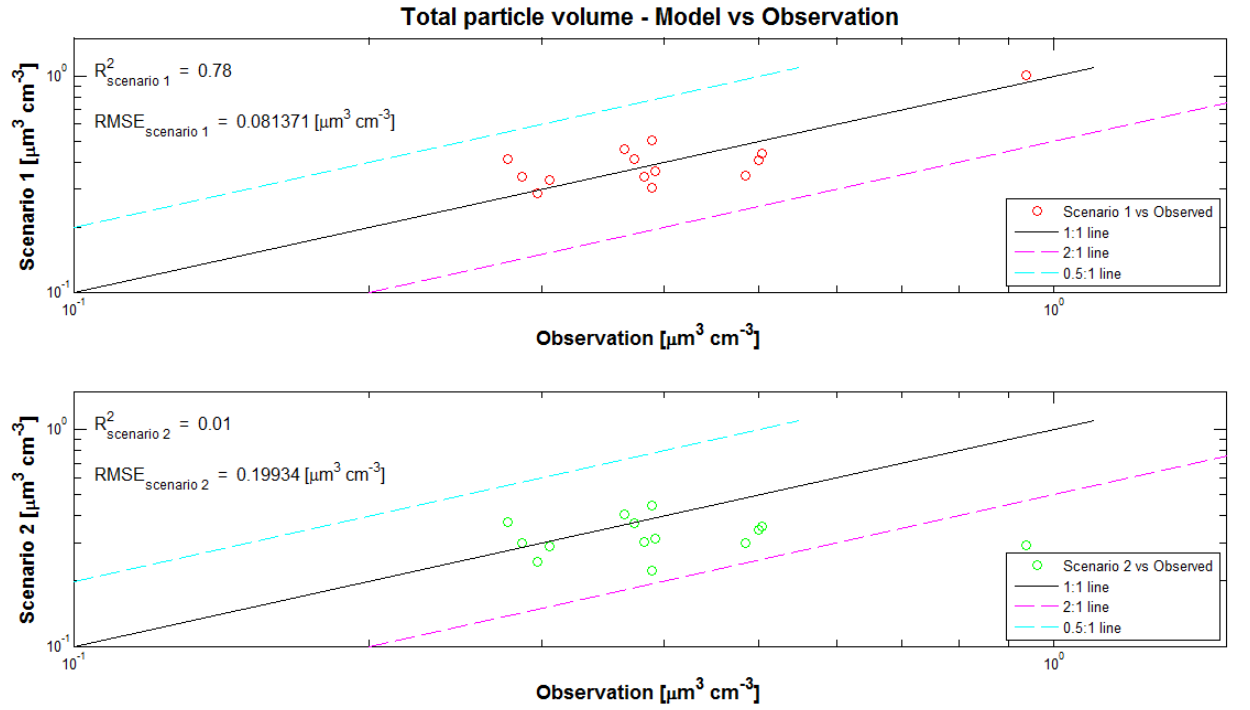

Figure 37: Modelled versus observed total particle volume for particle sizes with diameters in the size range 12–500 nm. The solid line represents 1:1 and perfect model agreement. The two dashed lines represent an over respectively underestimation by a factor of 2. The R^2 values and the RMSE values are given for both model scenarios respectively.

8.2.2 Modelled size distributions at Høvsøre – results

The modelled particle number size distributions at Høvsøre are shown in figure 38 (top and middle) for both of the emission scenarios. The plots were constructed by adding together the extracted number size distributions from 14 trajectory simulations arriving at Høvsøre with an interval of 3 hours.

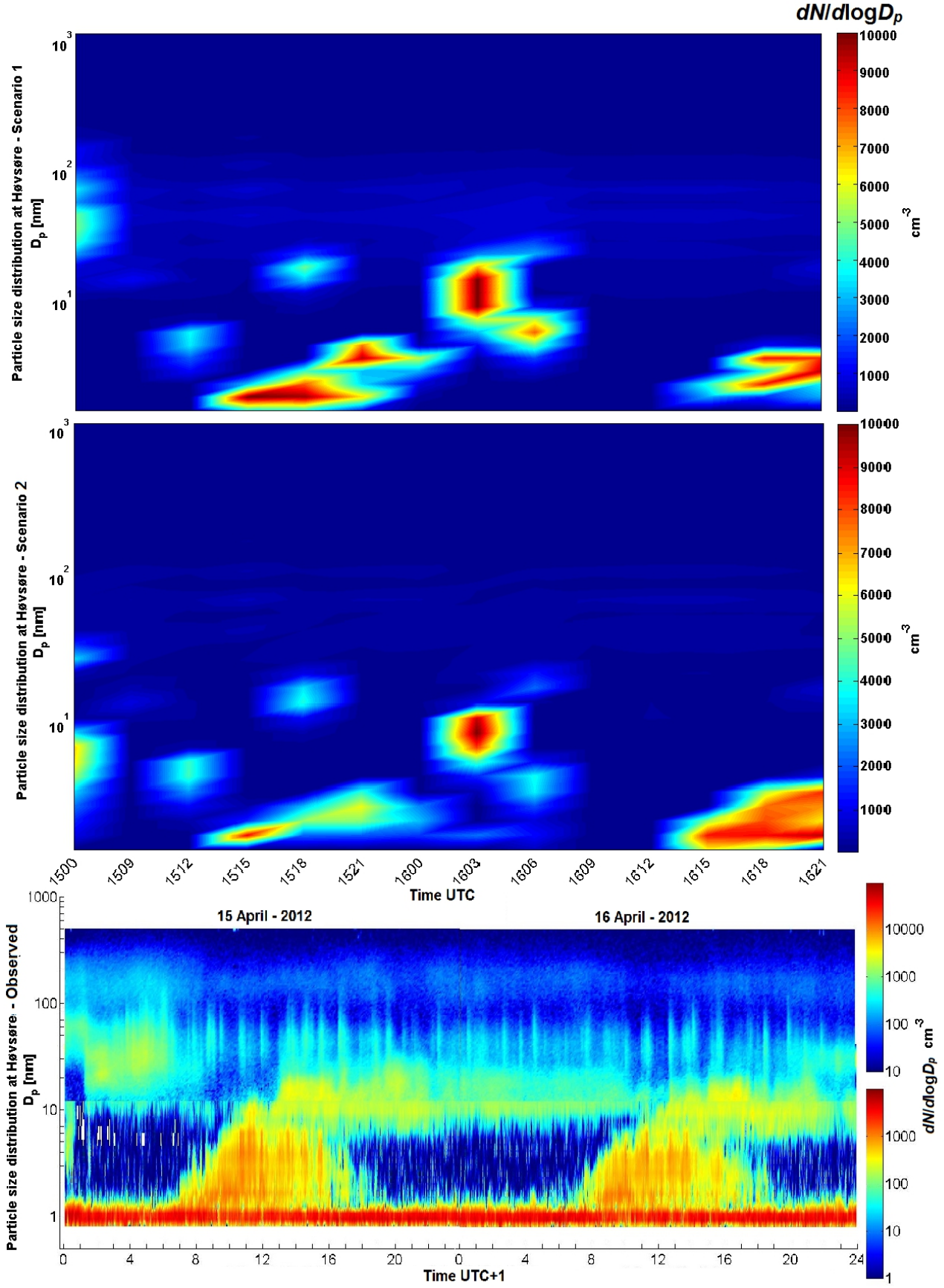

Figure 38: Modelled particle number size distribution at Høvsøre. ***Top:*** *Scenario 1.* ***Middle:*** *Scenario 2 – no marine anthropogenic emissions included. The displayed figures are composites of 14 trajectories arriving at Høvsøre with 3 hours interval. Time in days and hours of the format "ddHH".* ***Bottom:*** *Observed particle number distributions at Høvsøre during the simulation period. Particle diameters less than 12 nm are from AIS data (lower colorbar). The upper size range is derived from SMPS data (upper colorbar). Time in hours (UTC +1).*

The first two simulations plotted are exceptions with the interval 9 hours due to missing data in the two intermediate trajectories. The figures have been interpolated in time and particle size in order to better illustrate the evolution of the particle distributions.

The simulation of scenario 1 shows NPF formation from noon until 9 pm the 15th April. The new particle mode grows for 18 hours to particle diameters of 10-20 nm. NPF is also modelled at the 16th of April; a mode originating from NPF is apparent between 12 pm and 9 pm.

The simulation of scenario 2 shows NPF occurring at the same times as for the simulation of scenario 1. During the modelled NPF the 15th April, the particles grow to sizes just exceeding 10 nm in particle diameter. The results of the scenario 2 simulation also show high particle concentrations below 10 nm at midnight the 15th of April and strong NPF below 5 nm during the 16th of April.

Figure 39 shows the calculated difference ($\Delta dN/d\log D_p$) of the two particle number size distributions. The difference was calculated by subtracting the $dN/d\log D_p$ in each size bin of scenario 2 from that of scenario 1. Thus, a negative value indicates less modelled particles in scenario 2 while a positive value indicates an increase in the number of particles when anthropogenic marine emissions are not included in the simulations.

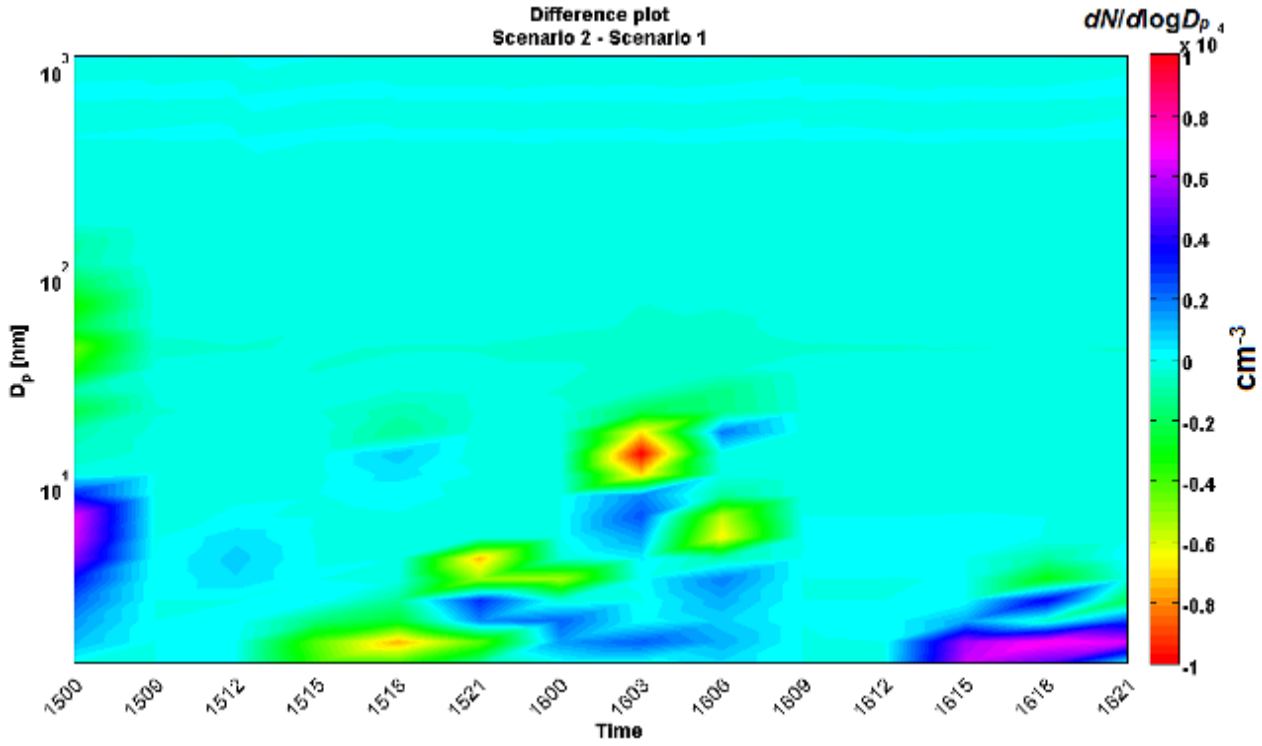

Figure 39: Difference plot of the two modelled particle number size distributions at Høvsøre. The color scale indicates an increase or decrease of the weighted particle concentrations with the same magnitude as the color scale in figure 39.

The difference calculation of figure 39 displays an overall decrease in the particle concentrations in scenario 2 compared to scenario 1. This decrease is most evident at sizes corresponding to the Aitken mode and also during the formation and growth of particles formed from NPF. There is however an increase in the particles originating from NPF at times when the modelled Aitken mode of scenario 1 is strong.

8.2.3 *Modelled NPF upwind of Høvsøre - results*

When the trajectories were between 0-24 hours upwind of Høvsøre, the geographical coordinates were stored for the periods when the model simulations showed NPF. The resulting coordinates were plotted separately for each day in a similar manner to the described NanoMap procedure. The results of the modelled NPF upwind of Høvsøre are shown in figure 40 where each model scenario is plotted separately.

The modelled scenarios display NPF in similar geographical areas but with local variations. The largest differences of the location of the NPF is observed off the Norwegian west-coast. The area where NPF is modelled during both days is largest for scenario 1 (light blue colours in figure 40). This area is found just south of Norway in the North Sea.

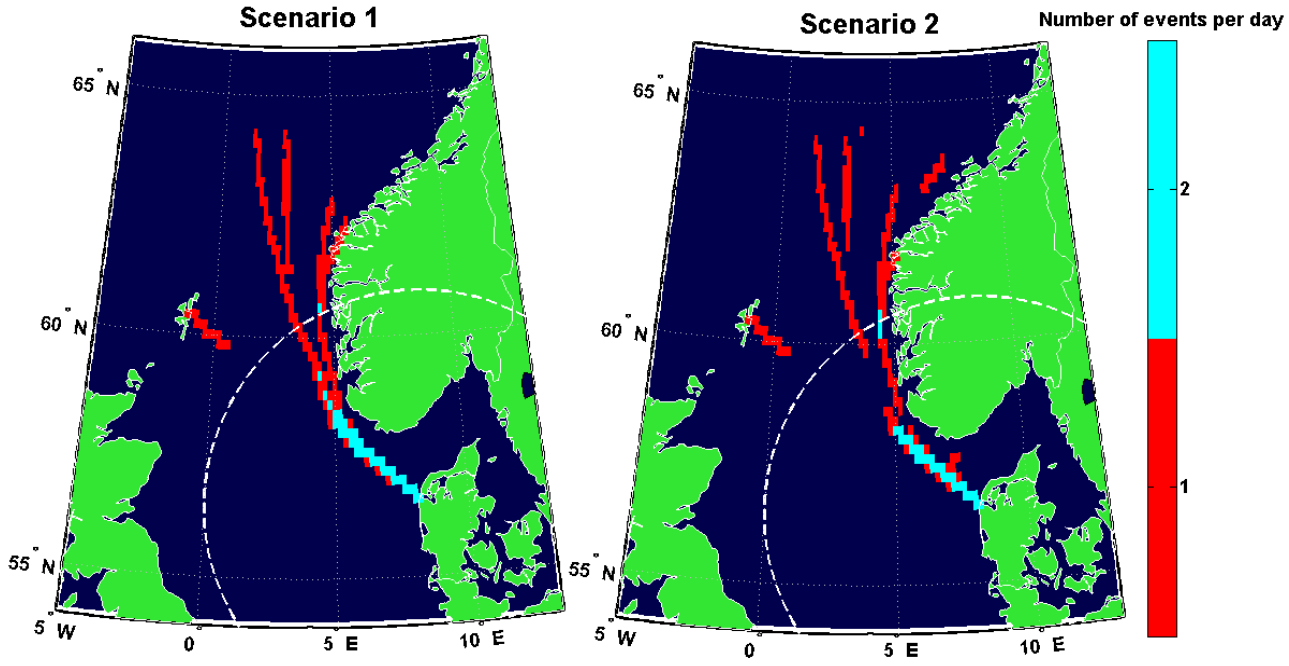

Figure 40: Modelled NPF 0-24 hours upwind of Høvsøre displayed for both scenario 1 (left) and scenario 2 (right).The dashed white circle represents a distance of 500 km from Høvsøre.

The difference between the geographical location of the two scenarios shown in figure 40 is available in figure 41, where the modelled NPF of Scenario 1 was subtracted from scenario 2. In the resulting plot, areas with less number of events per day indicate where anthropogenic emissions increase the NPF. Similarly, areas with more events per day indicate a decrease in the NPF caused by anthropogenic marine emissions. Areas with an increase in NPF due to anthropogenic emissions are found just west of the Norwegian south-west coast in the North Sea. Areas indicating the opposite are the yellow areas to the south and north of the Norwegian west-coast.

For sea areas only, the total area of the NPF represented by the grid was also calculated and compared between the two scenarios. The result found was an increase by 6% in the area of the modelled NPF over marine areas, as a result of including anthropogenic marine particulate and gas phase emissions in the model simulation.

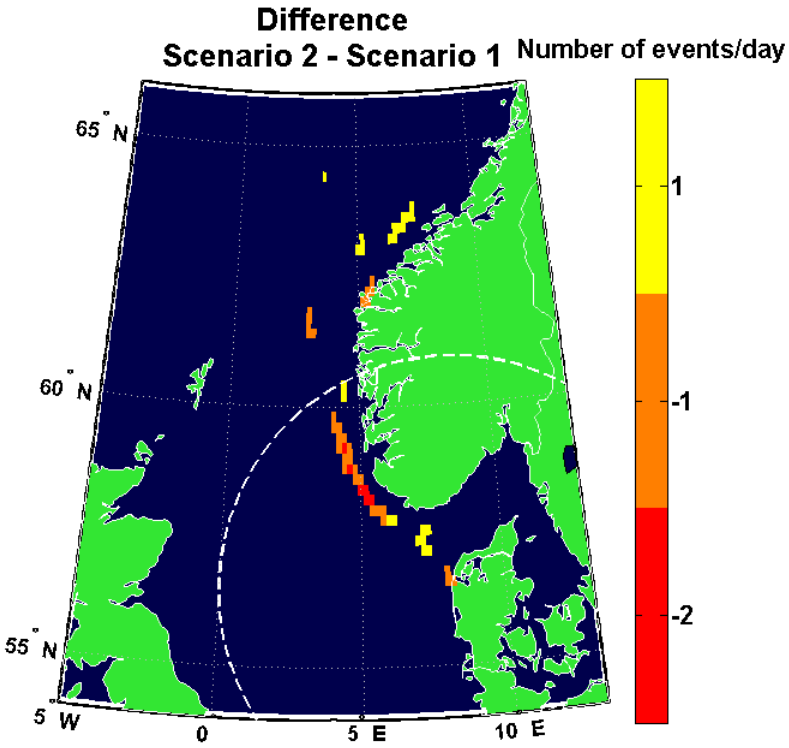

Figure 41: Quantitative comparison between the two scenarios of the geographical location of the modelled NPF 0-24 hours upwind of Høvsøre. Positive values indicate more NPF in model scenario 2 while negative values indicate more NPF in model scenario 1. The dashed white circle represents a distance of 500 km from Høvsøre.

9 Discussion

9.1 Task 1 – NanoMap

The NanoMap results show indeed that NPF is a rather frequent phenomena over sea areas in both the North Sea, Baltic Sea and the Mediterranean Sea. The inferred number of days with NPF therefore gives a crude, however direct, answer to the first aim of this project.

The calculated probability plots should be treated with caution. Since the inferred probabilities have not been verified, it is unlikely that these probabilities represent the actual probability in all areas where NPF was inferred. The presented probabilities are more likely to be close to the actual probability if the number of trajectories passing a grid cell was large. For statistical reasons, it could therefore be in order to neglect probability results in areas calculated from a low number of trajectory counts. To account for the uncertainties regarding the probability, weighted NanoMap results from several nearby measurement stations may provide more accurate probabilities.

Nonetheless, it is worth highlighting that the NanoMap results of the Preila data displays low NPF in the Eastern and Northern Gotland Basin of the Baltic Sea. In all other areas and at similar distances from Preila, the probability of an event is higher than three percent while in this area, the probability is between 0-1.5 %. Moreover, the number of events are higher west of Preila while the

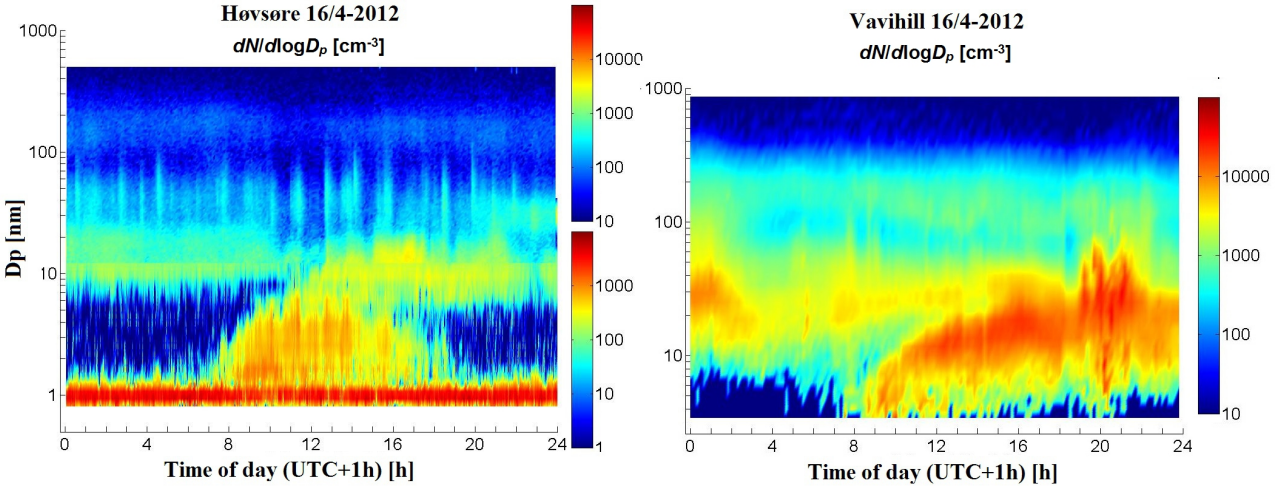

Figure 42: Illustration of the relatively weaker NPF and growth of the new mode to larger sizes in Høvsøre compared to Vavihill measurement. Left: Høvsøre size distribution 16/4-2012. Right: Vavihill size distribution 16/4-2012.

probability is highest to the east and south of Preila. This could indicate that terrestrial and forested areas have much higher event probability than sea areas. Such a result is evident in comparisons of coastal measurement stations to more continental stations (Manninen et al., 2010).

The three months data from Høvsøre makes evident a higher event frequency and event probability for airmasses with a cyclonic trajectory and a history from polar regions. For these airmass trajectories, the calculated event probability is similar to the event probability at the Høvsøre station. Interestingly, the results in figure 33 show very few inferred events over land areas. This could be due to the limited time of the measurement, but could have several explanations. It may indicate that the NPF in these cases are suppressed by e.g. land based or marine pollution sources. It may oppositely indicate that emissions from sea areas are necessary to initiate the NPF in this region. It is furthermore possible that a closer comparison of the strength of both the NPF and subsequent growth may reveal that the observed NPF at Høvsøre is weaker than for continental stations like Vavihill or Hyttiällä. An example of weaker NPF between Høvsøre and Vavihill is shown in figure 42. Thus, comparably weak emissions of Aitken or accumulation mode particles

may provide a large enough condensation and coagulation sink to inhibit the NPF when the airmass is situated over marine areas. This may partly explain the low number of inferred events over land areas.

The region south of Finokalia and the Aegean sea are evidently areas where NPF is very frequent while areas east and west of Finokalia show very little NPF. The region of high NPF probability south of Finokalia clearly shows NPF occurring in the marine atmosphere. This area is relatively far from both the European and the African continents and without islands which excludes any influence from terrestrial vegetation near the site. However, the areas north and south of Finokalia are areas with heavy ship traffic which is displayed by the large amount of annual SO_2 emissions as modelled by EMEP (figure 43).

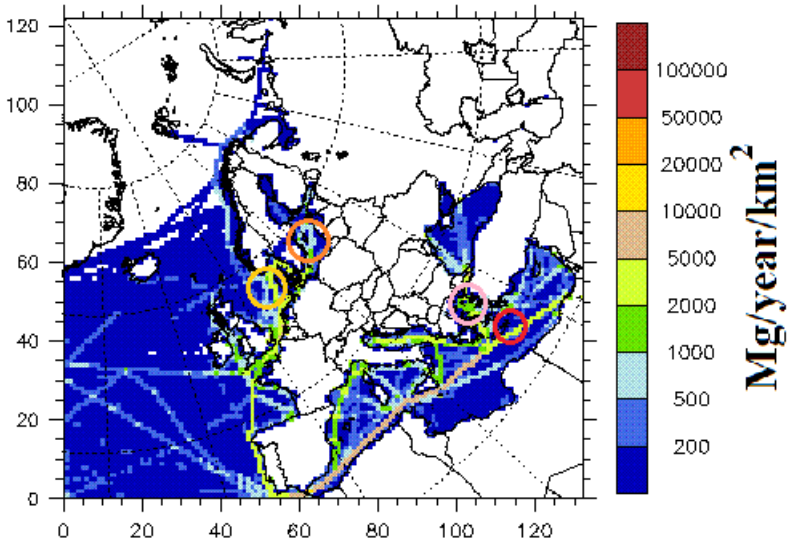

Figure 43: Ship emissions of SO_2 as modelled by EMEP. Coloured circles denotes areas of heavy ship traffic in the vicinity of the three measurement sites. The red circle to the right displays the region of interest south of Finokalia. (Source: WebDap, www.ceip.at).

In the area of high event probability south of Finokalia, shipping emissions are thus the only large anthropogenic pollution source. The area of high event probability north of Finokalia, in the Aegean Sea, is also heavily polluted by shipping emissions. It is however clear from the trajectory analysis that a large part of these trajectories arrives from the north, thereby passing quite polluted and densely populated land areas before reaching the Aegean Sea.

To this date, the only peer reviewed published results of a NanoMap analysis is the article by Kristensson et al. (2014). Kristensson et al. (2014) concludes that the NanoMap method may be used in order to identify the regional CCN concentration deriving from NPF. A combination of the probability results presented in this project and a qualified estimate of the fraction of particles formed by NPF that survives to sizes relevant for CCN activation may consequently be used to improve climate model predictions.

9.2 Task 2 - ADCHEM

The ADCHEM model simulations of the conditions at Høvsøre and the comparison to observations at the site, indicates that the model may be used to simulate both particle background sources and NPF, for a qualitative assessment of the impact of anthropogenic marine emissions on NPF. Improvements to the model are discussed in chapter 11. It should be noted that due to the short simulation time (2 days), the interpretation of the results should be treated with caution and it is possible that the conclusions may not be generalized to all plausible conditions.

The difference between the two model scenarios in the modelled particle number size distribution at Høvsøre shown in figure 39 is more pronounced at larger particle diameters. From the separate illustrations of the simulations, at midnight the 15th of April, the strong Aitken mode visible in scenario 1 (figure 38, top) originates from anthropogenic marine emissions (i.e. primary ship particles). This mode is not apparent in scenario 2 (figure 38, middle). In the absence of the strong Aitken mode, NPF is observed in scenario 2 and not in scenario 1. This result indicates that ship particle emissions may lower the amount of nucleated particles that survives to grow to larger sizes, by acting as a coagulation sink, effectively scavenging the nucleated particles. The absence of NPF due to the Aitken mode in scenario 1 may also be due to a lower nucleation rate. The lower nucleation rate is explained by the larger surface area on which the existing condensable gases may condense rather than to participate in homogeneous nucleation. The combined effect of these two explanations to the modelled deficiency of nucleation mode particles in airmasses characterised by large shipping emissions leads to the conclusion that in some cases, anthropogenic marine particulate emissions may drastically decrease NPF.

NPF is moreover not absent in scenario 2. This indicates that the condensable vapours originating from both marine and terrestrial biogenic sources and terrestrial anthropogenic sources induce atmospheric vapour concentrations high enough to initiate NPF in the marine atmosphere. This means that NPF in the marine atmosphere is not solely dependent on anthropogenic marine emissions. Although observations of NPF in the marine boundary layer are scarce, marine NPF has been observed in biologically active areas and during times with relatively high solar radiation (e.g. O'Dowd et al., 2010). The NPF modelled in scenario 2 may thus be due to a high biological activity resulting in high emissions of DMS, which increases the sulphuric acid concentration, and possibly, high emissions of isoprene which may result in an increased concentration of VOCs with a low volatility.

In the absence of a strong Aitken mode, scenario 1 generally demonstrates a higher nucleation rate and growth rate. An increase in the maximum sizes that these particles may grow to is further evident. Thus the difference between the modelled size distributions at Høvsøre suggests that anthropogenic marine gas phase emissions increase the amount of nucleated particles. Moreover, considering the full simulation period, the difference between the scenarios displayed in figure 39 demonstrates that in total, the NPF is increased by the anthropogenic marine emissions in scenario 1. This increase indicates that the positive effects on NPF from anthropogenic marine emissions of condensable gases may be larger than the negative effect on NPF from the anthropogenic marine emissions of particulate matter.

In the simulated NPF of scenario 2, a closer analysis of the source dependence of the NPF would be advisable for further studies. Since several observations of sub-micron particles indicate that NPF is not frequently occurring in the clean marine boundary layer (e.g. Heintzenberg et al., 2004), the source of the condensable gases required to model NPF in scenario 2 is an interesting subject. A thorough analysis of the condensable gases participating in the nucleation and the chemical composition of the particles themselves is beyond the scope of this project. However, these results may generate new research questions, which among one is the dependence on marine NPF attributed to marine biogenic VOC and DMS emissions. In the modelling study of Pirjola et al. (2000) it was found that the sulphuric acid derived from DMS emissions may explain the formation of stable clusters and the nucleation of particles with diameters of 1-2 nm. The growth of these particles could not be explained solely by the presence of sulphuric acid, which indicates the important role of low volatile VOCs in the growth of the newly formed particles.

At Høvsøre, the modelled size distribution of particles formed by NPF demonstrates a negligible contribution to the particle concentrations with diameters larger than 50 nm, relevant for CCN activation. Thus, the climate impact of the particles formed by nucleation in the marine atmosphere may be of low importance. However, Merikanto et al. (2009) modelled the contribution from

nucleation in the boundary layer to the CCN concentration. It was then concluded that nucleation of particles in the marine boundary layer over the North Atlantic may contribute to as much as 10 % of the total CCN concentration. Therefore, the low concentration of particles relevant for CCN activation modelled at Høvsøre in this study may not be representative for the full area of the simulation.

The most striking feature of the geographical differences in the modelled nucleation upwind of Høvsøre, illustrated in figure 40-41, is perhaps the more concentrated area where NPF occurs in scenario 1 compared to scenario 2. This area, mainly just off the Norwegian south-west coast in the North Sea, is characterised by both large on-shore and off-shore anthropogenic emissions, displayed by the modelled NMVOC emission by EMEP (figure 44, top). Furthermore, the NO_x emissions are a proxy for particulate shipping emissions, which suggests large particulate emissions in the area (figure 44, bottom). Furthermore, the increase by 6 % in the total area where NPF was modelled 0-24 hours upwind of Høvsøre, in scenario 1 compared to scenario 2, indicates similar to the modelled size distribution at Høvsøre that the net effect of shipping emissions may be an increase rather than a decrease of NPF.

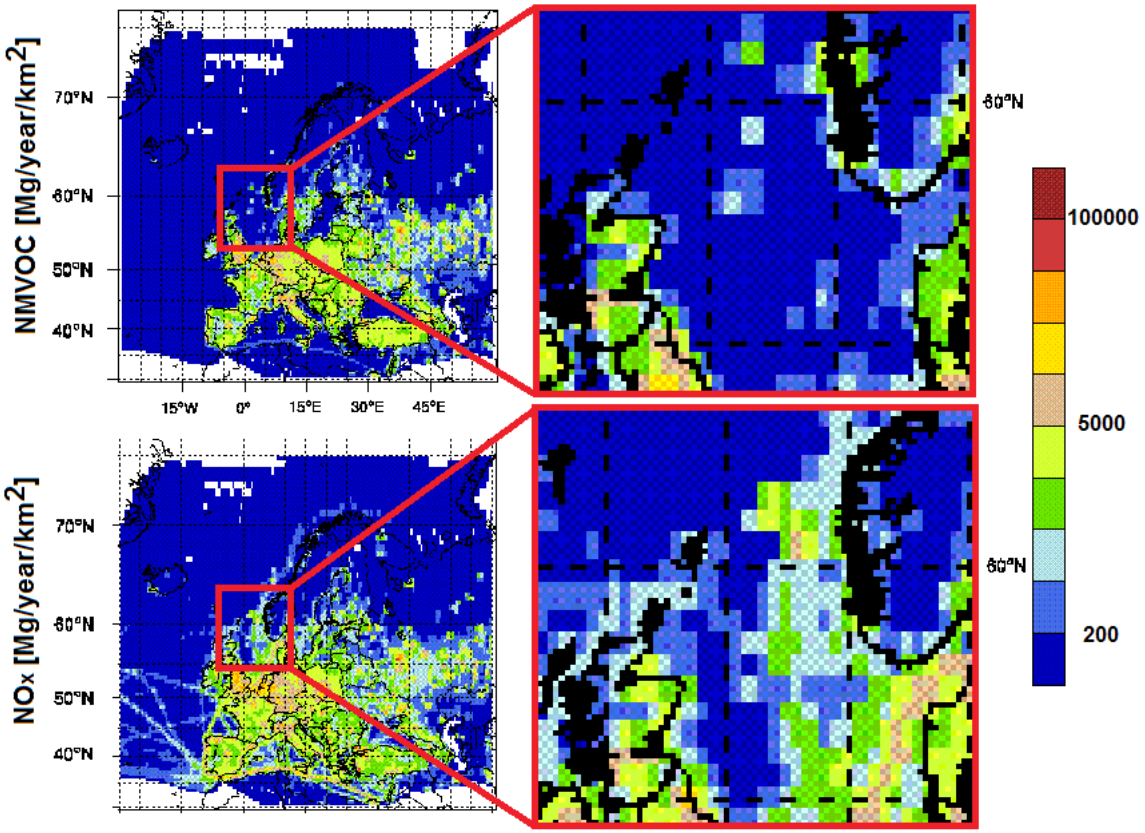

Figure 44: Yearly emissions of NMVOC and NO_x as modelled by EMEP. The North Sea area is displayed to the right. Data source: WebDap, www.ceip.at).

Combining the analysis of the anthropogenic influence on NPF at Høvsøre and the modelled NPF upwind of Høvsøre, it may be concluded that anthropogenic marine emissions do impact NPF. This impact most likely has two sides. Particulate emissions from shipping likely have a lowering effect on NPF in the marine atmosphere. Since an increase in the NPF is also observable in the comparison of the two scenarios, there is likely also an increase in the NPF deriving from the anthropogenic gas phase emissions. These findings demonstrate that if the particulate emissions were to decrease significantly, an increased number of NPF events would most likely be observed.

In Emission Control Areas (ECAs), new international legislations coordinated by the international

and maritime organization (IMO) which will be effective from the 1st of January 2015, requires the shipping industry to lower the sulphur emissions to approximately a tenth of today's values (van Aardenne et al., 2013). Since sulphur species largely contributes to the sulphuric acid concentration, the new legislations may result in a decrease of the NPF. If the legislation is applied to particulate matter as well, the lowered emissions may subsequently result in an increase of the NPF. This increase would be the result of a lowered condensation and coagulation sink. However, it may also be possible that the emissions of NMOVCs, which are currently not controlled by the legislation, contributes to the growth rate of the nucleated particles. The relative importance of these emissions are thus likely to increase.

As a consequence, new legislations regulating the emissions from international shipping, have the possibility to result in either an increase or a decrease of NPF in the North Sea and at nearby measurement stations.

9.3 Comparison between ADCHEM and NanoMap

The geographical location of the modelled NPF (figure 40) may further be compared to the inferred NPF of the NanoMap analysis. The comparison provides an attempt to verify the NanoMap results. It is, however, important to recognise the short simulation time (2 days) and the uncertainty of the ADCHEM model results. The results of the comparison should therefore be treated with caution.

NPF was observed at Høvsøre during the 15th and 16th of April 2012. Furthermore, NPF was also observed at the measurement station in Vavihill during the 15th of April 2012. The NanoMap results of the two observations are included in figure 45. The areas displaying modelled and inferred NPF are to a large extent consistent. This result implies that the NanoMap analysis may indeed provide a simple and user friendly method from which the extent of the regional NPF may be determined. The ability to determine the number of NPF events in an area is however decreased by the few measurement sites available.

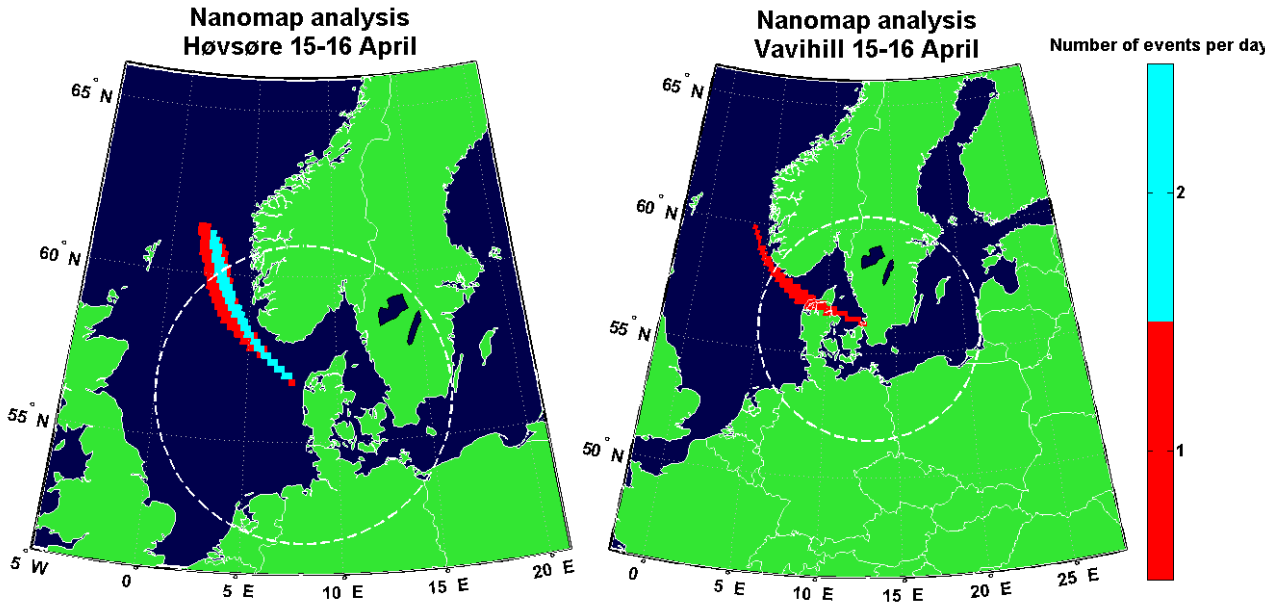

Figure 45: Inferred nucleation of particles at sizes of 1.5 nm in diameter derived using the NanoMap analysis and data from Høvsøre (left) and Vavihill (right). White circles represents a distance of 500 km from the measurement sites.

10 Summary and conclusions

Two separate methods were applied to address the aims formulated in chapter 2. The outcome of the results has provided new information on the geographical extensiveness of NPF in several marine areas. Moreover, the results permitted a qualitative assessment of the anthropogenic impact on the NPF in marine areas.

The results of the first method, the NanoMap method, that were used to address the first aim indicates that NPF is frequently occurring in several coastal waters and marine areas off the European coast. The NanoMap results, on average, show a higher frequency and a higher probability of NPF events in the marine areas heavily polluted by shipping. It is however not clear if the high frequency of NPF in these areas are due to the shipping emissions. It is also suggested that the calculated probability plots may further provide a basis for improving modelling of the CCN sources in global and regional climate models.

To address the second aim, the NPF was studied using the aerosol dynamics model ADCHEM. From the modelling study, it may be concluded that anthropogenic marine emissions do impact the NPF in the marine atmosphere. However, the simulations show that NPF in the marine atmosphere does not always depend on anthropogenic marine emissions alone. Moreover, the results of the simulations suggest that anthropogenic marine particulate emissions may in some cases reduce the NPF. Nonetheless, it was seen that the combined effect of anthropogenic marine emissions of particulate matter and condensable vapours may in fact result in an increase of the NPF. The latter model result was concluded from both the simulation of the particle number size distribution at the measurement site in Høvsøre, on the north-west coast of Denmark, and from the modelled NPF 0-24 hours upwind of Høvsøre.

To alter the cloud properties and the radiative balance in the atmosphere, the nucleated particles generally must grow to sizes where they effectively gain CCN properties. The impact from anthropogenic marine emissions on the ability of particles formed by nucleation to contribute to the CCN concentration was deemed to be low or negligible at Høvsøre. It is however not clarified if this result is representative for the whole area simulated also upwind of Høvsøre. Therefore, further studies on the subject may provide stronger evidence.

The ADCHEM modelling results were, in addition, compared to the NanoMap results, providing a first estimate of the NanoMap accuracy. The ADCHEM model results were found to be largely consistent with the NanoMap results.

As a final concluding remark, the results found by simulating the NPF in the North Sea suggests that new shipping emission control legislations may either decrease or increase the NPF. The final magnitude of the decrease or increase in the NPF will most likely principally depend on the relative reduction in particulate emissions contra sulphur emissions.

11 Outlook

The methods and results used and found in this project have the potential to generate new research questions, some of which proposed in the discussion (chapter 9). The results also enables suggestions for improvements of the methods used in this project.

The NanoMap results presented in this project may together with climate models allow improved predictions of the CCN concentrations and climate effects from the NPF in marine areas. However, in order to decrease the NanoMap uncertainty, the probability calculations should be evaluated further. The probabilities inferred are difficult to verify. Therefore a project well suited for further studies with the NanoMap method would include a methodology to assess these calculations.

To further improve on the NanoMap results, it would also be informative to further evaluate the correlation between the inferred NPF and areas characterised by large emissions. These emissions may include both anthropogenic and biogenic sources.

Regarding the ADCHEM simulations, only a fraction of the results produced using the ADCHEM model were finally analysed and presented in this project. To complement the findings, an in-depth analysis of the chemical species responsible for the differences in the two model scenarios is a task with the possibility to greatly enhance the understanding of marine NPF.

In general, for results to be trustworthy, a model should be calibrated and evaluated using independent observational data. The sensitivity of the model should also be analysed thoroughly with respect to small changes in the parameters. Much of this work has been done previously with other observations than from Høvsøre (i.e. Roldin, 2013). However, due to the large uncertainties of several parameters included in the model, a complete analysis of the steps recently mentioned may be done to improve the results of this project. If possible, a comparison of modelled data to observations both upwind and downwind of Høvsøre or a similar site may be used to calibrate the model. This would most likely allow the conditions to be simulated more accurately.

Since the nucleation parametrisation is highly uncertain, a Monte-Carlo based modelling approach with small random perturbations to the parameters and the nucleation mechanism itself may provide model results including an estimate of the model uncertainty. The drawback of Monte-Carlo simulations is generally the increased amount of simulation time required. The ADCHEM simulation of the 14 airmass trajectories in this project required on average 12 hours each for completion. In order to run multiple scenarios efficiently in a Monte-Carlo simulation set up, the ADCHEM model would most likely need to be used in large computer clusters. Preparing ADCHEM for computer clusters and super computers is currently in progress. Such a simulation has the potential to greatly enhance the ability to assess the results also of this project.

12 Self reflection

In this project two aims were formulated from the hypothesis. The main research question underlying the aims, the anthropogenic effect on NPF, is currently not well understood, yet a better understanding has the possibility to greatly improve climate model uncertainties.

To answer the aims, data were collected from a number of measurement sites. Meteorological data were obtained and a number of models were applied. This work required me (the author) to learn how to use several tools currently used in aerosol, atmospheric and climate research. The observational data collected required me to furthermore improve my understanding of these frequently used measurement techniques and to study the theory of aerosol particle motion from which these methods were developed.

The modelling of aerosol properties using the ADCHEM model required me to: (1) attain the required understanding of aerosol dynamics in the atmosphere, including condensation, coagulation and deposition, (2) critically evaluate the available literature in order to develop a simple sea-air gas-flux model, (3) learn some basics in a (computer) language commonly used in atmospheric research (FORTRAN), (4) evaluate the necessary input sources (shipping, BVOCs, etc.) required to realistically model NPF and aerosol dynamics and (5) calibrate and use a state of the art research model (ADCHEM) for addressing one of the aims of this project.

The NanoMap method was improved during the project. A first assessment of the NanoMap method made clear that it was necessary to interpolate data, as information was lost when the grid resolution was increased. Furthermore, an existing method to infer NPF probability in the NanoMap analysis was available at the start of this project. The results were however questionable since they often had probabilities a thousand or a million times lower than at the station from which data were used. During this project, the calculation of the inferred probability could be improved by evaluating the available NanoMap results. The use of first stage NanoMap results (the formation time) was implemented and the final calculation was changed, with the resulting probabilities now yielding more realistic values.

The NanoMap results were moreover presented by the author in a poster at the Nordic Society for Aerosol Research symposium in Stockholm, in January 2014.

The focus in this project is strictly on climate issues. Therefore critique is justified concerning the fact that the project did not elaborate further on aerosol health impacts. However, the necessity to exclude this important discussion arose as a consequence of the already broad field of study and the decision to focus on both the NanoMap method and modelling using ADCHEM. It is of course worth noting that in the long run, the anthropogenic climate change may pose an even larger threat to human health than the direct effects of aerosol particles do.

Furthermore, critique regarding the evaluation of the ADCHEM modelling results is also justified. A good lesson learnt during the time of this project is the importance of evaluating the time required for the gathering of data and the subsequent analysis respectively. In this project, it became clear that more data than could be evaluated had been collected. Therefore, with this in mind, to some extent the ADCHEM model could have been further evaluated to observational data and the accuracy of the results therefore better assessed, had more time been granted the analysis.

13 References

Aalto, P., Hämeri, K., Paatero, P., Kulmala, M., Bellander, T., Berglind, N., ... & Forastiere, F. (2005). Aerosol particle number concentration measurements in five European cities using TSI-3022 condensation particle counter over a three-year period during health effects of air pollution on susceptible subpopulations. *Journal of the Air & Waste Management Association*, *55*(8), 1064-1076.

Allen, M. D., & Raabe, O. G. (1982). Re-evaluation of Millikan's oil drop data for the motion of small particles in air. *Journal of Aerosol Science*, *13*(6), 537-547.

Asmi, E., Sipilä, M., Manninen, H. E., Vanhanen, J., Lehtipalo, K., Gagné, S., ... & Kulmala, M. (2009). Results of the first air ion spectrometer calibration and intercomparison workshop. *Atmospheric Chemistry and Physics*, *9*(1), 141-154.

Asmi, A., Wiedensohler, A., Laj, P., Fjaeraa, A. M., Sellegri, K., Birmili, W., ... & Kulmala, M. (2011). Number size distributions and seasonality of submicron particles in Europe 2008–2009. *Atmospheric Chemistry and Physics*, *11*(11), 5505-5538.

Broadgate, W. J., Liss, P. S., & Penkett, S. A. (1997). Seasonal emissions of isoprene and other reactive hydrocarbon gases from the ocean. *Geophysical Research Letters*, *24*(21), 2675-2678.

Chandler, D. (1987). Introduction to modern statistical mechanics. *Introduction to Modern Statistical Mechanics, by David Chandler, pp. 288. Foreword by David Chandler. Oxford University Press, Sep 1987. ISBN-10: 0195042778. ISBN-13: 9780195042771*, *1*.

Chang, R. Y. W., Sjostedt, S. J., Pierce, J. R., Papakyriakou, T. N., Scarratt, M. G., Michaud, S., ... & Abbatt, J. P. (2011). Relating atmospheric and oceanic DMS levels to particle nucleation events in the Canadian Arctic. *Journal of Geophysical Research: Atmospheres (1984-2012)*, *116*(D17).

Covert, D. S., Kapustin, V. N., Quinn, P. K., & Bates, T. S. (1992). New particle formation in the marine boundary layer. *Journal of Geophysical Research: Atmospheres (1984–2012)*, *97*(D18), 20581-20589.

Covert, David S., et al. "Aerosol number size distributions from 3 to 500 nm diameter in the arctic marine boundary layer during summer and autumn."*Tellus B* 48.2 (1996): 197-212.

Dal Maso, M., Kulmala, M., Riipinen, I., Wagner, R., Hussein, T., Aalto, P., & Lehtinen, K. (2005). Formation and growth of fresh atmospheric aerosols: eight years of aerosol size distribution data from SMEAR II, Hyytiala, Finland. *Boreal Environment Research*, *10*(5), 323-336.

Draxler, R.R., and G.D. Hess, 1997: Description of the HYSPLIT_4 modeling system. NOAA Tech. Memo. ERL ARL-224, NOAA Air Resources Laboratory, Silver Spring, MD, 24 pp.

Draxler, R. R., Hess, G. D., & Magazine, A. M. (1998). An Overview of the HYSPLIT_4 Modelling System for Trajectories, Dispersion, and Deposition. *Australian Meteorological Magazine*, *47*, 295-308.

Draxler, R.R., 1999: HYSPLIT4 user's guide. NOAA Tech. Memo. ERL ARL-230, NOAA Air Resources Laboratory, Silver Spring, MD.

Draxler and Rolph (2013). HYSPLIT (HYbrid Single-Particle Lagrangian Integrated Trajectory) Model access via NOAA ARL READY Website (http://ready.arl.noaa.gov/HYSPLIT.php). NOAA Air Resources Laboratory, Silver Spring, MD, USA.

Fitzgerald, James W. "Marine aerosols: A review." *Atmospheric Environment. Part A. General Topics* 25.3 (1991): 533-545.

Guenther, A. B., Monson, R. K., & Fall, R. (1991). Isoprene and monoterpene emission rate variability: observations with eucalyptus and emission rate algorithm development. *Journal of Geophysical Research: Atmospheres (1984–2012)*, *96*(D6), 10799-10808.

Guenther, A. B., Zimmerman, P. R., Harley, P. C., Monson, R. K., & Fall, R. (1993). Isoprene and monoterpene emission rate variability: model evaluations and sensitivity analyses. *Journal of Geophysical Research: Atmospheres (1984–2012)*, *98*(D7), 12609-12617.

Guenther, A. (1997). Seasonal and spatial variations in natural volatile organic compound emissions. *Ecological applications*, *7*(1), 34-45.

Heintzenberg, J., Birmili, W., Wiedensohler, A., Nowak, A., & Tuch, T. (2004). Structure, variability and persistence of the submicrometre marine aerosol.*Tellus B*, *56*(4), 357-367.

Houghton, J. T., Ding, Y., Griggs, D. J., Noguer, M., Van der Linden, P. J., Dai, X., ... & Johnson, C. A. (2001). IPCC, 2001: Climate Change 2001: The Scientific Basis. Contribution of Working Group I to the Third Assessment Report of the Intergovernmental Panel on Climate Change. *Cambridge, United Kingdom, New York, USA, Cambridge University Press*, *881*, 9.

Hu, Q. H., Xie, Z. Q., Wang, X. M., Kang, H., He, Q. F., & Zhang, P. (2013). Secondary organic aerosols over oceans via oxidation of isoprene and monoterpenes from Arctic to Antarctic. *Scientific reports*, *3*.

IPCC, 2007: Climate Change 2007: The Physical Science Basis. Contribution of Working Group I to the Fourth Assessment Report of the Intergovernmental Panel on Climate Change [Solomon, S., D. Qin, M. Manning, Z. Chen, M. Marquis, K.B. Averyt, M. Tignor and H.L. Miller (eds.)]. Cambridge University Press, Cambridge, United Kingdom and New York, NY, USA, 996 pp.

IPCC, 2013: Climate Change 2013: The Physical Science Basis. Contribution of Working Group I to the Fifth Assessment Report of the Intergovernmental Panel on Climate Change [Stocker, T.F., D. Qin, G.-K. Plattner, M. Tignor, S.K. Allen, J. Boschung, A. Nauels, Y. Xia, V. Bex and P.M. Midgley (eds.)]. Cambridge University Press, Cambridge, United Kingdom and New York, NY, USA, 1535 pp.

IPCC, 2013: Summary for Policymakers. In: *Climate Change 2013: The Physical Science Basis. Contribution of Working Group I to the Fifth Assessment Report of the Intergovernmental Panel on Climate Change* [Stocker, T.F., D. Qin, G.-K. Plattner, M. Tignor, S.K. Allen, J. Boschung, A. Nauels, Y. Xia, V. Bex and P.M. Midgley (eds.)]. Cambridge University Press, Cambridge, United Kingdom and New York, NY, USA,**in press**.

Jenkin, M. E., Saunders, S. M., & Pilling, M. J. (1997). The tropospheric degradation of volatile organic compounds: a protocol for mechanism development. *Atmospheric Environment*, *31*(1), 81-104.

Jenkin, M. E., Wyche, K. P., Evans, C. J., Carr, T., Monks, P. S., Alfarra, M. R., ... & Rickard, A. R. (2012). Development and chamber evaluation of the MCM v3. 2 degradation scheme for β-caryophyllene. *Atmospheric Chemistry and Physics*, *12*(11), 5275-5308.

Jonsson, Å. M., Westerlund, J., & Hallquist, M. (2011). Size-resolved particle emission factors for individual ships. *Geophysical Research Letters*, *38*(13).

Kettle, A. J. et al. (1999) A global database of sea surface dimethylsulfide (DMS) measurements and a procedure to predict sea surface DMS as a function of latitude, longitude and month. Global Biogeochem. Cycles 13, 399-444.

Kerminen, V. M., Lihavainen, H., Komppula, M., Viisanen, Y., & Kulmala, M. (2005). Direct observational evidence linking atmospheric aerosol formation and cloud droplet activation. *Geophysical research letters*, *32*(14).

Kivekäs, N., Massling, A., Grythe, H., Lange, R., Rusnak, V., Carreno, S. D., ... & Kristensson, A. (2014). Contribution of ship traffic to aerosol particle concentrations downwind of a major shipping lane. *Atmospheric Chemistry and Physics Discussions*, *14*(6), 8419-8454.

Kristensson, A., Johansson, C., Westerholm, R., Swietlicki, E., Gidhagen, L., Wideqvist, U., & Vesely, V. (2004). Real-world traffic emission factors of gases and particles measured in a road tunnel in Stockholm, Sweden. *Atmospheric Environment*, *38*(5), 657-673.

Kristensson, A., Dal Maso, M., Swietlicki, E., Hussein, T., Zhou, J., KERMINEN, V. M., & Kulmala, M. (2008). Characterization of new particle formation events at a background site in Southern Sweden: relation to air mass history. *Tellus B*, *60*(3), 330-344.

Kristensson et al. (2014). NanoMap: Geographical mapping of atmospheric nucleation through analysis of particle number size distribution and trajectory data. Accepted for publication in Boreal Environmental Research.

Kulkarni, P., Baron, P. A., & Willeke, K. (Eds.). (2011). *Aerosol measurement: principles, techniques, and applications*. John Wiley & Sons.

Kulmala, M., Vehkamäki, H., Petäjä, T., Dal Maso, M., Lauri, A., Kerminen, V. M., ... & McMurry, P. H. (2004). Formation and growth rates of ultrafine atmospheric particles: a review of observations. *Journal of Aerosol Science*,*35*(2), 143-176.

Kulmala, M., Laakso, L., Lehtinen, K., Riipinen, I., Dal Maso, M., Anttila, T., & ... Tammet, H. (2004). Initial steps of aerosol growth. *Atmospheric Chemistry And Physics*, *4*2553-2560.

Kulmala, M., Lehtinen, K. E. J., & Laaksonen, A. (2006). Cluster activation theory as an explanation of the linear dependence between formation rate of 3nm particles and sulphuric acid concentration. *Atmospheric Chemistry and Physics*, *6*(3), 787-793.

Kulmala, M. M., Kontkanen, J. J., Junninen, H. H., Lehtipalo, K. K., Manninen, H. E., Nieminen, T. T., &...Worsnop, D. R. (2013). Direct Observations of Atmospheric Aerosol Nucleation. *Science*, *339*(6122), 943-946.

Laakso, L., Grönholm, T., Rannik, Ü., Kosmale, M., Fiedler, V., Vehkamäki, H., & Kulmala, M. (2003). Ultrafine particle scavenging coefficients calculated from 6 years field measurements. *Atmospheric Environment*, *37*(25), 3605-3613.

Leith, D. (1987). Drag on nonspherical objects. *Aerosol science and technology*, *6*(2), 153-161.

Manninen, H. E., Nieminen, T., Asmi, E., Gagné, S., Häkkinen, S., Lehtipalo, K., ... & Kulmala, M. (2010). EUCAARI ion spectrometer measurements at 12 European sites–analysis of new particle formation events. *Atmospheric Chemistry and Physics*, *10*(16), 7907-7927.

Martensson, E. M., Nilsson, E. D., De Leeuw, G., Cohen, L. H., & Hansson, H. C. (2003). Laboratory simulations and parameterization of the primary marine aerosol production. *Journal of geophysical research*, *108*(D9), AAC15-1.

Matsunaga, S., Mochida, M., Saito, T., & Kawamura, K. (2002). In situ measurement of isoprene in the marine air and surface seawater from the western North Pacific. *Atmospheric Environment*, *36*(39), 6051-6057.

Merikanto, J., Spracklen, D. V., Mann, G. W., Pickering, S. J., & Carslaw, K. S. (2009). Impact of nucleation on global CCN. *Atmospheric Chemistry and Physics*, *9*(21), 8601-8616.

Meskhidze, N., & Nenes, A. (2006). Phytoplankton and cloudiness in the Southern Ocean. *Science*, *314*(5804), 1419-1423.

Nannoolal, Y., Rarey, J., & Ramjugernath, D. (2008). Estimation of pure component properties: Part 3. Estimation of the vapor pressure of non-electrolyte organic compounds via group contributions and group interactions.*Fluid Phase Equilibria*, *269*(1), 117-133.

O'Dowd, C. D., Geever, M., Hill, M. K., Smith, M. H., & Jennings, S. G. (1998). New particle formation: Nucleation rates and spatial scales in the clean marine coastal environment. *Geophysical Research Letters*, *25*(10), 1661-1664.

O'Dowd, C. D., Jimenez, J. L., Bahreini, R., Flagan, R. C., Seinfeld, J. H., Hämeri, K., ... & Hoffmann, T. (2002). Marine aerosol formation from biogenic iodine emissions. *Nature*, *417*(6889), 632-636.

O'Dowd, C., & De Leeuw, G. (2007). Marine aerosol production: a review of the current knowledge. *Philosophical Transactions of the Royal Society A: Mathematical, Physical and Engineering Sciences*, *365*(1856), 1753-1774.

O'Dowd, C., Monahan, C., & Dall'Osto, M. (2010). On the occurrence of open ocean particle production and growth events. *Geophysical Research Letters*, *37*(19).

Passant, N. R. (2002). Speciation of UK emissions of non-methane volatile organic compounds. *AEA Technology Report ENV-0545, Culham, Abingdon, United Kingdom*.

Paasonen, P., Nieminen, T., Asmi, E., Manninen, H. E., Petäjä, T., Plass-Dülmer, C., ... & Kulmala, M. (2010). On the roles of sulphuric acid and low-volatility organic vapours in the initial steps of atmospheric new particle formation. *Atmospheric Chemistry and Physics*, *10*(22), 11223-11242.

Petzold, A., Hasselbach, J., Lauer, P., Baumann, R., Franke, K., Gurk, C., ... & Weingartner, E. (2008). Experimental studies on particle emissions from cruising ship, their characteristic properties, transformation and atmospheric lifetime in the marine boundary layer. *Atmospheric Chemistry and Physics*, *8*(9), 2387-2403.

Pikridas, M., Riipinen, I., Hildebrandt, L., Kostenidou, E., Manninen, H., Mihalopoulos, N., ... & Pandis, S. N. (2012). New particle formation at a remote site in the eastern Mediterranean. *Journal of Geophysical Research: Atmospheres (1984–2012)*, *117*(D12).

Pirjola, L., O'Dowd, C. D., Brooks, I. M., & Kulmala, M. (2000). Can new particle formation occur in the clean marine boundary layer?. *Journal of Geophysical Research: Atmospheres (1984–2012)*, *105*(D21), 26531-26546.

Putaud, J. P., Raes, F., Van Dingenen, R., Brüggemann, E., Facchini, M., Decesari, S., ... & Wiedensohler, A. (2004). A European aerosol phenomenology—2: chemical characteristics of particulate matter at kerbside, urban, rural and background sites in Europe. *Atmospheric Environment*, *38*(16), 2579-2595.

Riipinen, I., Sihto, S. L., Kulmala, M., Arnold, F., Maso, M. D., Birmili, W., ... & Lehtinen, K. E. J. (2007). Connections between atmospheric sulphuric acid and new particle formation during QUEST III–IV campaigns in Heidelberg and Hyytiälä. *Atmospheric Chemistry and Physics*, *7*(8), 1899-1914.

Roldin, P., Swietlicki, E., Schurgers, G., Arneth, A., Lehtinen, K. E. J., Boy, M., & Kulmala, M. (2011). Development and evaluation of the aerosol dynamics and gas phase chemistry model ADCHEM. *Atmospheric Chemistry and Physics*, *11*(12), 5867-5896.

Roldin, P. (2013). *Process based Modelling of Chemical and Physical Aerosol Properties*

Relevant for Climate and Health (Doctoral dissertation, Lund University).

Saunders, S. M., Jenkin, M. E., Derwent, R. G., & Pilling, M. J. (2003). Protocol for the development of the Master Chemical Mechanism, MCM v3 (Part A): tropospheric degradation of non-aromatic volatile organic compounds.*Atmospheric Chemistry and Physics*, *3*(1), 161-180.

Seinfeld, J. H., & Pandis, S. N. (2006). *Atmospheric chemistry and physics : from air pollution to climate change / John H. Seinfeld, Spyros N. Pandis*. Hoboken, N.J. : Wiley, cop. 2006.

Simpson, D., Benedictow, A., Berge, H., Bergström, R., Emberson, L. D., Fagerli, H., ... & Wind, P. (2012). The EMEP MSC-W chemical transport model–technical description. *Atmospheric Chemistry and Physics*, *12*(16), 7825-7865.

Smiatek, G., & Steinbrecher, R. (2006). Temporal and spatial variation of forest VOC emissions in Germany in the decade 1994–2003. *Atmospheric Environment*, *40*, 166-177.

Spracklen, D. V., Carslaw, K. S., Kulmala, M., Kerminen, V. M., Mann, G. W., & Sihto, S. L. (2006). The contribution of boundary layer nucleation events to total particle concentrations on regional and global scales. *Atmospheric Chemistry and Physics Discussions*, *6*(4), 7323-7368.

Spracklen, D. V., Carslaw, K. S., Kulmala, M., Kerminen, V. M., Sihto, S. L., Riipinen, I., ... & Lihavainen, H. (2008). Contribution of particle formation to global cloud condensation nuclei concentrations. *Geophysical Research Letters*, *35*(6).

Stohl, A. (1998). Computation, accuracy and applications of trajectories—a review and bibliography. *Atmospheric Environment*, *32*(6), 947-966.

Stohl, A., Forster, C., Frank, A., Seibert, P., & Wotawa, G. (2005). Technical note: The Lagrangian particle dispersion model FLEXPART version 6.2.*Atmospheric Chemistry and Physics*, *5*(9), 2461-2474.

Tarrasón, L., Turner, S., & Fløisand, I. (1995). Estimation of seasonal dimethyl sulphide fluxes over the North Atlantic Ocean and their contribution to European pollution levels. *Journal of Geophysical Research: Atmospheres (1984–2012)*,*100*(D6), 11623-11639.

Taylor F.W. (2005). *Elementary climate physics*. Oxford: Oxford University Press.

Tunved, P., Strom, J., & Krejci, R. (2013). Arctic aerosol life cycle: linking aerosol size distributions observed between 2000 and 2010 with air mass transport and precipitation at Zeppelin station, Ny-Alesund, Svalbard. *Atmospheric Chemistry And Physics*,*13*(7), 3643-3660.

Vana, M., Ehn, M., Petaja, T., Vuollekoski, H., Aalto, P., de Leeuw, G., & ... Kulmala, M. (2008). Characteristic features of air ions at Mace Head on the west coast of Ireland. *Atmospheric Research*, *90*(2-4), 278-286.

van Aardenne, J., Colette, A., Degraeuwe, B., Hammingh, P., & De Vlieger, I. (2013). *The impact of international shipping on European air quality and climate forcing* (Vol. 4).

Wallace, John M. and Peter V. Hobbs. Atmospheric Science; *An Introductory Survey*. Elsevier. Second Edition, 2006.

Wiedensohler, A., Covert, D. S., Swietlicki, E., Aalto, P., Heintzenberg, J., & Leck, C. (1996). Occurrence of an ultrafine particle mode less than 20 nm in diameter in the marine boundary layer during Arctic summer and autumn. *Tellus B*, *48*(2), 213-222.

Wiedensohler, A., Wehner, B., & Birmili, W. (2002). Aerosol number concentrations and size

distributions at mountain-rural, urban-influenced rural, and urban-background sites in Germany. *Journal of aerosol medicine*, *15*(2), 237-243.

World Health Organisation. (2002). The World health report: 2002: Reducing risks, promoting healthy life.

Yelland, M., & Taylor, P. K. (1996). Wind stress measurements from the open ocean. *Journal of Physical Oceanography*, *26*(4), 541-558.

Zhang, R., Khalizov, A., Wang, L., Hu, M., & Xu, W. (2012). Nucleation and Growth of Nanoparticles in the Atmosphere. Chemical *Reviews*, *112*(3), 1957-2011.

14 Appendix A

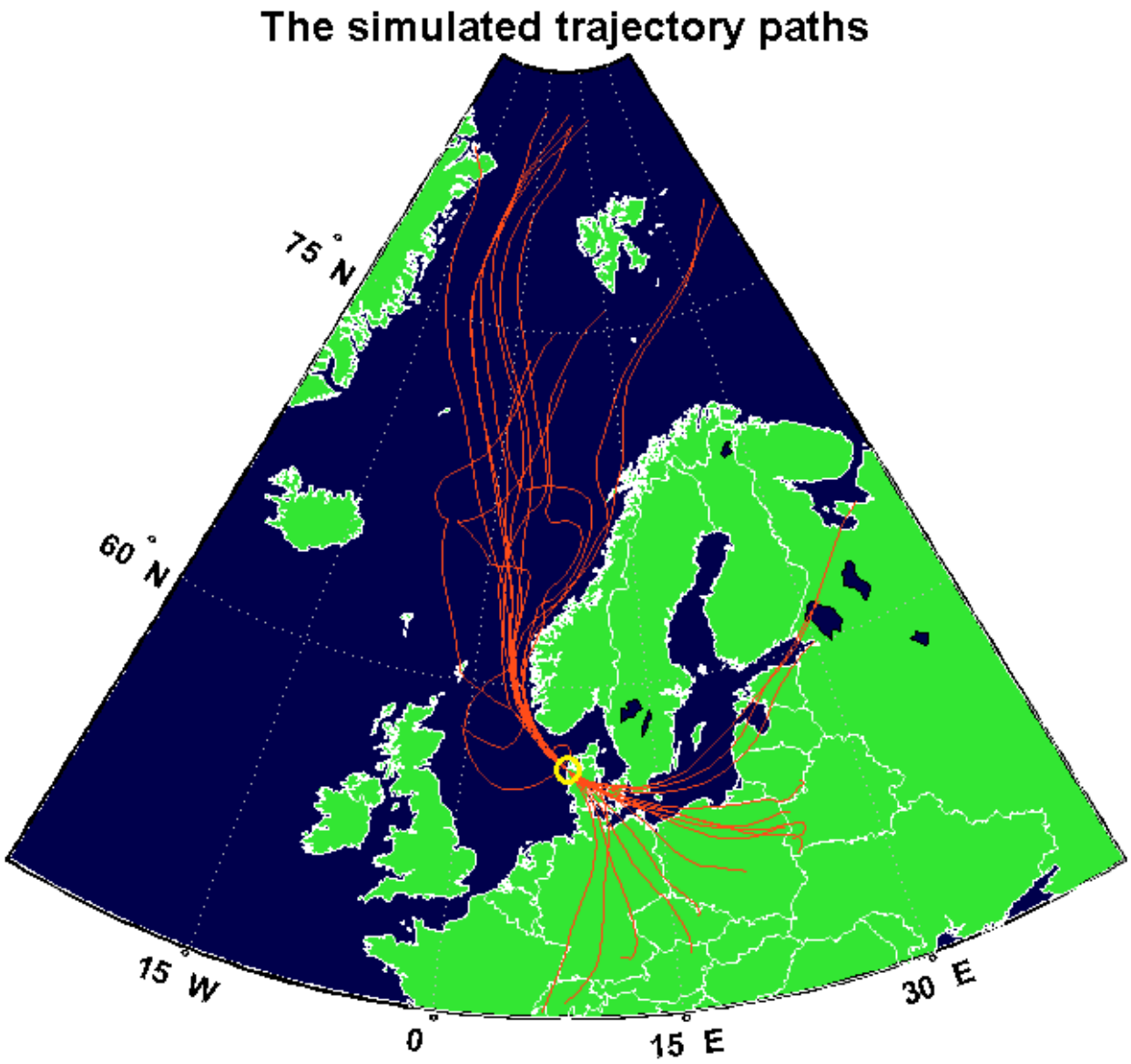

Figure A.1: The simulated trajectory paths. The yellow circle shows the approximate position of Høvsøre. Each trajectory is composed of a 96 hours backward trajectory and a 48 hours forward trajectory.

15 Appendix B

Table B.1: Speciation of VOCs used as input to the ADCHEM model.

Terrestrial BVOC emissions	α-pinene	β-pinene	D-limonene	Isoprene	**Marine BVOC emissions**	Isoprene
Anthropogenic VOC emissions	Ethanol	Ethane	1-Pentene	Nonane	1-Butene	
	Methanol	Formaldehyde	2-methylpropene	Xylene	1,2,4-trimethylbenzene	
	Butane	Acetaldehyde	Dodecane	Toluene	1,3,5-trimethylbenzene	
	Ethylene	MEK	Benzene	Undecane	1,2,3-trimethylbenzene	
	Propene	GLYOX	Ethylene	Propylene	Ethylbenzene	
		M-GLYOX	Decane	o-Xylene	m-Xylene	

16 Appendix C

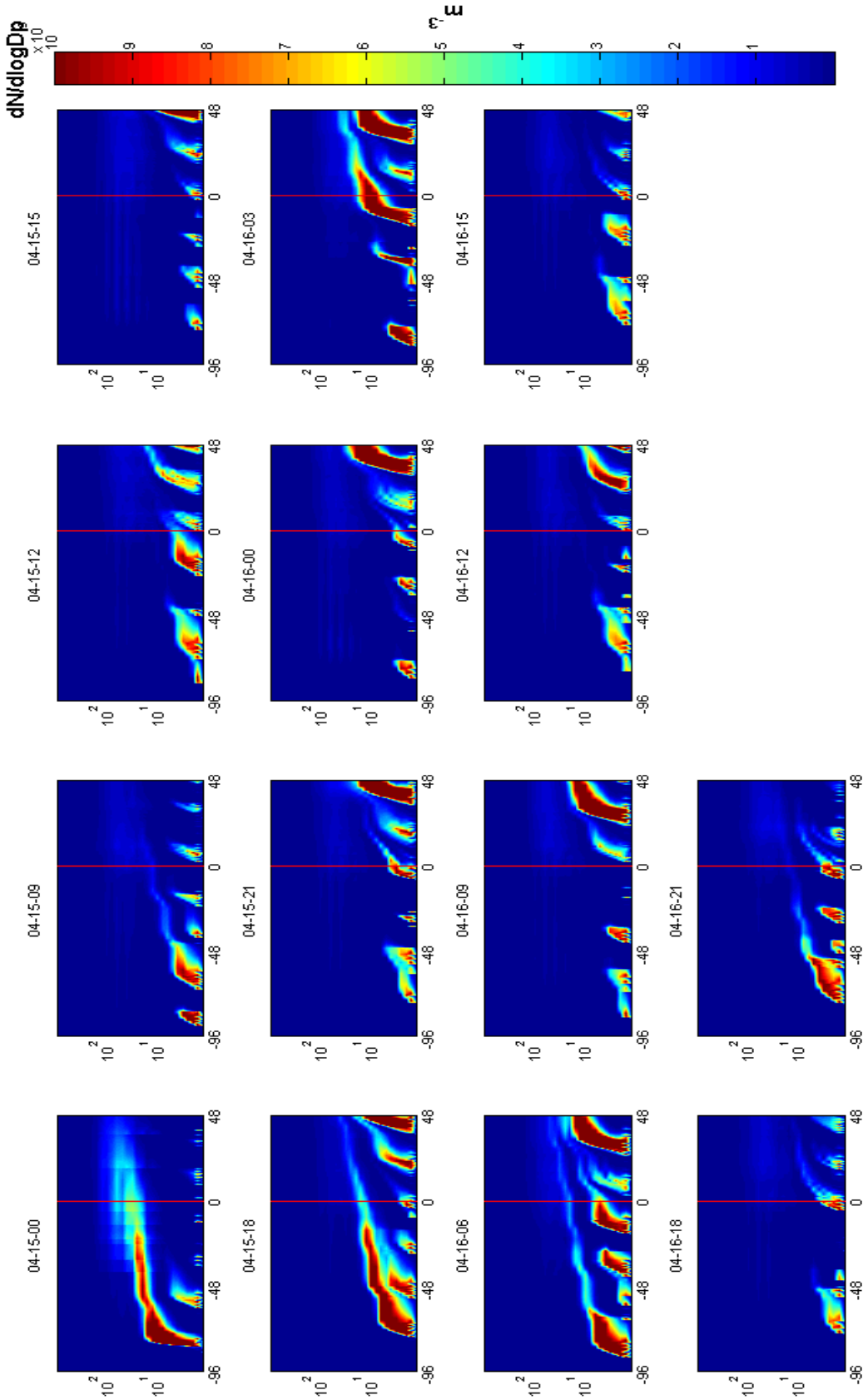

Figure C.1: *All model simulations for scenario 1. The simulations start 96 hours upwind of Høvsøre and end 48 hours after passing over Høvsøre. The red line indicates when the trajectory is over Høvsøre.*

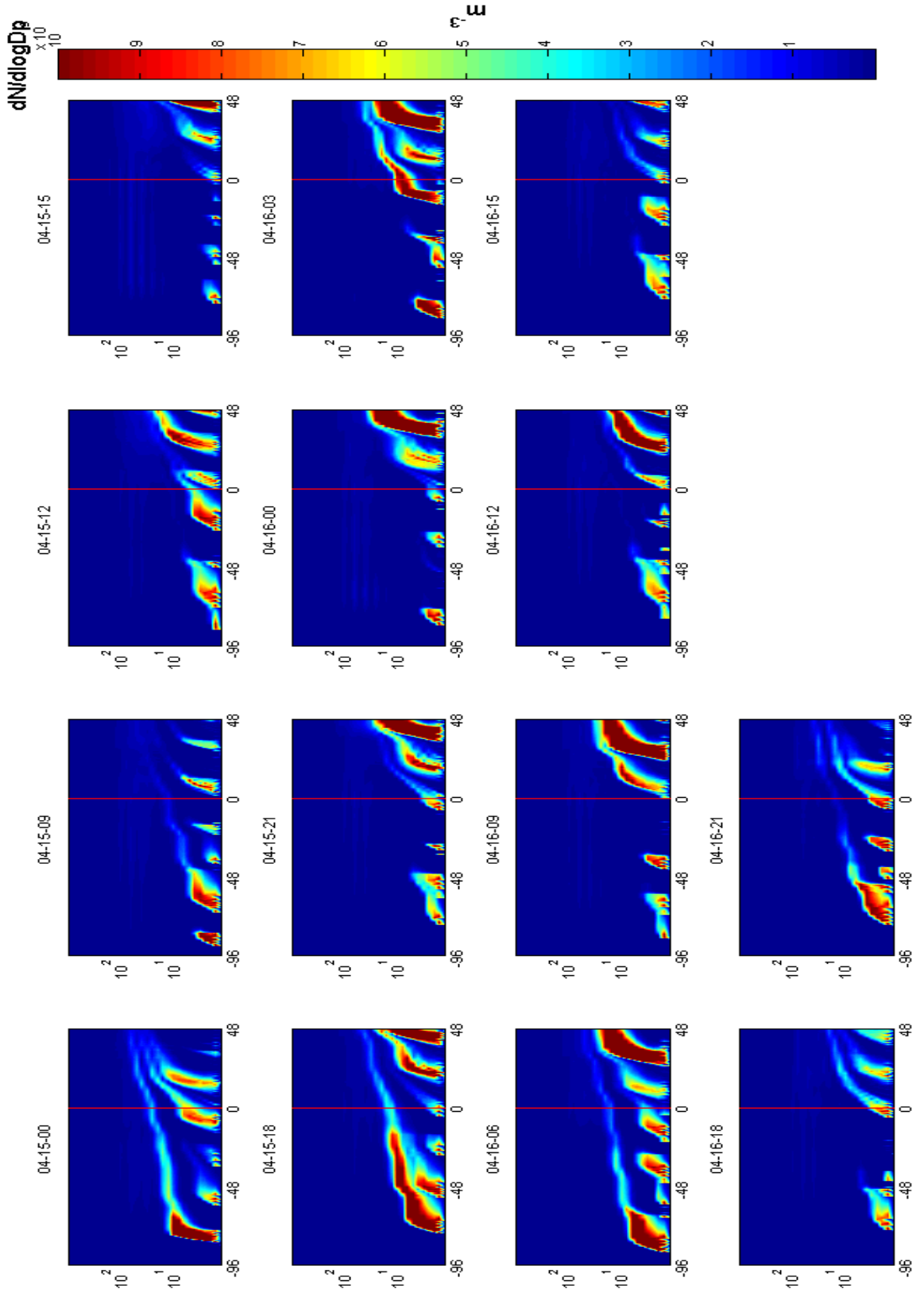

Figure C.2: *All model simulations for scenario 2. The simulations start 96 hours upwind of Høvsøre and end 48 hours after passing over Høvsøre. The red line indicates when the trajectory is over Høvsøre.*